8-2016

BIAS AND VARIABILITY IN IMAGE-BASED VOLUMETRIC YTTRIUM-90 DOSIMETRY

Wendy Siman

Recommended Citation

Siman, Wendy, "BIAS AND VARIABILITY IN IMAGE-BASED VOLUMETRIC YTTRIUM-90 DOSIMETRY" (2016). *UT GSBS Dissertations and Theses (Open Access)*. 703.
http://digitalcommons.library.tmc.edu/utgsbs_dissertations/703

BIAS AND VARIABILITY IN IMAGE-BASED VOLUMETRIC YTTRIUM-90 DOSIMETRY

by

Wendy Siman, M.S.

APPROVED:

____
S. Cheenu Kappadath, Ph.D.
Advisory Professor

____
Veera Baladandayuthapani, Ph.D.

____
Peter A. Balter, Ph.D.

____
Armeen Mahvash, M.D.

____
Osama R. Mawlawi, Ph.D.

APPROVED:

____
Dean, The University of Texas
Graduate School of Biomedical Sciences at Houston

BIAS AND VARIABILITY IN IMAGE-BASED VOLUMETRIC YTTRIUM-90 DOSIMETRY

A
DISSERTATION
Presented to the Faculty of

The University of Texas

Health Science Center at Houston

and

The University of Texas

MD Anderson Cancer Center

Graduate School of Biomedical Sciences

in Partial Fulfillment

of the Requirements

for the Degree of

DOCTOR OF PHILOSOPHY

By

Wendy Siman, M.S.

Houston, Texas

August 2016

Dedication

In loving memory of my mom and my sanctuary, Turino Lusfaidi, to whom I owe everything.

Acknowledgment

First and foremost, I would like to thank my advisor and my friend, Cheenu Kappadath, for his encouragement and for giving me the opportunity to pursue the doctoral study in medical physics at UTHealth/MDACC. As an advisor, at times he can be very demanding, but in retrospect I have benefited greatly from our hard work. Ever since I was a resident at MDACC, Cheenu has been helping me grow both professionally as a medical physicist and academically as a scientist.

I would also take this opportunity to thank my advisory-committee members: Veera Baladandayuthapani, Peter Balter, Armeen Mahvash, and Osama Mawlawi for taking time out of their very busy schedules to guide me through my dissertation work over the past 3 years. Special thanks to Osama Mawlawi, who has also been mentoring me since I was a resident. He always takes the time to provide me with very constructive criticism of our work.

Justin Mikell, my friend and lab mate, has been a very insightful person to bounce ideas off, especially regarding dosimetry. Amy Ninetto from the department of Scientific Publications at MDACC has been a tremendous help in editing and proofreading our manuscripts.

I would also like to acknowledge the following funding agencies for supporting my research NIH/NCI R01 CA138986, Siemens Medical Solutions (USA), and Sirtex Technology Pty Ltd (Australia).

All faculty members and administrative staff from the graduate school, the medical physics program, and especially from the Imaging Physics department have been very supportive of me during my time as a trainee.

BIAS AND VARIABILITY IN IMAGE-BASED VOLUMETRIC YTTRIUM-90 DOSIMETRY

Wendy Siman, M.S.

Advisory Professor: S. Cheenu Kappadath, Ph.D.

^{90}Y-microsphere therapy has been widely accepted as a treatment option for both primary and metastatic liver tumors where the patients are ineligible for surgical resection and external beam radiation therapy. The prognosis of untreated patient having liver cancer is very poor with life expectancy less than a year at advance stage. Hence the ability to predict treatment efficacy right after the treatment from post-therapy imaging will help personalize treatment strategies and achieve better outcome. Such prediction can be modeled from correlation of dose and tumor response metrics.

It has been shown that local dose deposition method can generate dose map from ^{90}Y emission images with accuracy comparable to dose-point kernel and Monte Carlo simulation methods. The bias and variability of the input images remain to be the weakest link in volumetric dosimetry. The objectives of this dissertation project were to improve image-based volumetric ^{90}Y dose quantification using current commercially available systems and to determine its limitation (bias/variability).

We have developed a practical image reconstruction method for ^{90}Y bremsstrahlung SPECT/CT (bSPECT/CT) images with CT attenuation correction and energy-window based background compensation. Although the volumetric quantitative accuracy of our bSPECT/CT images is limited by partial volume effect, the images can be used to accurately

quantify the total ^{90}Y activity delivered to the patient, which allow gross treatment delivery verification and limited outcome prediction.

We have also characterized the accuracy and variability of volumetric ^{90}Y dosimetry calculated from count-limited ^{90}Y-PET/CT images. Knowledge of overall errors (systematic and random) in volumetric ^{90}Y dosimetry is important to derive statistically significant dose-response model, which in turn allowing prediction of treatment outcome and personalization of treatment strategy.

Table of Contents

List of Figures

List of Tables

Chapter 1: Introduction

1.1. Background

Liver cancer is the second leading cause of cancer-related death; accountable for 745,000 deaths in 2012 (9.1% total). The prognosis for liver cancer is very poor with the mortality/incidence ratio of 0.95 (1). In the United States, the liver-cancer incidence and mortality of 39,230 and 27,170 are estimated in the year of 2016 (2). Similar to the world-wide prognosis, the prognosis of liver cancer in the US is also very poor with the 1- and 5-year survival rates of 44% and 17%. About 75% of the liver cancer cases are hepatocellular carcinoma (HCC) cases. Liver is also a common site for metastatis from tumors in organs that supply blood to portal vein, e.g., colorectal and pancreatic tumors.

Although surgical resection offers the best prognosis for liver-cancer patient, only < 25% of the patients are eligible for the procedure (3–6). These patients are usually not eligible for external beam radiation therapy because of radiosensitivity of both tumor and normal tissue. Radioembolization using radionuclide-doped microsphere is devised to exploit the difference in perfusion between normal liver and liver tumors (both HCC and metastatic) (7). In normal liver tissue, 70%–80% of the blood is supplied by the portal vein and the rest is supplied by the hepatic artery. In contrast, 80%–100% of the blood supply to liver tumor comes from the hepatic artery (8). This unique perfusion of the tumor allows selective delivery of radionuclide-doped microspheres, using intra-arterial technique, to the tumor while sparing the normal liver tissue. Note that the distribution of the microspheres is mechanistic instead of biochemical distribution; hence the treatment technique is called *selective* internal radiation therapy (SIRT) instead of targeted radionuclide therapy (TRT).

Currently there are two commercially available microspheres products: glass microspheres (TheraSphere™; BTG Biocompatibles Ltd, Farnham, UK) and resin microspheres (SIR-Spheres™; Sirtex Medical, Sydney, Australia). Resin microspheres are FDA approved to treat colorectal cancer liver metastates, while glass microspheres are under a humanitarian device exemption from the FDA to treat HCC. The differences in efficacy and toxicity of these two sphere types are subject to ongoing debate (9, 10), although recent studies show that the overall patient survival treated using either spheres is very comparable (11).

Both resin and glass microspheres are doped with Yttrium-90 (^{90}Y). ^{90}Y is selected to deliver the radiation therapy because of its attractive therapeutic properties. ^{90}Y is effectively a pure β- emitter with maximum and average β- energy of 2.28 and 0.934 MeV, with half-life of 64.2 hours. This energy spectrum corresponds to maximum and average penetration range of < 11 mm and < 4 mm in tissue, respectively. Hence, the ^{90}Y microspheres deposit their energy locally at their "target" location, which allows normal tissue sparing during the radiation treatment.

Treatment planning for ^{90}Y microspheres is done using surrogate ^{99m}Tc-MAA (macro aggregated albumin). Many studies have shown that distribution of MAA is not a consistent and reliable predictor of microsphere distribution (12, 13); therefore a direct imaging of post ^{90}Y-microsphere therapy is needed to confirm the delivery of ^{90}Y-microsphere distribution (qualitative imaging) and to predict the treatment outcome (quantitative imaging).

Although it is desirable from safety point of views (normal tissue sparing and patient release), as a pure β- emitter, ^{90}Y presents a very unique challenge for direct ^{90}Y imaging. ^{90}Y planar and SPECT images can be acquired by imaging the bremsstrahlung photons, produced as the β- particles interact with matter (liver parenchymal). ^{90}Y bremsstrahlung imaging is very challenging (Chapter 2) mainly due to the absence of photopeaks (γ and/or fluorescence x-ray) and sub-optimal hardware. Alternatively, ^{90}Y decay process also yield very low branch of 32 ppm positron emission, produced via internal pair production. The annihilation photons can be imaged using PET imaging, which poses very unique challenges as well due to very low signal (Chapter 3–5).

1.2. Purpose statement

The *long term goal* of this project is to assess the efficacy (tumor response and normal tissue toxicity) of ^{90}Y-microsphere therapy by correlating image-based volumetric dose quantification to tumor response and normal tissue complications, thus leading to treatment-strategy personalization and better patient outcome. The *objectives* of this dissertation project were to improve image-based volumetric 90Y dose quantification using current commercially available systems and to determine its limitation (bias/variability).

A period of 4–8 months is required to reveal whether or nor not the tumor is responding to ^{90}Y-microsphere treatment (14). In normal clinical workflow, the follow-up imaging procedure (e.g. CT, MR, ^{18}F PET/CT, ^{99m}Tc-MAA SPECT/CT) to evaluate treatment response is scheduled about 3 months after ^{90}Y-microsphere therapy, the earliest; while patients with advance liver cancer disease (both HCC and metastases), if left untreated, usually survive for less than 6–12 months (15–18). Hence the ability to predict the efficacy of treatment from post-therapy ^{90}Y imaging will allow personalization of treatment strategy, which will result in better outcome for the patient.

To realize this precision-medicine approach, several groups have used image-based volumetric dosimetry (19–23) to derive the dose-response model for ^{90}Y-microsphere therapy. ^{90}Y dose maps have been calculated from either ^{99m}Tc-MAA SPECT/CT, ^{90}Y bSPECT/CT, or ^{90}Y PET/CT images. At the current state of commercially available technology, there seems to be a general agreement that ^{90}Y PET/CT images are the better estimation of ^{90}Y activity (or dose) distribution. Studies have shown that ^{99m}Tc-MAA (macro aggregated albumin) is not a consistent and reliable surrogate of ^{90}Y-microsphere distribution (12, 13); while ^{90}Y bSPECT/CT images have been shown to be inferior in image resolution, image contrast, and hence volumetric quantitative accuracy compared to ^{90}Y PET/CT (24–26).

Nevertheless, in the United States, majority of post-treatment ^{90}Y imaging procedures, which are important to verify the treatment delivery, are done on SPECT/CT scanners. Most recent development in bremsstrahlung SPECT/CT (bSPECT/CT) image reconstruction has shown that with incorporation of physics modeling using Monte Carlo simulation, it is possible to generate accurate quantitative bSPECT/CT images (27, 28). However, these advance techniques are not widely available for clinics where ^{90}Y-microsphere therapies are done. In the specific aim 1 of this dissertation project, we have developed a practical method, using commercially available SPECT/CT systems, to reconstruct bSPECT/CT images with improved image quality and improved activity quantification.

Recent ^{90}Y-PET-based dose-response studies have not been able to show a consistent and statistically significant relationship between dose metrics (D_{70} and/or D_{mean}) and tumor response to ^{90}Y-microsphere therapy (22, 23). Volumetric dosimetry that incorporates radiobiological modeling is suggested to have improved dose-response model (29–31). In addition, dose-response model also needs stratification based on microsphere type, tumor type, dosimetry and response quantification methods (30, 32). Incorporation of radiobiological modeling requires information of 3D dose distribution, which can be estimated from ^{90}Y PET/CT images (33–35). The performance of volumetric ^{90}Y dosimetry calculated from degraded ^{90}Y PET/CT images, however, has not been characterized. In specific aim 2–4, we characterized and optimized the performance of PET-based volumetric dosimetry.

1.3. Hypothesis and aims

1.3.1. Central hypothesis

The central hypothesis of this dissertation is that optimization of ^{90}Y emission image reconstruction, using current commercially available imaging systems, can maintain the overall errors (systematic and random) in volumetric dose quantification to < 20% in clinically relevant imaging conditions.

1.3.2. Specific aim 1

SA 1: *Develop practical ^{90}Y bremsstrahlung SPECT/CT imaging protocol.*

Several groups (27, 28) have shown that Monte-Carlo simulation can accurately model the object attenuation, scatters, and collimator-detector response to reconstruct quantitative bresmsstrahlung SPECT/CT (bSPECT/CT) images with quantification error of mean activity concentration < 10%. These advance image reconstruction method, however, are not commercially available and cannot be readily implemented in clinical practice, especially in clinics that are not associated with academic hospital, a common practice in the United States.

The *objective* of this aim is to improve image quality and ^{90}Y dosimetry quantification of bSPECT/CT images using a commercially available imaging system. We tested the *working hypothesis* that energy-window based "background" compensation can be used to improve volumetric dose quantification and image quality in ^{90}Y bSPECT/CT.

In this aim, we developed a practical and simple methodology to determine bremsstrahlung imaging energy window (EW) and to correct for attenuation (CT-based) and "background" signal (EW-based). This methodology can readily be applied in clinical practice to improve image quality and quantification of ^{90}Y bSPECT/CT images.

Research design:

- *SA 1.1*: Determine the imaging EW for ^{90}Y bremsstrahlung imaging
- *SA 1.2:* Develop the EW-based background compensation model
- *SA 1.3*: Optimize the image reconstruction parameters
- *SA 1.4:* Establish the count-to-activity calibration factor

1.3.3. Specific aim 2

SA 2: *Optimize ^{90}Y PET/CT image reconstruction for volumetric dose quantification.*

Volumetric dosimetry has been calculated from ^{90}Y PET images (20, 22, 25). Recent studies on image reconstruction-parameters optimization for quantitative ^{90}Y PET imaging (24, 36–39), however, have still been based on mean-activity-concentration recovery coefficient as the objective function, which is more relevant to diagnostic dosimetry and detection tasks.

The *objective* of this specific aim was to improve quantification of volumetric ^{90}Y dosimetry by optimizing the image-reconstruction protocol. Our w*orking hypothesis* for this aim was that using dose volume histogram estimate (DVH'), instead of mean dose recovery coefficient, as the optimization objective function would result in smaller errors in 3D dose distribution.

Traditional objective function of mean dose recovery coefficient can only be used to optimize the number of equivalent iterations and it does not take into account the change of 3D dose distribution due to image noise. In this aim, using errors of DVH' as the objective function, we were able to concurrently optimized the number of equivalent iterations and the filtration full width at half maximum and, consequently, minimized the errors in volumetric quantification of ^{90}Y dose distribution.

Research design:

- *SA 2.1*: Optimize the number of equivalent iterations (subset × iteration) based on convergence of mean dose recovery coefficient (RC).
- *SA 2.2*: Optimize the reconstruction parameters (equivalent iterations and filter FWHM) based on the errors in DVH'.

1.3.4. Specific aim 3

SA 3: *Determine the errors and variability of volumetric dose quantification from ^{90}Y PET/CT images*

Volumetric ^{90}Y dose has been quantified (22, 23, 25) using cumulative dose volume histogram calculated from ^{90}Y PET images (DVH') and has been used to empirically derive dose-response relationship to predict treatment outcome. ^{90}Y PET images, however, are subject to image degrading factors such as partial volume effect, image noise, and motion blur (40). Consequently, the DVHs'suffer from errors due to these degrading factors. While these factors degrade all emission imaging, ^{90}Y PET imaging presents a unique challenge in the extremely low signal (positron yield of 32 ppm).

Despite increased use of ^{90}Y PET images for volumetric ^{90}Y dosimetry, the impact of very low signal on the errors, both systematic and random, in the resulting DVH' and it summary metric (e.g., D_{mean} and D_{70}) has not been thoroughly evaluated.

The *objective* of this aim was to characterize the systematic and random errors in quantification of ^{90}Y volumetric dose distribution from ^{90}Y PET images. The *working hypothesis* of this aim was that partial volume effect governs the errors in volumetric dose quantification; while the count limitation determines the random errors.

In this aim, we characterized the overall errors (systematic and random) of volumetric quantification of ^{90}Y dose distribution from ^{90}Y PET/CT images, which are important in designing clinical studies to derive the dose-response correlation derived using dose metrics from ^{90}Y PET images. Knowledge of the limitation in the dose metrics also allow understanding of the confidence level of the response prediction.

Research design:

- *SA 3.1*: Characterize the effects of the activity-dependent bias

- *SA 3.2:* Determine the impact of image noise (duration) and partial volume effect (PVE) on image-based volumetric dose quantification

1.3.5. Specific aim 4

SA 4 : *Determine the effectiveness of quiescent period gating (QPG) method for reducing errors in volumetric dose quantification from ^{90}Y PET/CT images.*

^{90}Y-PET acquisition duration can be up to 30 min/bed, during which, the PET data acquired are degraded by motion blur due to time-averaging of multiple breathing cycles (typically 4 s/cycle). Although motion correction has been subject to active research in ^{18}F-PET/CT imaging (41–44), effect of motion blur on volumetric ^{90}Y dose distribution and motion compensation strategies in ^{90}Y PET/CT imaging have not been evaluated.

Most widely used motion correction technique is gating-based PET/CT acquisition at quiescent respiratory period (45). Quiescent period gating (QPG) method–both phased and amplitude-based methods–group the acquired data into smaller bins to minimize the spatiotemporal mismatch in the data due to the respiratory cycles (46). Each bin will have reduced systematic errors due motion blur, but each data will have lower counts. As a result, gating-based technique trades off systematic errors due to motion blur with both systematic and random errors due to lower signal used to reconstruct the gated PET images. In contrast to ^{18}FDG PET/CT imaging, where the acquisition duration is usually 3 min/bed, in ^{90}Y-PET/CT imaging with duration of 30 min/bed, it is practically not possible to increase the duration to compensate for the count loss.

The ***objective*** of this aim was to determine if motion compensation using QPG is effective at reducing the overall errors in quantification of volumetric ^{90}Y dose distribution using dose volume histogram calculated from ^{90}Y PET images. Our ***working hypothesis*** was that tumor with relative motion range < 1 does not benefit from QPG motion compensation because the overall errors in the DVH' calculated from the compensated ^{90}Y images are not reduced by the motion compensation.

In this aim, we characterized the impact of both low count, and motion blur, and the effectiveness of their trade-off using QPG on quantification of volumetric ^{90}Y dose distribution (DVH'). We found that QPG motion compensation did not always reduce the overall errors in DVH'; therefore this work is important because it allows identification of ^{90}Y PET/CT imaging condition where the volumetric tumor dosimetry can benefit from QPG motion compensation.

Research design

- SA 4.1: Evaluate the impact of increase image noise (due to gating) on AC quantification
- *SA 4.2*: Evaluate the impact of motion on activity distribution quantification
- *SA 4.3*: Determine the effectiveness of QPG method in improving AC quantification in ^{90}Y PET/CT images suffering from motion blur

1.4. Significance and Innovation

1.4.1. Significance

In the specific aim 1 of this dissertation project, we have developed a practical method, using commercially available SPECT/CT systems, to reconstruct bSPECT/CT images with improved image quality and improved activity quantification. Although the quantitative accuracy of our bSPECT/CT images is very limited by partial volume effect (due to sub-optimal collimator design), the background compensated and attenuation corrected bSPECT images can be used to accurately quantify the total ^{90}Y activity delivered to the patient, which allow gross treatment delivery verification and limited outcome prediction.

Recent ^{90}Y-PET-based dose-response studies (22, 23) have not been able to show a consistent and statistically significant relationship between dose metrics (D_{70} and/or D_{mean}) and tumor response, partly because the accuracy and variability in the dose metrics are largely unknown. In specific aim 2–4, we characterized the accuracy and variability of volumetric ^{90}Y dosimetry calculated from count-limited ^{90}Y-PET/CT images. Knowledge of overall errors (systematic and random) in volumetric ^{90}Y dosimetry is significant because it is the first step in a continuum of research that is expected to derive statistically significant dose-response model, which in turn allowing prediction of treatment outcome and personalization of treatment strategy.

In addition, it has been suggested that the dose-response model can be improved by incorporating radiobiological models, which require information of 3D dose distribution. 3D ^{90}Y dose maps calculated from ^{90}Y-PET/CT images are subject to image degrading factors that affect the ^{90}Y-PET/CT images. In addition to characterizing the overall errors, in specific aim 2–4, we also improved the estimated ^{90}Y dose map by optimizing the image reconstruction protocol and compensating motion blur.

1.4.2. Innovation

The innovation of bSPECT/CT imaging in specific aim 1 is that we developed an empirical background compensation based on adaptation of energy-window based scatter estimation. The proposed reconstruction method is very practical that it does not need any advance techniques such as Monte-Carlo simulation based reconstruction, which is not widely available for clinical use.

Methods to generate dose map from ^{90}Y PET/CT images have been developed (33–35). The volumetric ^{90}Ydose distribution inside the tumor margin, which is calculated from the dose map estimate, has been used to derive dose-response model and to predict treatment outcome (21–23, 47). The quantitative reconstructions of these ^{90}Y PET/CT images, however, are optimized for quantifying mean dose (24, 36–39), instead of quantifying the ^{90}Y dose distribution used to generate the ^{90}Y dose map estimate. The innovation in specific aim 2–4 on ^{90}Y-PET/CT imaging is that we characterized the quantification errors (systematic and random) of volumetric ^{90}Y dose distribution calculated from ^{90}Y PET images. The volumetric ^{90}Y dose distribution was quantified using dose volume histogram estimate (DVH'). In specific aim 2, we optimized ^{90}Y PET/CT image reconstruction by minimizing the errors in DVH', which was innovative because, to the best of our knowledge, there have not been any published works on optimizing ^{90}Y PET/CT image reconstruction other than using recovery coefficient of mean activity concentration as the objective function. In specific aim 3 and 4, we quantified the errors (systematic and random) in DVH' due to count limitation and motion blur, respectively.

1.5. Chapters organization

The main body of this dissertation consists of 3 chapters, each written in manuscript form for peer-review journal publication. Chapter 2 addresses specific aim 1. Chapter 3 addresses specific aim 2 and 3. Chapter 4 addresses specific aim 4. The final chapter 5 consists of summary about the key findings in this dissertation work, study limitation and future work.

Chapter 2: Practical reconstruction protocol for quantitative ^{90}Y bremsstrahlung SPECT/CT

2.1. Introduction

Yttrium-90 microsphere therapies are used in the management of unresectable primary and metastatic liver cancers.(48, 49) In treatment planning, the radiopharmaceutical macro-aggregated albumin (^{99m}Tc-MAA) is used as a surrogate for ^{90}Y microspheres. First, planar imaging is used to determine the lung shunt fraction, which is incorporated into the dosimetry calculation to prevent radiation pneumonitis from ^{90}Y therapy. Next, single-photon emission computed tomography (SPECT)/computed tomography (CT) imaging is used to determine whether there is extrahepatic uptake of the ^{99m}Tc-MAA and adequate perfusion of the target lesions. However, several studies have shown that the distribution of ^{99m}Tc-MAA prior to treatment may not be a consistent and reliable indicator of the post-treatment distribution of the ^{90}Y-microspheres.(12, 13) These potential discrepancies in distribution between planning ^{99m}Tc-MAA and treatment ^{90}Y-microspheres support the need for post-treatment ^{90}Y imaging to assess treatment delivery. However, bremsstrahlung ^{90}Y imaging is challenging.

In contrast with the majority of the radionuclides used in nuclear medicine imaging, ^{90}Y is effectively a pure beta emitter, i.e., it lacks discrete-energy photon emissions, such as gamma rays and/or characteristic fluorescence X-rays. The X-ray photons emitted by ^{90}Y are very low in both yield (<< 1 ppm) and energy (<< 18 keV), and the gamma photons emitted by ^{90}Y have an insignificant yield (<< 1 ppm) and very high energy ($\sim 2\ MeV$). Yttrium-90 activity distribution *in vivo* is traditionally assessed by imaging the bremsstrahlung photon, which is produced from interactions of energetic beta particles with soft tissue, using planar and/or SPECT/CT imaging.

Yttrium-90’s lack of photopeaks has stunted standardization of ^{90}Y bremsstrahlung imaging procedures; consequently, image quality varies widely amongst different facilities. The ^{90}Y decay process also has a very small branching to the excited state of stable ^{90}Zr, which is followed by an internal pair production (32 ppm per β^- decay).(50) The positrons generate a pair of 511-keV annihilation photons that can be imaged using ^{90}Y positron emission tomography (PET)/CT. Recent studies have suggested that ^{90}Y PET/CT imaging provides better image quality (contrast and resolution) and quantification than bremsstrahlung SPECT/CT.(24, 25) Preliminary results of studies of tumor dosimetry, treatment response, and toxicity based on quantitative ^{90}Y PET/CT and ^{90}Y SPECT/CT post-therapy imaging have been presented. (14, 22, 51) However, at present, there is no well-established standardized imaging protocol for ^{90}Y imaging *in vivo* with either SPECT/CT or PET/CT.

In contrast to gamma and X-ray emitter imaging, in which the object spatial information is carried by photons with a discrete energy, bremsstrahlung imaging’s the object spatial information is carried by photons with a continuous energy distribution. In discrete energy photopeak imaging, the imaging energy window (EW) is defined such that it accepts most of the primary photon emission while rejecting most of the scatter. The EW is usually centered on the photopeak and its extend (width) is governed by the energy resolution of the gamma camera, however the continuous nature of ^{90}Y photon emissions prohibit such straightforward approach. Simulation work (52, 53) have shown that a typical ^{90}Y bremsstrahlung emission spectrum from ^{90}Y activity in the liver can be expressed as the sum of 5 spectral components: primary bremsstrahlung, object scatter, camera backscatter, collimator scatter and penetration, and lead X-rays produced in the collimator. At any given EW, the ratio of primary bremsstrahlung to the total number of photons detected is $< 15\%$, with the highest primary fraction around 80–180 keV.(52–54)

Research on improving ^{90}Y bremsstrahlung imaging both qualitatively and quantitatively is ongoing, but most of the published solutions require some sort of Monte Carlo simulation. Rong et al used Monte Carlo simulations to accurately model the energy dependent object attenuation, scatter and the collimator-detector response to obtain quantitatively accurate images(27). The net percent errors in activity estimates from physical geometrical phantom experiments and simulated patient data were shown to be 5-10 %. Elschot et al directly incorporated into the reconstruction algorithm the energy dependent photon scatter and attenuation estimated from Monte Carlo simulations(28). Their approach demonstrated higher tumor contrast and lower mean residual count in lung insert albeit at the cost of higher image noise. These advanced Monte Carlo based approached are not commercially available and cannot be easily implemented in the routine clinical practice. The lack of their widespread use is further exacerbated by the fact that many ^{90}Y procedures, at least in the United States, are performed in interventional radiology clinics that are often not associated with academic hospitals.

The objective of this study was to develop a practical imaging protocol to improve ^{90}Y bremsstrahlung SPECT/CT image quality and quantification that could be readily implemented on commercially available imaging systems. To accomplish our objective, we developed a simple method for determining an appropriate imaging EW, its EW-based background compensation (BC), and CT-based attenuation correction (AC). Furthermore, we present approaches for the optimization of SPECT reconstruction parameters for both detection and quantification. Finally, we address the implementation and accuracy of self-calibration that lead to total activity quantification from ^{90}Y SPECT/CT images.

2.2. Methods

All data acquisition and analysis were performed on Symbia TruePoint SPECT/CT systems (Siemens Medical Solutions, Hoffman Estates, IL, USA).

2.2.1. Defining energy windows for CT attenuation correction

Six preliminary EWs (the maximum allowed on the SymbiaTruePoint SPECT/CT systems) were defined in order to separate the total ^{90}Y bremsstrahlung spectrum into regions dominated by different spectral components: 70–100 keV (object scatter and lead X-rays), 100–125 keV (object scatter), 125–175 keV (backscatter), 175–225 keV (backscatter), 225–300 keV (backscatter, collimator scatter and septal penetration), and 300–400 keV (collimator scatter and septal penetration). The maximum widths of the EWs were constrained by the ability to accurately represent photon attenuation at the mean energy of each window to facilitate SPECT AC, such that, if $\Delta\mu$ is the difference in linear attenuation, μ, between the extreme energies of a window, we required $\Delta\mu/\mu_{\text{mean}} < 10\%$. The 10% limit on $\Delta\mu$ was based on earlier work that showed that SPECT images were accurate to within 1% when $\Delta\mu/\mu_{\text{mean}} < 6\%$.(55)

The electron density phantom we used (model 062, CIRS, Norfolk, VA) enables precise correlation of CT data in Hounsfield units (HU) to the linear attenuation coefficient, μ (cm^{-1}). It includes 8 different reference tissues with CT values ranging from −790 HU (lung inhale) to 235 HU (trabecular bone). An axial CT scan of the electron density phantom was performed at a high tube current to minimize CT noise (130 kVp, 200 mAs). The CT image was converted into μ-maps using proprietary software (e.Soft, Siemens Medical Solutions) that converted each CT image into a μ-map at a user-defined emission energy at 5 keV intervals from 70–511 keV (the range is limited by the software). Circular regions of interest (ROIs) were drawn within the inserts to calculate their μ as a function of photon energy.

Starting with the above-defined 6 EWs, we iterated on the EW widths so that the $\Delta\mu/\mu_{\mathrm{mean}}$ was < 10% in each EW for the adipose, soft tissue, muscle, and liver inserts. Considerations were also made to isolate the various scatter components in different EWs.

2.2.2. Choosing appropriate imaging energy windows

In this work, the primary signal was assumed to be spatially registered within the object, while the background signal was considered to be more widely distributed across the image. It is important to note that this primary signal definition may contain object scatter in addition to the primary bremsstrahlung and perhaps even some smaller contributions from collimator scatter, septal penetration, and backscatter. We defined the imaging EW as the EW that had the highest fraction of primary signal to background signal.

Fig 1 shows the phantom experiment setup, which acquired using a gamma camera with 1.6-cm (5/8-inch) crystal. Yttrium-90 (III) chloride solution was placed in a vial (8.5 cm × 3.3 cm) 1 cm. The ^{90}Y phantom was positioned at 30 cm above the gamma camera with a medium-energy low-penetration (MELP) collimator. Acrylic slabs of various thicknesses (2, 5, 9, 12, and 16 cm) were placed right below the phantom to introduce attenuation and scatter. For the 5 cm-thick acrylic slab, the distance between the collimator and the phantom was varied to 15, 20, 25, 30, and 35 cm. Planar static images were acquired for each imaging condition. Each static image was acquired in the 6 EWs determined in Sec. 2.A. For each imaging condition, planar images with 2 million counts were acquired in the 90–125 keV EW.

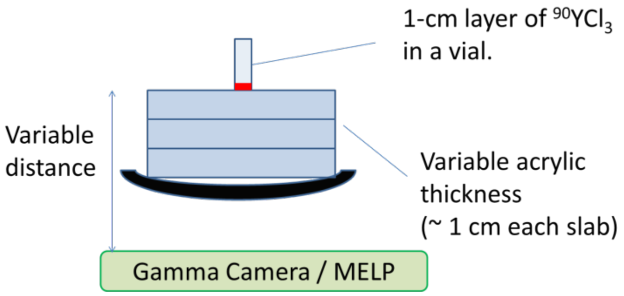

Fig 1. The experimental setup used to acquire ^{90}Y planar images under different imaging conditions. Both the acrylic thickness and the distance between the collimator and the phantom were varied.

To calculate the signal-to-background ratio, we drew 2 ROIs on each of the static images (Fig 2): a small ROI at the center, enclosing the image of the object, and a larger ROI that enclosed the entire field of view (FOV). The total counts in the small ROI represented the numbers of photons carrying more object spatial information. This was designated as the primary signal. The total counts in the periphery, calculated by subtracting the total counts in the smaller ROI from those in the larger ROI, represented the number of scattered photons that had already lost their spatial information. This was designated as the background signal.

For each EW, the mean pixel count per keV was calculated by dividing the total counts from the ROIs by the EW width and the number of pixels in the ROI. Signal-to-background ratio was calculated as the mean pixel count/keV in the center divided by the mean pixel counts/keV in the periphery. The signal-to-background ratios were calculated for all static phantom images (all 6 EWs for all imaging conditions). The EW with the highest signal-to-background ratio was used as the imaging EW.

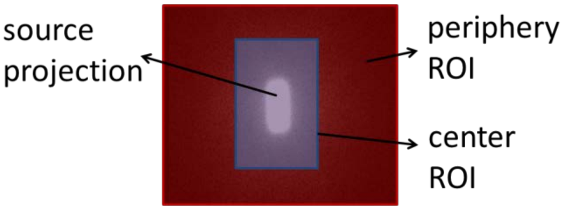

Fig 2. The larger ROI (periphery), indicated in red, encloses the entire FOV of the gamma camera. The smaller ROI (center), indicated in blue, encloses the projected image of the phantom. The background counts in the periphery region were calculated by subtracting the counts for the small ROI from those of the large ROI. The small ROI contains both the primary signal counts, which carry more object spatial information, and unwanted background counts.

2.2.3. Developing empirical energy window-based background compensation for ^{90}Y bremsstrahlung imaging

Our empirical EW-based BC model adapted the EW-based scatter correction model, in which the scatter in the imaging EW is estimated as a scaled image of the scatter-estimate EW.(56–58) In this work, we used scaled images of the BC EW as a model to compensate for the background signal in the imaging EW. The BC EW was selected empirically from our phantom study and based on the errors in the activity recovery coefficient and the amount of residual background count in the cold lung insert. The scaling coefficients were calculated from clinical images. The use of a single scaling coefficient for BC can be justified if low variation in the scaling coefficients is observed under clinical imaging conditions. We used clinical planar images (anterior and posterior views) of 10 post-^{90}Y-microsphere therapy patients with inherent random geometries (patient thicknesses and distance to collimator). The images were acquired using a Symbia T gamma camera with a crystal thickness of 1.6 cm. For each potential BC EW (5 EWs: A, C, D, E, and F), the scaling coefficients were derived by averaging the scaling coefficients calculated for each clinical planar image of the 10 patient scans, for 20 images in total. The scaling coefficients were calculated as the ratio of the periphery ROI total counts in the imaging to the potential BC EWs (Fig 3). The variations in the scaling coefficients for each potential BC EW in the clinical scans were reported as 1 standard deviation.

Fig 3. Clinical planar images in imaging (A) and potential background compensation (B) energy windows showing the positioning of regions of interest (outside but adjacent to the liver) from which the total counts were extracted to calculate the scaling coefficient for the empirical background compensation model. The area superior to the liver was excluded to avoid including any signal contamination from the lung shunt.

The most appropriate BC EW was determined empirically according to 2 criteria: 1) the maximum recovery coefficient of the 37-mm sphere and 2) the minimum residual activity concentration in the cold lung insert of a NEMA IEC body phantom (Biodex, Shirley, NY). The phantom was filled with 2.8 GBq (75.4 mCi) $^{90}YCl_3$ with the sphere-to-background ratio of 7.8**.** SPECT/CT images of the phantom were acquired for 28 s/view for 2 × 64 views over 360° using Symbia T6 SPECT/CT systems with 1.6 cm NaI(Tl) detectors and MELP collimators. The acquisition EWs were chosen based on the results reported in Sec. 3.B.

SPECT/CT images of the IEC phantom were reconstructed using the Ordered Subset Expectation Maximization (OSEM) (Flash 3D, Siemens Medical Solutions) algorithm with CT attenuation (See Sec. 2.A) and 5 different BC models. The number of equivalent iterations (subset × iteration) was 8 × 8 (based on results reported in Sec. 3.E). The reconstructed images had a matrix size of 128 × 128 and a voxel size of 4.8 mm. No post-reconstruction filter was applied to the images to avoid further image resolution degradation on inherently poor-resolution bremsstrahlung ^{90}Y images.

For each reconstructed image set, a spherical volume of interest (VOI) with a diameter of 10 mm was placed inside the 37-mm sphere, and cylindrical VOIs with diameters and lengths of 25 mm were placed in the adjacent background and in the lung insert. A VOI of 10 mm in diameter for the 37-mm sphere was chosen to decrease the partial volume effect. Observed sphere-to-background ratio recovery was calculated from the mean counts inside these VOIs, i.e., $mean_{sphere}/mean_{background}$. Residual activity concentration in the lung insert was calculated as a fraction of mean count in the background, i.e., $mean_{insert}$ /$mean_{background}$. The most suitable BC model was determined based on the recovery of the true sphere-to-background ratio (measured/true) and the residual mean count in the lung insert.

The improvement in image contrast after BC was evaluated visually and semi-quantitatively by comparing the contrast-to-noise ratio (CNR) of the lesions before and after the BC was applied. The CNRs of the lesions were calculated as $\mathrm{CNR} = \frac{\mathrm{mean}_{\mathrm{lesion}} - \mathrm{mean}_{\mathrm{background}}}{\sqrt{\mathrm{mean}_{\mathrm{background}}}}$; where $\mathrm{mean}_{\mathrm{lesion}}$ and $\mathrm{mean}_{\mathrm{background}}$ are mean ROI counts in the hot lesions and warm liver, respectively.

2.2.4. SPECT/CT activity calibration for quantification

The SPECT calibration factor was defined as the ratio of the total activity in the FOV to the total counts in the FOV. For ideal image reconstruction (with accurate corrections for scatter, attenuation, and collimator-detector response), calibration with a point source in air suffices. In practice, however, the image reconstruction is not ideal, so the calibration factor is usually derived from phantom images with all the necessary corrections applied. It is imperative that the calibration of the SPECT/CT imaging system remain valid under clinically relevant conditions to minimize the variations in activity quantification that may result from a mismatch between the calibration and clinical imaging conditions.

Post-therapy ^{90}Y SPECT/CT scanning presents a unique condition in which the total ^{90}Y activity inside the liver (and hence inside the SPECT FOV) can be determined with uncertainty $< 10\%$. Clinical images acquired under such conditions can be used to calibrate the SPECT/CT imaging system. In this study, the calibration factors were calculated from 30 post-^{90}Y-microsphere therapy SPECT/CT studies with a wide range of abdomen sizes, from 19–40 cm (measured in the anterior-posterior direction from the transaxial CT images). The patient scans were chosen such that the net administered activity could be determined with high accuracy. Activity uncertainty in the FOV was maintained at $< 7\%$ by selecting patient scans with a lung shunt fraction $< 5\%$ and administered activity residuals $\leq 2\%$ and by assuming the error in dose calibrator assay $\leq 3\%$.

All clinical images were acquired using gamma cameras with a crystal thickness of 1.6 cm in the EWs described in Secs. 2.A and 2.B. The planar images were acquired for 10 min with a matrix size of 256 × 256 and pixel size of 2.4 mm. The SPECT projection images were acquired for 28 s/view for 2 × 64 views over 360°. The SPECT images were reconstructed using the OSEM algorithm with number of equivalent iterations of 64, (optimized in Sec. 2.E), matrix size of 128 × 128, voxel size of 4.8 mm, and post-reconstruction Gaussian filter of 4.8 mm.

The calibration factors were calculated for the following image types: planar images, SPECT images with no correction (SPECT only), SPECT images with CT-based AC (Sec. 2.A) (SPECT with AC), and SPECT images with both CT-AC (Sec. 2.A) and BC (Sec. 2.C) (SPECT with AC+BC). For each image type, we used linear regression analysis to derive the relationship between the total injected activity in the FOV and the corresponding total count rates (total counts/frame duration) in the same image FOV. The global calibration factor and its uncertainty were calculated from the regression equation as the gradient and its standard error. The validity of using a single global calibration factor under various clinical imaging conditions was evaluated based on the standard deviation of the residuals (the difference between the actual activities with the predicted injected activities with respect to the actual values) in the linear regression analysis.

2.2.5. Reconstruction-parameter optimization for qualitative and quantitative SPECT/CT images

The IEC phantom data acquired in Sec. 2.C were also used for this section. The SPECT/CT images were reconstructed using the 3D-OSEM (Flash 3D) algorithm with CT attenuation (Sec. 2.A) and a final empirical BC model (Sec. 3.C). We varied the number of equivalent iterations(59) from 8 to 256: 8 subsets with 1–16 iterations and 16 subsets with 12–16 iterations. The reconstructed images had a matrix size of 128 × 128 and a voxel size of 4.8 mm. No post-reconstruction filter was applied to the images. For each total number of iterations, the SPECT/CT count-to-activity calibration factor was calculated as the total injected ^{90}Y activity divided by the total counts in the entire reconstructed volume. Self-calibration of the respective SPECT/CT images was performed for absolute image quantification, i.e., voxel unit in Bq/mL.

Spatial resolution (partial volume effect) and convergence of iterative reconstruction both affect the SPECT quantitative accuracy. For each reconstructed image, a spherical VOI with a diameter of 10 mm was placed inside the 37-mm sphere, and cylindrical VOIs with a diameter and length of 25 mm were placed in the adjacent background and in the lung insert. VOI of 10 mm in diameter for 37-mm sphere was used to minimize the partial volume effect. Measured sphere-to-background ratios were calculated from the mean counts inside these VOIs ($\text{mean}_{\text{sphere}}/\text{mean}_{\text{background}}$). The total number of iterations was optimized based on the recovery of the true SBR, i.e., $\text{SBR}_{\text{measured}}/\text{SBR}_{\text{true}}$. The activity quantification accuracy was measured as the activity recoveries in the 37-mm sphere and in the background, i.e., $\text{measured activity}/\text{true activity}$. The efficacy of the EW BC was also evaluated by measuring the relative activity in the lung insert with respect to the background activity. In addition, the activity quantifications in the 37-mm sphere and in the background using SPECT with CT AC+BC were also compared with the activity quantification in SPECT with AC.

2.3. Results

2.3.1. Defining energy windows for CT attenuation correction

Table 1 shows the 6 energy windows (EW A–B) that maintained $\Delta\mu/\mu_{mean} < 10\%$ for each of the 4 materials considered. The E_{low} and E_{high} limits were very similar for all 4 materials. The average E_{low} and E_{high} values are shown in the column of Table 1 labeled "Average$_{CT\text{-}AC}$". When considering BC, it is best to define the EWs such that the various spectral components are isolated in different EWs (e.g., the dual-EW technique uses 1 window for photopeak + scatter and a second window for scatter only). Since individual separation of 5 spectral components of bremsstrahlung is not possible because of its continuous nature, we adjusted the Average$_{CT\text{-}AC}$ windows to maximize separation between the various spectral components. These EW definitions are labeled "Nominal$_{AC,SC}$" and were selected as the acquisition EWs in this experiment. Based on the energy and spatial distribute`on analyses, EW B (90–125 keV) was determined to be the primary imaging window.

	Adipose	Soft Tissue	Muscle	Liver	Average$_{CT\text{-}AC}$	Nominal$_{AC,BC}$
CT #	−63.6	−4.4	40.1	48.7	n/a	n/a
A	70–90	70–90	70–90	70–90	70–90	70–90

B	90–130	90–125	90–125	90–125	90–126	90–125
C	130–175	125–180	125–170	125–170	126–174	125–160
D	175–235	180–245	170–230	170–230	174–235	160–215
E	235– 310	245–320	230–305	230–300	235–309	250–310
F	310–400	320–420	305–410	300–400	309–408	310–410

Table 1. The low and high photon energy limits of the 6 energy windows for < 10% change in the attenuation coefficient (Average$_{\text{CT-AC}}$) for adipose, soft tissue, muscle, and liver, and modified for energy window-based background compensation (Nominal$_{\text{AC,BC}}$). CT numbers are in HU units and energy windows A–F are in keV.

2.3.2. Choosing an appropriate imaging energy window

The calculated SBRs from the images acquired under different imaging conditions (scattering material thickness of 2−16 cm at 30 cm away from the MELP collimator and scattering material thickness of 4.8 cm at 15–35 cm away from the MELP collimator) exhibited similar patterns, i.e., the sphere-to-background ratio was the highest in EW B (~8.53), as shown in Fig 4.

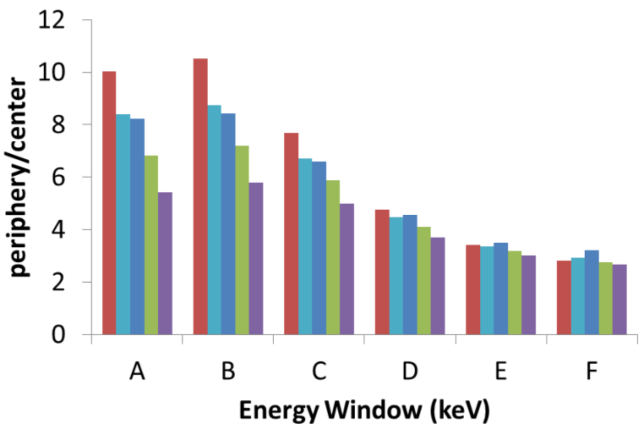

EW	SBR	
	mean	stdev
A	8.13	17%
B	8.53	17%
C	6.65	13%
D	4.50	9%
E	3.41	8%
F	2.97	12%

Fig 4. The signal-to-background ratios (SBR) of 6 energy windows (EWs) for the tested attenuating material thicknesses and source-to-collimator distance combinations, indicated by different bar colors. EWs A, B, and C had high signal-to-background ratios, i.e., they contained relatively high spatial information, whereas EWs E and F had low signal-to-background ratios, i.e., they contained relatively low spatial information. The means and standard deviations (stdev) of the SBRs for the EWs are shown in the adjacent table.

2.3.3. Developing empirical energy window-based background compensation for ^{90}Y bremsstrahlung imaging

The mean scaling coefficients ± 1 standard deviation for each BC model were 0.92 ± 0.04, 0.91 ± 0.05, 0.55 ± 0.05, 0.75 ± 0.09, 0.53 ± 0.07 for EWs A, C, D, E, and F, respectively. The coefficient of variance of the scaling coefficients was ~10%, which suggests that a fixed scaling coefficient factor may be implemented for BC in clinical images.

Using EW F for BC in SPECT/CT image reconstruction of the IEC phantom fulfilled both criteria: maximum SBR recovery and minimum lung insert residual activity; therefore, the EW-based BC for imaging EW B can be modeled as $\text{EW B} - 0.53 \times \text{EW F}$. Using this model, the SBR recovery coefficient for the 37-mm sphere of the IEC phantom was the highest at 87%, and the lung insert residual activity was the lowest at 14%, as shown in Fig 5.

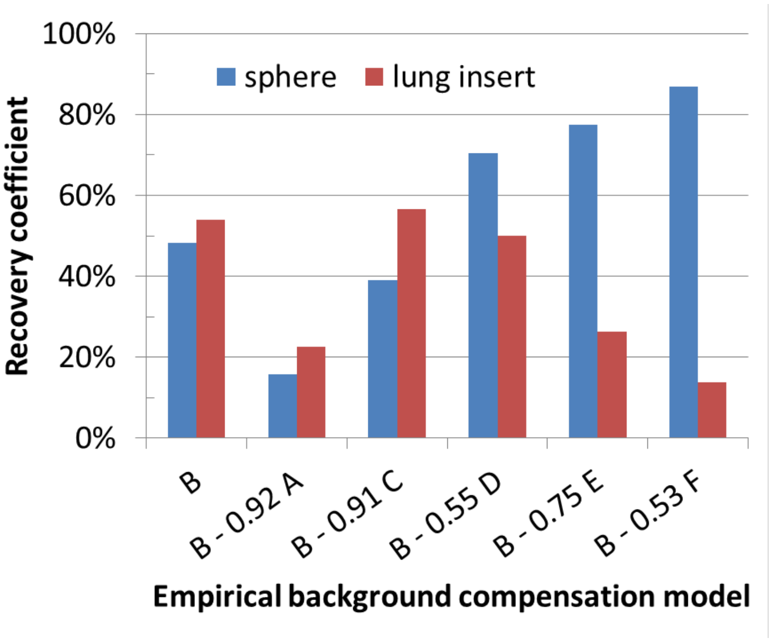

Fig 5. Recovery coefficients for 37-mm sphere and lung insert residual in the IEC phantom for SPECT/CT images reconstructed without background compensation and with 5 models of background compensation.

Fig 6 shows clinical examples of background-compensated planar images from 4 different patients. The BC improved the image contrast of the planar images. The tumors' detectability as measured by CNRs (shown beside selected tumors in Fig 4 increased after the application of the proposed BC. While the edges of the images still look fuzzy because of the inherently poor resolution of ^{90}Y, whose maximum beta range is 11 mm in water, improved delineation of the liver and liver lobes is apparent.

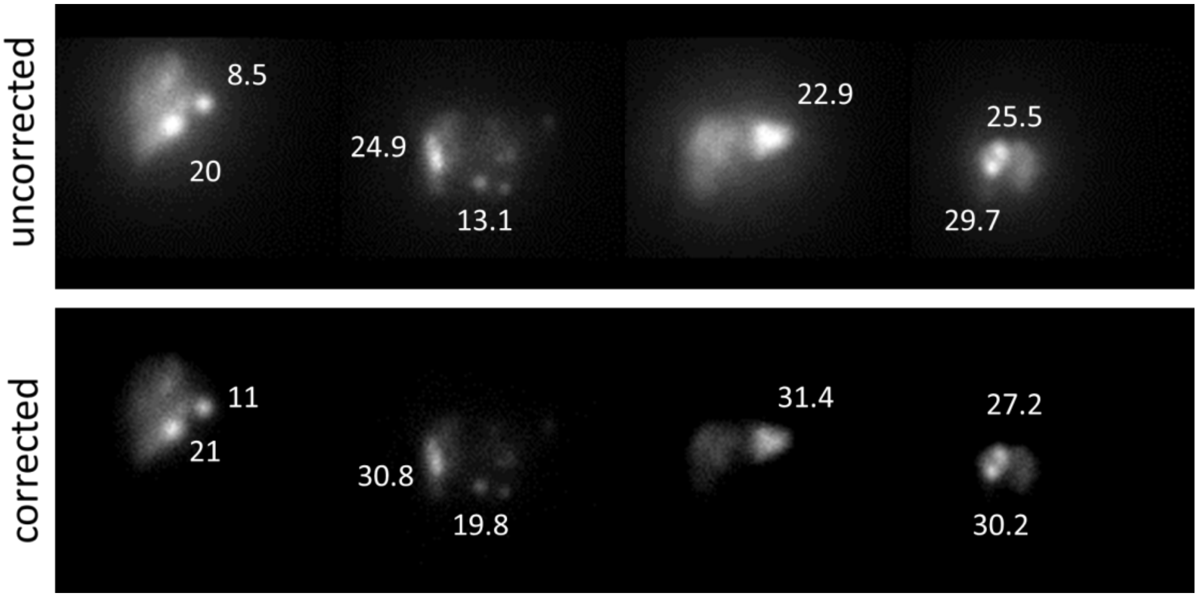

Fig 6. The uncorrected and background-compensated clinical images demonstrating that the energy window-based background correction improves the visualization of the liver and lesions. All images are shown using the same window width and level. The background-corrected images show improvement in the contrast-to-noise ratios of the lesions (inset numbers), which corresponds to improved visibility. The corrected images also exhibit improved liver and tumor delineation**.**

2.3.4. SPECT/CT activity calibration for quantification

For various reconstructed SPECT and planar images, the global calibration factors (gradients), their uncertainties (standard errors of the gradients), and the coefficients of determination (R^2) of the regression lines are presented in Table 2. In all cases, the total counts observed were proportional to the ^{90}Y activity in the FOV with $R^2 > 0.9$. As expected, the variations in the calibration factors exhibited the lowest variation in SPECT with AC + SC and the highest in SPECT-only and planar images.

The activity residual in EW B after linear regression is plotted in Fig 7; the standard deviations of the activity residuals were 11.3%, 5.6%, 5.2%, and 9.1% for SPECT only, SPECT with AC, SPECT with AC + SC, and planar images, respectively. Activity predictions using SPECT with AC and SPECT with AC + SC had lower variation than did predictions made using SPECT-only or planar images. The predicted activity in an IEC phantom using the global calibration factor derived from clinical scans introduced an error of −25% with respect to the true injected activity.

Image Type	R^2	CF (Bq/cps)	Std. Error (%)
SPECT	0.901	7.5	6.9%
SPECT AC	0.972	2.3	4.0%
SPECT AC + BC	0.982	4.0	2.8%
Planar	0.917	417.5	5.7%

Table 2. Results of the linear regression analysis of the relationship between total activity in the field of view and the corresponding total counts in the images. AC: attenuation correction, BC: background compensation, CF: calibration factor.

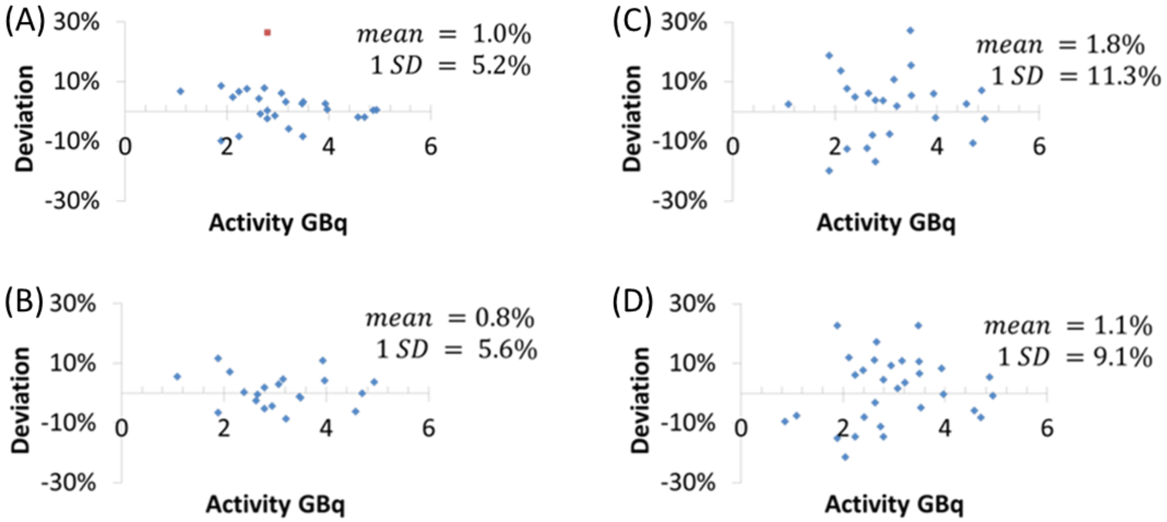

Fig 7. The activity residuals, defined as the difference between the true and predicted values relative to the true value, in EW B (90–125 keV) after linear regression. (A) Variations from SPECT/CT images with attenuation correction and background compensation. The mean and the maximum of the *absolute* deviation were 4% and 10%, respectively. The red square indicates the data point from the IEC phantom with a sphere-to-background ratio of 8. (B) Variations from SPECT/CT images with attenuation correction only. The mean and the maximum of the *absolute* deviation were 4.5% and 12%. (C) Variations from uncorrected SPECT images. The mean and the maximum of the *absolute* deviation were 9% and 27%, respectively. (D) Variations from total counts in opposing planar views. The mean and the maximum of the *absolute* deviation were 10% and 23%, respectively. SD: standard deviation.

2.3.5. Reconstruction-parameter optimization for qualitative and quantitative SPECT/CT images

2.3.5.1. Quantitative SPECT/CT imaging

The activity concentration and SBR recovery of the 37-mm sphere and the activity recovery in the background region in SPECT/CT images of the IEC phantom with CT AC + BC are shown in Fig 8. The background activity concentration converged rapidly (after 16 iterations), while the 37-mm sphere activity converged more slowly (after 128 iterations). The activity concentration in the background was fully recovered (~100%) at convergence and the activity concentration in the 37-mm sphere was partially recovered (90%) at convergence. The SBR recovery (87%) converged after 128 iterations as well. The measured activity concentration in the cold lung insert was calculated with respect to the background activity. The activity concentration in the cold lung insert vanished slowly as a function of total number of iterations. At 128 iterations, the activity concentration in the lung inserts was 14% of the activity concentration in the background.

As a comparison, at 128 iterations, the SPECT/CT images of the IEC phantom reconstructed using CT AC only had recovery of 39%, 82%, 48%, and 44% for the sphere, background, SBR, and lung insert, respectively.

The proposed BC method increased the activity concentration in the sphere and the SBR recovery by more than 2-fold (from 39% to 90%). The false-positive activity in the cold lung insert fell from 44% to 14%.

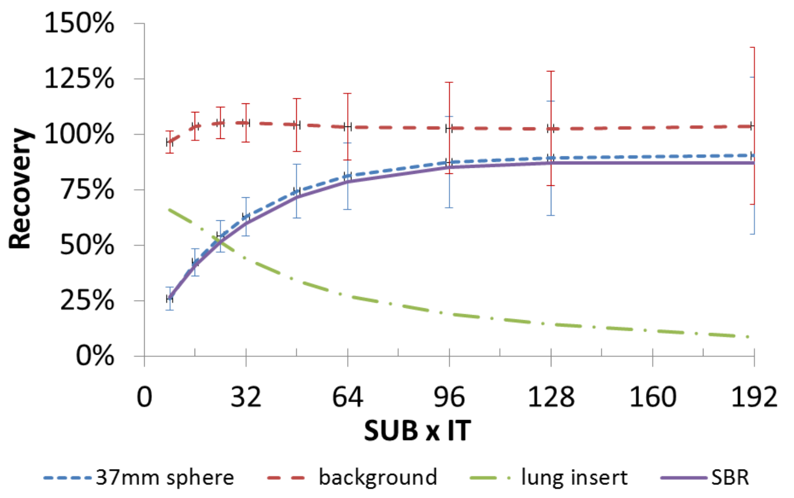

Fig 8. Recovery coefficients as a function of the total number of iterations. The background activity concentration reached 100% recovery rapidly (after 16 number of equivalent iterations). The activity concentration in the 37-mm spheres (using a 10mm-diameter VOI to minimize the partial volume effect) reached a plateau after 128 equivalent iterations (90% recovery). After 128 equivalent iterations, the signal-to-background ratio recovery also reached a plateau. The measured activity concentration in the cold lung insert was calculated with respect to the background activity. At 128 iterations, the activity concentration in the lung insert was 14% of the activity concentration in the background. The error bars indicate standard deviations for the volumes of interest. SUB: subset, IT: iteration.

2.3.5.2. Qualitative SPECT/CT images

As the number of equivalent iterations increased, the recovery of the activity in the sphere also increased. For OSEM reconstruction, however, the background noise also increased as a function of the number of equivalent iterations, as demonstrated by the growing error bars in Fig 8 as a function of the number of equivalent iterations. Fig 9 shows the 37-mm sphere detectability (measured as CNR) as a function of the number of equivalent iterations. The highest CNR, 25, was achieved at 16–24 number of equivalent iterations before the sphere activity concentration converged. At convergence (64 iterations), the CNR had decreased to 18 for SPECT with AC + SC and 13 for SPECT with AC. Visually, more spheres were detectable at lower iterations [Fig 9 (a)] than at higher iterations at convergence [Fig 9(b)]. SPECT with AC [Fig 9 (c)] had lower detectability than did SPECT with AC + BC.

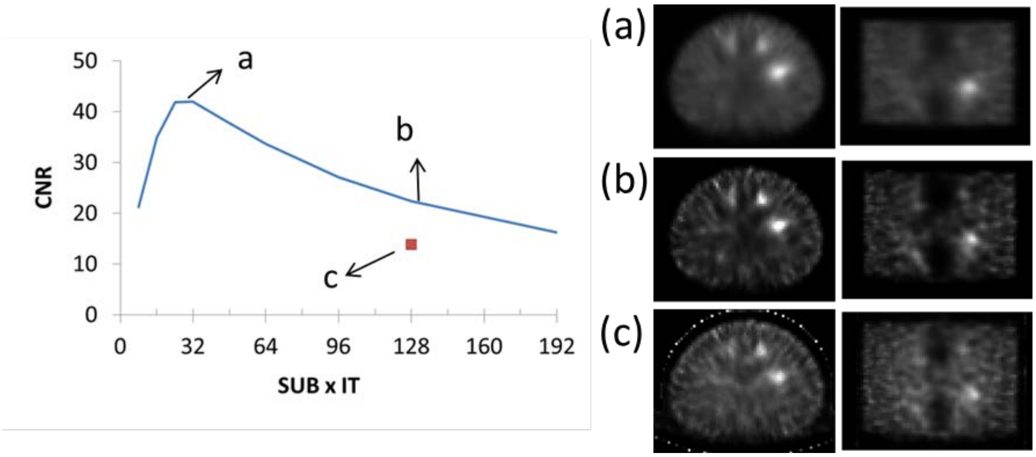

Fig 9. (left) Detectability (contrast-to-noise ratio, CNR) of the 37-mm sphere as a function of the number of equivalent iterations in SPECT/CT images with CT attenuation and background compensation (solid blue line). The red square indicates the CNR of the sphere for SPECT/CT images with CT attenuation correction only at convergence. (right) Transaxial and coronal images of the IEC phantom: (a) attenuation-corrected and background-compensated at the highest CNR (37-mm sphere), (b) attenuation-corrected and background-compensated at convergence (37-

mm sphere), and (c) attenuation-corrected at convergence. Attenuation correction and background compensation improved detectability [(b) versus (c)]. The highest detectability was achieved before convergence [(a) versus (b)]. In (b), the SBR was about 7, whereas the SBR in (c) was only about 3. SUB: subset, IT: iteration

2.4. Discussion

2.4.1. Limitation of the proposed background-compensation method

The proposed BC method is an empirical model. Monte Carlo simulation studies are required to accurately correct for specific components of scatter in the imaging EW. For example, Monte Carlo simulation studies[11,12] suggest that EW F (315–415 keV) may contain little or no object scatter information. Although our proposed BC method was not designed to correct for any specific source of contamination in the imaging EW B (e.g., object scatter, septal penetration, septal scatter, backscatter), we have shown that the proposed method increased both the CNR (detectability) and the accuracy of activity quantification.

The BC factor was derived for a Siemens Symbia T gamma camera with a 1.6-cm crystal and MELP collimator. Since energy window-based scatter correction is dependent on the energy spectrum, other makes and models of cameras with different crystal thicknesses and collimators will likely require different BC parameters, i.e., EW selections and BC scaling factors. The methodology described here, however, could be applied to develop BC models for ^{90}Y bremsstrahlung SPECT/CT imaging using other SPECT/CT systems. The readers are encouraged to use the procedure outlined here to determine the BC factors on their own systems prior to the clinical implementation of this technique.

2.4.2. Energy window selection

The signal-to-background ratio the highest in EWs A and B (and perhaps even C), which means that these EWs provided more spatial information in the image than did the other EWs. This finding is consistent with other studies that found that the optimal EW for qualitative ^{90}Y bremsstrahlung imaging was 80–180 keV.(54, 60) However, EW A was contaminated by the characteristic X-rays (70–90 keV) from the lead collimator and lead housing, so we chose EW B (the EW with the highest SBR) as the imaging EW of the ^{90}Y bremsstrahlung images.

However, the BC EW was chosen empirically based on the SBR recovery, as shown in Fig 5. Since EWs A and C had signal-to-background ratios comparable to that of EW B—that is, they contained good spatial information—using these EWs to compensate for background yielded a decrease in SBR recovery compared to using no BC.

To further validate our empirical method, two line profiles were extracted from the static images in EW B and EW F (Fig 10). One line profile was extracted across an image of a liver and the other one was drawn in the background region. The line profiles of the liver images showed that EW B provided much more spatial information of the liver image than did EW F. The line profiles in the background region suggest that the spatial distributions of the background signal were similar in EW B and EW F, supporting the usefulness of the proposed BC mode to compensate for the background signal.

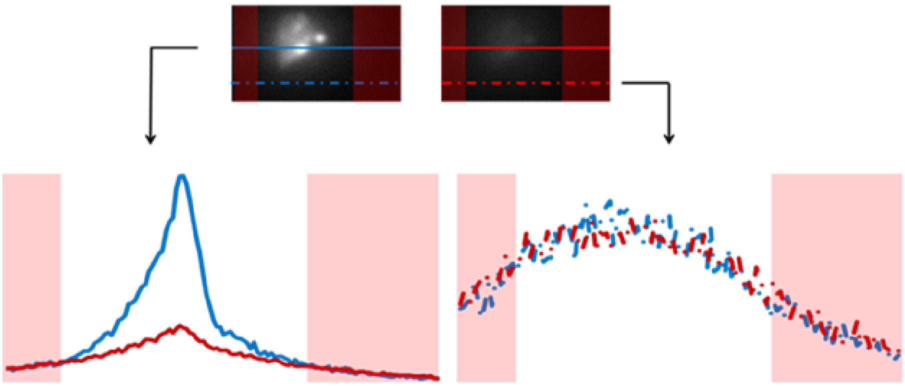

Fig 10. The images on the top are clinical images from Fig 6 in energy window (EW) B (left) and F (right) showing the locations from which the line profiles were extracted. The graphs at the bottom show line profiles in EWs B and F (scaled) across the liver image (left graph) and line profiles of EWs B and F (scaled) across the background region outside the liver (right graph). In the regions outside the liver (shaded), the background profiles in EWs B and F (scaled) are indistinguishable.

2.4.3. Partial volume effect and bremsstrahlung ^{90}Y quantitative accuracy

Yttrium-90 bremsstrahlung imaging using current commercially available gamma camera is hardware limited. The collimators used for nuclear medicine imaging are not designed for such high energy (up to 2.3 MeV) bremsstrahlung photon spectra of ^{90}Y. The observed events in the gamma camera have high contaminations from photons that have undergone septal penetration, septal scatter and backscatter that contribute to low image contrast. Furthermore, bremsstrahlung imaging has an inherent poor resolution due to electron staggering (up to 11 mm in soft tissue) in the bremsstrahlung production. These limitations may be addressed by optimizing(61, 62) the gamma camera collimator design for ^{90}Y bremsstrahlung imaging and by incorporating the physics model of electron staggering and bremsstrahlung photon generation in ^{90}Y SPECT/CT reconstruction using Monte Carlo simulation(27, 28, 63).

In order to minimize the interplay of the partial volume effect when assessing SPECT convergence, we used a VOI with 10-mm diameter to assess the recovery of activity concentration for the 37-mm sphere. As a result, up to 90% of the activity concentration in the 37-mm sphere was recovered at convergence. Qualitatively, as seen in Fig 9, spheres with diameter below 22 mm were not clearly visible in reconstructed ^{90}Y SPECT/CT images. As shown in Fig 11, the closer the VOI diameter is to the nominal diameter of the 37-mm sphere, the lower the recovery coefficient. Due to the partial volume effect, when using a VOI that matches the 37-mm sphere size, the recovery coefficient of 55% was realized. However, matched VOIs between CT and SPECT are needed for tumor dosimetry. Therefore, use of various published techniques to compensate for the partial volume effect will need to be employed for tumor dosimetry in clinical practice(64, 65). In contrast, the partial volume effect in ^{90}Y PET/CT is less pronounced. Recent ^{90}Y PET/CT quantitative studies(66, 67) have suggested that the recovery coefficient of 90% is achievable in a 37-mm sphere using a matching VOI size.

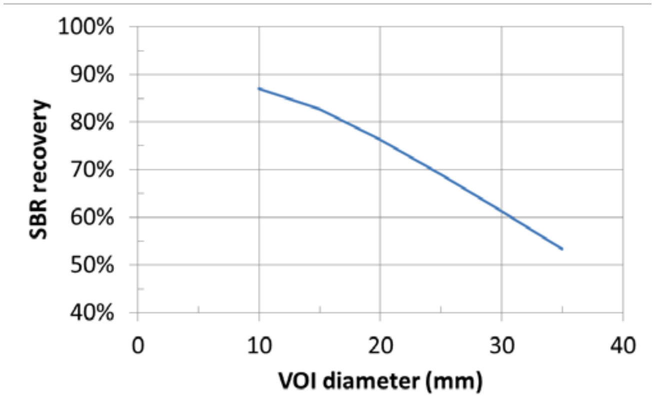

Fig 11. Graph of signal-to-background ratio recovery as a function of the diameter of the volume of interest (VOI). The SBR recovery decreases as the VOI diameter increases, demonstrating the partial volume effect.

2.4.4. Count-to-activity calibration factor derivation

The unique imaging conditions of ^{90}Y microsphere therapy permit SPECT/CT counts-to-activity calibration for generating quantitative ^{90}Y SPECT/CT images to be performed using clinical ^{90}Y images. SPECT images with CT AC + BC can be used to accurately quantify the activity present in the FOV with a mean absolute deviation $\leq$ 4%. Because the calibration factor determined using the IEC phantom demonstrated a substantial bias, caution is warranted when using an IEC phantom to calibrate SPECT/CT systems, since it may not accurately represent clinical imaging conditions in terms of attenuation and scatter.

2.4.5. Reconstruction parameter optimization

For OSEM reconstruction, the background noise also increases as a function of the number of equivalent iterations (Fig 8); therefore, the highest detectability (as measured by CNR) is usually achieved before the convergence (Fig 11). At convergence, even though the image quantification is more accurate, image detectability may actually be lower.

2.4.6. Correction for deadtime count loss

Because the yield of bremsstrahlung radiation in adipose and soft tissue (low-Z material) with a high energy spectrum is low, the number of detected photons is low; hence, gamma camera deadtime count loss is not an issue for post-therapy ^{90}Y SPECT/CT imaging. The number of total counts per activity was found to be linear (at least in the activity range of 1–5 GBq), providing further confirmation that the gamma camera does not suffer from deadtime count loss. If, however, correction for deadtime count loss is needed, the recently proposed revised monitor source method for practical deadtime count loss compensation can be employed. (68, 69)

2.5. Conclusion

We have proposed a practical method to reconstruct quantitative SPECT images with CT attenuation correction and empirical EW-based BC. For Siemens SymbiaT SPECT/CT systems, we found that EW B (90–130 keV) and EW F (310–400 keV) are the most appropriate to be used as the imaging and BC EWs. Despite our empirical correction method’s limitations, our phantom study shows that our reconstruction and compensation method improves both image quality and quantification.

Acknowledgments: Supported in part by Siemens Medical Solution USA and the NIH National Cancer Institute grant R01CA138986.

Chapter 3: Quantitative ^{90}Y-PET image reconstruction: optimization

3.1. Introduction

^{90}Y microspheres have been used for treating non-resectable liver cancer (48, 49). Current dosimetry standard for ^{90}Y-microspheres treatment planning, as recommended by AAPM (70) is the schema (71) developed by MIRD dosimetry that assumes uniform distribution in normal liver, tumor, and lung using partition mode (72) based on the surrogate ^{99m}Tc-MAA planar images. This simplistic model aims to calculate the mean organ absorbed dose for safe treatment planning (73).

In diagnosis nuclear medicine imaging, mean organ absorbed dose is the primary dosimetry metric of interest to evaluate population cancer risk from the imaging procedure. On the other hand, in (pre and post) therapy imaging, the dosimetry task aims to calculate normal tissue complication probability (NTCP) and tumor control probability (TCP) for the individual patient. These two RPT end points require the dose distribution information, which is beyond mean absorbed dose (40, 74); therefore there is a pressing need for volumetric dosimetry of ^{90}Y.

In the past decade, volumetric ^{90}Y dosimetry techniques have been implemented based on 3D ^{90}Y-activity distribution from both bremsstrahlung SPECT/CT (20, 51) and more recently from PET/CT (21, 35, 75) imaging. It has also been shown that local deposition method can be used to generate ^{90}Y dose map (Gy) by scaling the PET images (Bq/mL) using a single conversion factor (Gy/Bq/mL) (22, 35, 51). Since ^{90}Y PET/CT images have been suggested to have advantages over bremsstrahlung SPECT/CT in term of image contrast, resolution, and hence quantification ((24–26), in this work, we focus on ^{90}Y PET/CT to quantify volumetric ^{90}Y dose.

3D activity distribution that is observed in emission images is subject to image degrading factors such as partial volume effect, image noise, and motion blur (40). Consequently, the dose volume histogram calculated from these images (DVH') suffers from errors due to these degrading factors. While these degrading factors affect all nuclear medicine imaging, ^{90}Y PET imaging presents a unique challenge in that it has an extremely low signal, coming from 32 ppm of positron yield produced via internal pair production.

Several groups have used DVH' to summarize the information of 3D dose distribution estimated from ^{90}Y PET images (22, 23, 25). DVH (76) plots in the abscissa the minimum dose (D_x) that covers x% of the volume of interests (VOI) in the ordinate. The spread of the DVH curve around the median indicates the non-uniformity of the 3D dose distribution in the VOI (77). The two aforementioned RPT end points, i.e., TCP and NTCP can be calculated from DVH (78, 79). In practice, however, calculation of TCP and NTCP are complicated as they require radiobiological parameters that are difficult to determine from in vivo studies. Alternatively, empirical dose-response model have been derived by correlating DVH' summary metrics such as D_{95} in external beam therapy, D_{90} in brachytherapy, and recently D_{70} in ^{90}Y-microsphere studies (22, 23, 80–82). Even though PET/CT images have been increasingly used for volumetric dosimetry calculation, the impact of signal starvation on the errors, both systematic and random, in the resulting DVH' and it summary metric (e.g., D_{mean} and D_{70}) is poorly understood.

There has not been any standardization of ^{90}Y PET image acquisition and reconstruction. Recent studies on OSEM reconstruction-parameters optimization for quantitative ^{90}Y PET imaging (24, 36–39) still used mean-activity-concentration recovery coefficient as the objective function, which is more relevant to diagnostic dosimetry and detection tasks.

In this work, we aimed to optimize ^{90}Y-PET image-reconstruction protocol for volumetric ^{90}Y dosimetry—calculated as DVH'. We optimized the image-reconstruction protocol in a phantom studying using a modified NEMA IEC phantom study under a wide range of clinically relevant imaging condition: sphere sizes, activity concentrations, sphere-to-background ratios, and acquisition durations. While increase in equivalent number of iterations improves image resolution and quantification of mean activity concentration, it also increases the image noise. After convergence is achieved, increase in equivalent number of iterations only results in higher image noise. Application of Gaussian post-reconstruction filtration introduces image blurring and it can be used to reduce image noise; although it results in underestimation of the mean activity concentration with severity degree depending on the filter full width half maximum. Image noise and partial volume effect are major degrading factors that limit voxel-based dosimetry (40); hence, optimization of reconstruction parameters (equivalent number of iterations and post-reconstruction filtration FWHM) is imperative to improves the accuracy of DVH estimates calculated from noisy ^{90}Y PET images (DVH').

3.2. Methods

We used a modified NEMA IEC phantom (Biodex, Shirley ,NY) to emulate clinically relevant ^{90}Y PET imaging conditions thru various combinations of acquisition durations, sphere activity concentrations, sphere-to-background ratios (SBR), and sphere sizes. The modified IEC phantom contains 2 sphere sets of diameters 37, 17, 13 mm each. These sphere were filled with ^{90}Y activity concentrations (AC) of 4.8 MBq/cc (130 uCi/mL) and 1.6 MBq/mL (43 uCi/mL); the background chamber was filled with 0.4 MBq/mL (10 uCi/mL) to give SBR of 13 and 4.

PET data of the IEC phantom were acquired in list-mode using GE D690 PET/CT scanner for 300 min in 1-bed position. To optimize the quantitative image reconstruction, PET images were reconstructed using various parameter sets. All PET images (AC map in Bq/mL) were multiplied by a scaling factor of 4.78×10^{-5} Gy.mL/Bq to convert the PET images to ^{90}Y dose map (Gy) via local deposition method (35).

To evaluate the variation of optimum reconstruction parameters under a range of image noise, we replayed the list-mode PET data to 60, 45, 30, 15, and 5 min with 10 different realizations each. We also acquired the PET list-mode data on day 0 (sphere ACs of 4.8 and 1.6 MBq/mL) and on day 3 (sphere ACs of 2.3 and 0.8 MBq/mL) to assess variation in reconstruction due to dose rate during acquisition.

The PET/CT images were reconstructed using 3D-OSEM with PSF+TOF modelling (VPFXS). The voxel size was $2.6 \times 2.6 \times 3.3$ mm^3. Assuming local energy deposition, the corresponding known doses of the sphere sets were 230 and 77 Gy on day 0 and 110 and 37 Gy on day-3 acquisition. We optimized the image reconstruction parameter using both recovery coefficient (RC) of mean dose (section B.1.1) and minimum errors in volumetric ^{90}Y dose quantification (section B.1.2) as the objective functions.

3.2.1. Reconstruction optimization based on recovery-coefficient convergence

The reconstruction parameter optimized in this sub section was the number of equivalent iterations (subsets × iterations); where the objective function of the optimization was recovery coefficient (RC) of mean sphere dose. PET images were reconstructed using fixed subset of 12 and varying iterations of 1–12.

The sphere RCs were calculated as RC = D_{mean}/D_{true}; where D_{mean} is the mean dose in the sphere computed from CT-contoured VOI, and D_{true} is the known absorbed dose in the sphere calculated based on the injected ^{90}Y activity.

The convergence properties of sphere RC were evaluated under aforementioned various imaging conditions: acquisition durations (300–5 min), sphere dose (230–37 Gy), SBR (13 and 4), and sphere sizes (37, 17, and 13 mm). RC convergence was determined by calculating sphere RC as a function of number of equivalent iterations for images with no post-reconstruction filtration.

3.2.2. Reconstruction optimization based on errors in dose volume histogram estimates

Here, the reconstruction parameters optimized were both the number of equivalent iterations and the full width at half maximum (FWHM) of the post-reconstruction Gaussian filters. PET images were reconstructed using fixed subset of 12 and varying iterations of 1–12. The post-reconstruction Gaussian filters in the transaxial plane were varied from 0, 2.6, 5.2, 7.8, and 10.4 mm. The PET images (Bq/mL) were converted to dose map (Gy) and were corrected for dose-dependent systematic error in volumetric ^{90}Y dose (Chapter 4).

We optimized the image-reconstruction parameters for sphere (tumor) dose quantification; therefore the volumetric dose distribution in the all sphere sets (13, 17, and 37-mm spheres with SBR of 13 and 4) were quantified using dose volume histogram estimate (DVH'). The optimization objective function was minimum errors in the sphere DVH'.

Sphere DVH' were derived from matching-sized volumes of interest (VOI) that were contoured from CT sphere images, e.g., DVH' in the 17-mm sphere was derived from 17-mm spherical VOI. Errors in the DVH' were calculated as root mean square errors (RMSE) of the differences in the image-based sphere DVH' and the true DVH, i.e., $RMSE = \sqrt{\frac{\sum_{20}^{80}(D_x - D_{true})^2}{60}}$; where D_x is the minimum dose that covers x% of the VOI, and D_{true} is the known dose based on injected ^{90}Y activity. The true DVH was calculated for uniform sphere dose distribution as such that D_x for all volume coverage, x, equal to D_{true}. RMSEs were calculated from D_{80} to D_{20} to avoid high errors near the maximum (D_0) and minimum (D_{100}) doses due to both systematic and random errors (section C.3.). RMSE for each sphere DVH' was calculated as an average of 10 different image noise realizations; the standard errors were also reported. RMSE was calculated for all image-reconstruction-parameter combinations (equivalent iterations and filtration FWHM) under the same variation of imaging condition in section 3.2.1.

3.3. Results

3.3.1. Reconstruction optimization based on recovery-coefficient convergence

The convergence rates of VPFXS algorithm were found to be insensitive to various imaging conditions tested: sphere sizes, SBR, sphere dose (activity concentration), and acquisition duration. Fig 12 demonstrated this convergence rate invariance for sphere with SBR of 13, sphere diameters of 37, 17, and 13 mm, and sphere dose of 230 and 77 Gy. Spheres with various imaging condition achieved RC convergence after 36 equivalent iterations. The systematic and random errors in converged RC were characterized in Chapter 4.

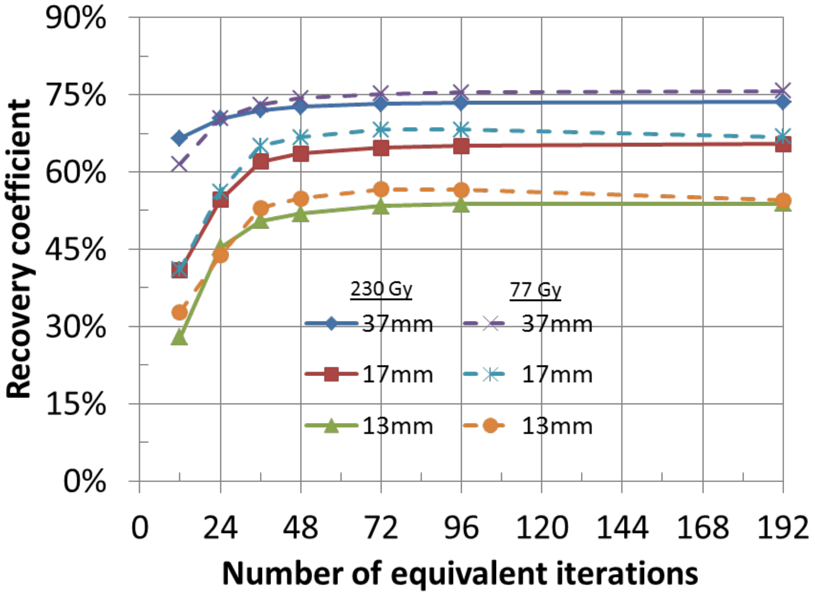

Fig 12. Mean dose recovery coefficient (RC) plotted as a function number of equivalent iterations (subset × iterations) for sphere with sphere-to-background ratio of 13, sphere sizes of 37, 17, and 13 mm, and dose levels of 230 and 77 Gy.

3.3.2. Reconstruction optimization based on errors in DVH'

We found that images reconstructed using equivalent iterations of 24–48 and filtration FWHM of 5.2–7.8 mm, RMSE of sphere DVH' were consistently among the lowest in various tested imaging conditions.

Fig 13 shows the DVH' for 17-mm sphere images (SBR of 13, dose of 230 Gy, duration of 30 min) reconstructed using various equivalent iterations (Fig 13A) and various filtration FWHM (Fig 13B). Their RMSE of DVH’ are shown in Fig 13C as a function of equivalent iterations and filtration FWHM. The standard errors of selected DVH’ RMSE are also shown as the error bars. RMSEs of DVH’ were among the lowest at 36 equivalent iterations; further increase in the number of equivalent iterations beyond 36 resulted in higher noise, as evident in the increase spread of DVH’ (longer tails on both ends). Similarly, the RMSE of DVH’ was the lowest with filtration FWHM of 5.2 mm. Heavier filtration shifted the DVH’ toward lower dose and resulted in higher underestimation of DVH’.

The DVH’ RMSE in a larger sphere image (37 mm in diameter) was the lowest at equivalent iteration of 24, while the RMSE in a smaller sphere image (13 mm in diameter) was the lowest at 48 equivalent iterations. However image reconstruction of all spheres (diameter of 37–13 mm) using 36 equivalent iterations resulted in change of absolute errors in DVH’ of < 1% at all volume coverage (Fig 13A and Fig 13C).

As the sphere image noise/non-uniformity increases due to lower dose or shorter duration, 7.8-mm filtration resulted in lower RMSE of DVH’ than did images with 5.2-mm filtration. Changes in 17-mm sphere (77 Gy) DVH’ calculated from sphere images (15-min duration) with 5.2 and 7.8-mm filtration were < 3% at volume coverage between 20–80%, on average.

While application of image filtration suppresses image noise and hence reduces noise-dependent errors in DVH, it also increases the errors in DVH due to increased partial volume effect. Heavier filtration with FWHM of 7.8 and 10.4 can be used on larger sphere (37-mm sphere), where partial volume effect is less severe, to further reduce the RMSE of DVH estimate; heavier filtration beyond 7.8-mm FWHM, however, did not significantly improve the DVH’ (< 2% absolute change at all volume coverage). In contrast, application of filtration with FHWM wider than 5.2 mm increased the RMSE of DVH’ in smaller spheres, e.g. in 17-mm sphere (Fig 13B and Fig 13C).

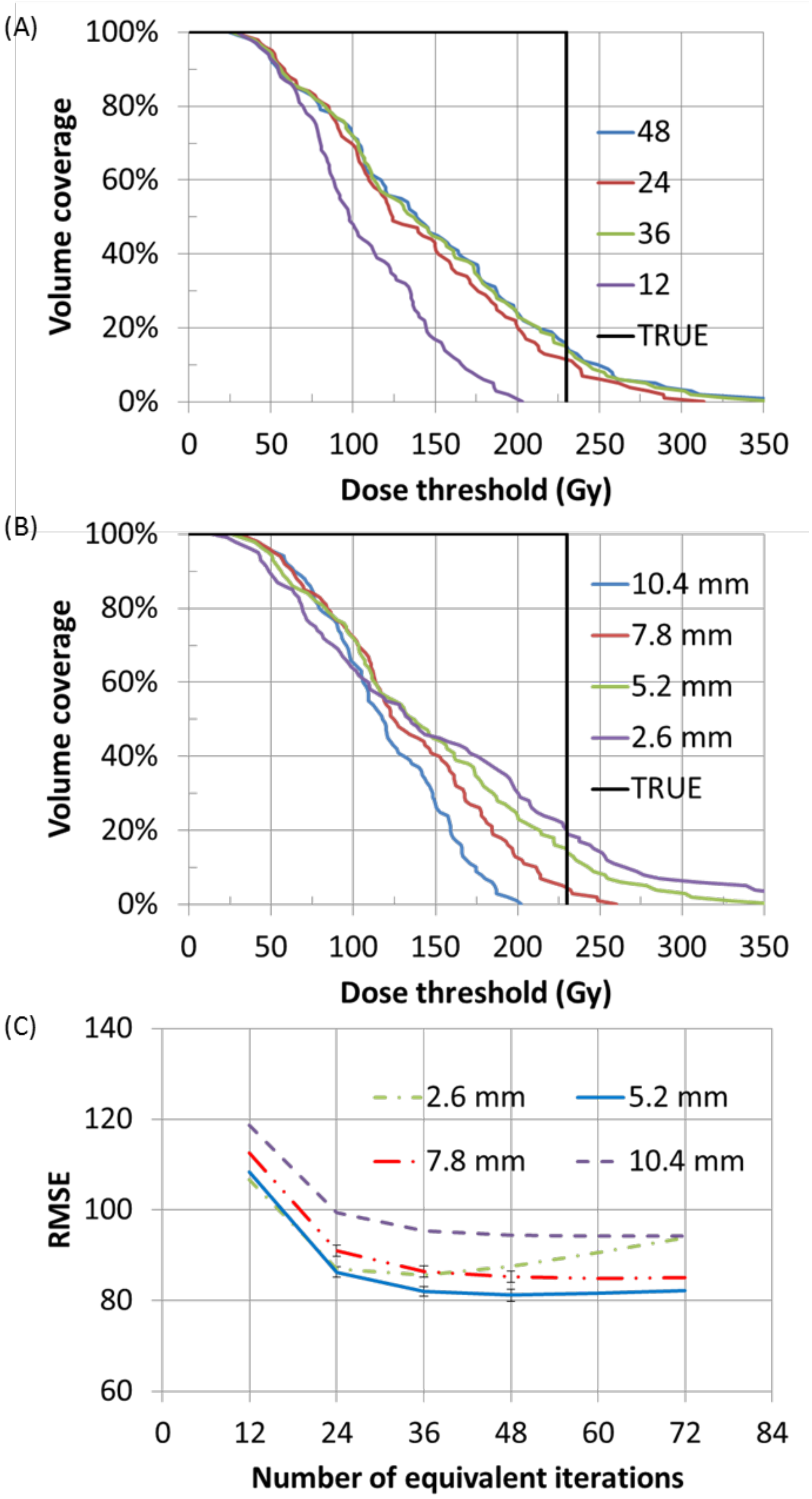
(A)
Volume coverage
100%
80%
60%
40%
20%
0%
0
50
100
150
200
250
300
350
Dose threshold (Gy)
48
24
36
12
TRUE
(B)
Volume coverage
100%
80%
60%
40%
20%
0%
0
50
100
150
200
250
300
350
Dose threshold (Gy)
10.4 mm
7.8 mm
5.2 mm
2.6 mm
TRUE
(C)
RMSE
140
120
100
80
60
0
12
24
36
48
60
72
84
Number of equivalent iterations
2.6 mm
5.2 mm
7.8 mm
10.4 mm

Fig 13. Dose volume histogram estimates (DVH') of 17-mm sphere (230 Gy) calculated from 15-min sphere images reconstructed with (A) equivalent iterations of 12–48 (filtration full width at half maximum [FWHM] of 5.2 mm) and (B) from images reconstructed with FWHM of 2.6–10.4 mm (equivalent iteration of 36). The black curve indicates the adjusted reference DVH. (C) The root mean square error (RMSE) of DVH' as a function of equivalent iterations and filtration FWHM for 17-mm sphere image (230 Gy, 15 min).

3.4. Discussion

3.4.1. RMSE dependence on dose threshold selection

To determine the sensitivity of RMSEs to selection of dose threshold ranges, we also investigated the random error in RMSE trends as a function of dose threshold ranges: $D_0 – D_{100}$, $D_{10} – D_{90}$, $D_{20} – D_{80}$, $D_{30} – D_{70}$, $D_{50} – D_{80}$, $D_{60} – D_{90}$. As expected, using the entire dose threshold range from D_0-D_{100}, the RMSE was the lowest when using lower number of equivalent iterations to avoid high errors due to noise near the extreme doses. The resulting DVH, however, yields higher errors in more useful dose metrics, e.g. D_{20}-D_{80}, as shown in Fig 13 and Fig 14. RMSE calculation using other dose threshold ranges between D_{10}-D_{90} results in similar RMSE trend as a function of equivalent iterations, i.e., RMSE was the lowest at 36 equivalent iterations with 7.8-mm filtration (Fig 14). We chose dose threshold range of D_{20}-D_{80} as a conservative approach to avoid noise-related errors near the extremes, which cause both high errors (Fig 13) and high random error (**Fig 21**A).

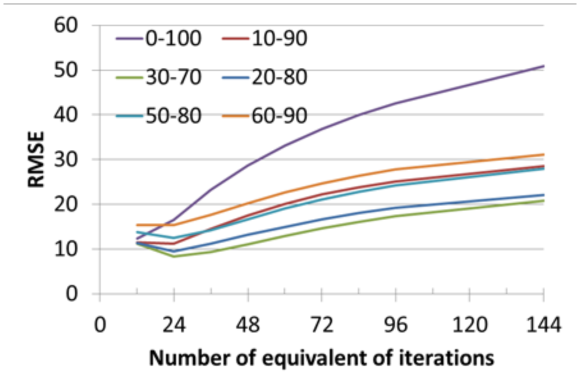

Fig 14. Root mean square errors (RMSE) of 17-mm sphere (110 Gy) dose volume histogram (DVH) estimate for various dose threshold ranges. Using the entire range D_0–D_{100} results in an optimization systematic error where low number of equivalent iterations is preferred to avoid high errors due image.

3.4.2. Comparison of optimization objective functions: traditional mean dose RC versus DVH' RMSE.

As the numbers of equivalent iterations increases, the sphere images begin to converge, but the image noise increases as well. Transaxial filtration can be used to reduce the image noise, but it blurs the image, which results in changes in dose distribution (smeared) with degree of severity depending on the FWHM of the filtration and the sphere sizes.

Optimization using mean dose RC does not take into account the alteration in dose distribution due to changes in image noise: increase noise from higher number of equivalent iteration and reduced noise from higher filtration FWHM. Since spatial filtration reduces the mean dose RC, reconstruction-parameter optimization using mean dose RC as the objective function would suggest minimum filtration. As shown in Fig 13, sphere images with no/low filtration resulted in higher errors in DVH.

While the standard deviation of the mean dose RC can be used to minimize the increase noise from higher number equivalent iteration, it cannot be used to optimize the FWHM of the filtration. Wider FWHM filtration will monotonically result in lower standard deviation.

Although in clinical practice, post-reconstruction filtration is usually applied to 90Y PET images, the FWHM of the filtration is not being optimized for volumetric quantification task. Post reconstruction filtration is normally considered to improve detection only. In this work, we showed that filtration can be used to improve volumetric quantification; therefore for volumetric quantification task, the FWHM of the filtration applied to the 90Y PET images need to be optimized (or verified) based on minimum errors in the DVH.

3.4.3. Study limitation

This study was limited to phantom studies using a modified NEMA IEC phantom. Spheres with uniform dose were not true representations of heterogeneous ^{90}Y-microsphere distribution in the tumor. Future studies using a physical phantom (83) with inhomogeneous ^{90}Y distribution are needed to further evaluate the errors in volumetric ^{90}Y dosimetry calculated from ^{90}Y PET images.

3.5. Conclusion

Using DVH' as an objection function allows optimization of both number of equivalent iterations and FWHM of the post-reconstruction filtration. We recommend using 36 equivalent iterations with 5.2-mm filtration for ^{90}Y-PET image reconstructed using VPFXS (GE OSEM with TOF and PSF).

Chapter 4: Quantitative 90Y-PET image reconstruction: systematic (bias) and random (variability) errors.

4.1. Introduction

This chapter is a continuation from Chapter 3, where we used the optimized image-reconstruction protocol discussed in Chapter 3 to generate ^{90}Y dose map of the modified IEC phantom. In this chapter, we characterized the systematic and random errors in the resulting sphere DVHs'. We evaluated the dose-dependent systematic error in quantitative ^{90}Y PET images (in GE D690/D710) that have been reported by several groups on different PET scanner makes and models (37, 39, 66, 84). Then we assessed the unique challenge in ^{90}Y PET, i.e., very low signal acquired. Low signal introduces increased non-homogeneity (image noise) in dose distribution, resulting in systematic error in DVH'. In addition, low signal also increases the random errors in DVH' measurement, both of which contribute to total error in DVH', consequently reducing the predictive value of dose-response model.

In clinical practice, the dose metrics are calculated from a single measurement (e.g. PET image set). Dose metrics used to predict tumor response ideally should have very high correlation to response metric and have low errors (systematic and random) so as to maintain clinically acceptable predication intervals. These PET based metric with high errors will, despite their high correlation, will have large prediction intervals; hence we need to trade-off the degree of correlation and the errors in the dose metric used.

Mean tumor dose (Dmean) has been shown to have correlation with tumor response (73, 85). However, in tumor with heterogeneous dose distribution, the correlation between mean dose and response will be weaker. Minimum dose (D_{100}) to tumor, in principle, would have the highest correlation with tumor response. Minimum dose, however, is prone to errors (contouring uncertainty, noise in image-based dosimetry, etc). Due to this uncertainty in minimum dose, dose metrics will less errors (despite lower correlation, theoretically) are being used in radiation oncology (for example, D95 in external beam therapy, D90 in brachytherapy). Therefore, accurate measurement of DVH for 90Y therapies are needed and then those metric need to be correlated with response to establish the appropriate dose metric for SIRT; there are some suggestions that D70 is of clinical relevance in 90Y SIRT.

The correlation between dose and response metrics require clinical data, which we currently do not have. Errors in the dose metrics, however, can be studied in phantom study acquired under clinically relevant imaging condition. In our study, we characterized the errors of dose volume histogram (DVH) metrics at volume coverage of 20–80% and Dmean, depending on the noise level, is at D20–D50%. The findings in our study will help future study by providing some reference 1) in calculation of sample size needed to determine statistically meaningful dose-response model, and 2) in the confidence interval of dose metrics calculated from a single measurement (from patient images/dose map). Information about the overall errors of the dose metrics can be used as a reference to compare the predictive power of different dose-response models (e.g., Dmean -response vs D80-response).

4.2. Methods

We used a modified NEMA IEC phantom (Biodex, Shirley ,NY) to emulate clinically relevant ^{90}Y PET imaging conditions thru various combinations of acquisition durations, sphere activity concentrations, sphere-to-background ratios (SBR), and sphere sizes. The modified IEC phantom contains 2 sphere sets of diameters 37, 17, 13 mm each. These sphere were filled with ^{90}Y activity concentrations (AC) of 4.8 MBq/cc (130 uCi/mL) and 1.6 MBq/mL (43 uCi/mL); the background chamber was filled with 0.4 MBq/mL (10 uCi/mL) to give SBR of 13 and 4.

PET data of the IEC phantom were acquired in list-mode using GE D690 PET/CT scanner for 300 min in 1-bed position. To optimize the quantitative image reconstruction, PET images were reconstructed using various parameter sets in section B.1. For the rest of the study (section B.2.—B.3.), all PET images were reconstructed using the optimal parameter set derived in section B.1.

All PET images (AC map in Bq/mL) were multiplied by a scaling factor of 4.78×10^{-5} Gy.mL/Bq to convert the PET images to ^{90}Y dose map (Gy) via local deposition method (35).

4.2.1. Dose-dependent systematic error in volumetric ^{90}Y-dose quantification

To separate the errors due to prompt rate and prompt count, we compared the errors in mean dose as the ^{90}Y activity decayed (rate and count effect) to the errors as the acquisition duration decreased (count effect only). We acquired 300-min list-mode PET data of the modified ^{90}Y IEC phantom for 11 consecutive days. As the ^{90}Y activity decayed, both the total prompt rate and the total prompt counts decreased. We also down-sampled the 300-min list-mode data to shorter duration: 120, 60, 20, 10, 5 min. For images with 60–5min duration, we down-sampled them at 10 different noise realizations.

For all images, the mean dose (with no partial volume effect [PVE]), $D_{\text{mean, no PVE}}$, was computed as the mean dose in 37-mm sphere images calculated using a 17-mm VOI to minimize PVE and random error due to VOI placement. We also computed the mean dose in the background region as an average of $D_{\text{mean, background}}$ from 5 17-mm VOIs scattered in the background region. The errors in $D_{\text{mean, no PVE}}$ and $D_{\text{mean, background}}$ were calculated with respect to D_{true}, i.e., $1 - D_{\text{mean,no PVE}}/D_{\text{true}}$. For the 300-min images at different dose level (different days), we used polynomial data fitting to model the errors as a function of D_{true} for mean dose in both 37-mm spheres (SBR of 13 and 4) and the background. This empirical model was used to correct for the dose-dependent systematic error in $D_{\text{mean, no PVE}}$. We quantified the errors in DVH' calculated from sphere dose distribution with and without the empirical dose-dependent systematic error correction.

For the images with reduced durations, we only characterize the errors as a function of D_{true} for mean dose in 37-mm spheres with SBR of 13. The errors were calculated as an average of errors in 10 noise realizations, and their standard errors were also calculated. The relationships between the errors in $D_{\text{mean, no PVE}}$ and the known dose were compared in both activity decay and acquisition duration reduction using linear regression method.

The volumetric dose distributions of spheres with different activity (dose) level but comparable number of true prompt event were compared to assess if there were alteration in the dose distribution beyond the systematic error in $D_{\text{mean, no pve}}$. We selected several 37-mm sphere images at different dose levels (e.g., 230, 100, 11 Gy) and we matched the number of true prompt event level by varying the acquisition duration (e.g., 15, 30, 300 min, respectively) such that the product dose and acquisition duration were comparable. The DVH' of these 37-mm sphere images were calculated from 17-mm VOI and normalized such that the area under the curve equaled to unity. Agreement of the normalized DVH was measured as the (max-min)/average at all volume coverage, i.e., D_0 to D_{100}.

4.2.2. Comparison between ^{90}Y and equivalent ^{18}F studies

A total of 111 kBq (3 μCi) of ^{18}F was injected into the modified IEC phantom (SBR of 11 and 3) to simulate the inherent low count and high random fraction (random event/total prompt) typical of ^{90}Y studies. ^{18}F activity of 3 μCi resulted in positron emission rate of 108 kcps, which was equal to the positron rate from 3.37 GBq (91 mCi) of ^{90}Y activity. PET list-mode data of this ^{18}F phantom were acquired for 12 hours and were down-sampled to 12 × 30-min separated by 1 hour each. The 300-min PET-list mode data (day 1 to day 11) for similar ^{90}Y phantom study were down-sampled to 10 contiguous 30-min scans to match the scan duration for ^{18}F.

All ^{18}F PET images were reconstructed using the same optimized parameters used to reconstruct ^{90}Y PET images (section B.1.). At each time point, we calculated the mean absorbed dose, $D_{\text{mean, no pve}}$, in 37-mm sphere (SBR 11) from 17-mm VOI and we also calculated their errors with respect to the known dose from assay. Errors in $D_{\text{mean, no pve}}$ were characterized as a function of known positron emission rate and compared to the errors in $D_{\text{mean, no pve}}$ from ^{90}Y study using linear regression analysis to determine the correlation between the errors and the positron emission rate (activity). In addition, we also compared the total prompt and number of random events (retrieved from the DICOM tags) in both ^{18}F and ^{90}Y studies as a function of positron emission rate.

To measure the contribution of internal background radiation from lutetium-176 yttrium orthosilicate (LYSO) crystal, we acquired an 8-hour blank scan of the background radiation with just air in the FOV. The number of random events in 30-min acquisition was calculated to match the acquisition duration of ^{18}F and ^{90}Y studies.

4.2.3. Impact of low signal on volumetric ^{90}Y dose quantification

To investigate the impact of low signal acquired on accuracy and random error of the sphere DVH', we varied the number of true event acquired by reducing the acquisition duration. The 300-min list-mode PET data were down-sampled with multiple noise realizations to 5 × 60 min, 6 × 45 min, 10 × 30 min, 10 × 25 min, 10 × 20 min, 10 × 15 min, 10 × 10 min, 10 × 5 min. PET images were reconstructed using optimized reconstruction parameters for post-therapy quantitative ^{90}Y PET imaging (Chapter 3). The PET images were converted to dose map and were corrected for dose-dependent systematic error (Chapter 4.2.1)

4.2.3.1. Impact of image noise on volumetric ^{90}Y dose quantification accuracy

The impact of noise in accuracy of both differential (more intuitive approach) and cumulative dose histogram estimates (DVH') were evaluated in sphere images with minimal PVE. VOI with 17-mm diameter was used to calculate DVHs' in the 37-mm sphere (SBR 13, 230 Gy) images with various durations. At each duration, the DVH' were calculated as averages of multiple noise realizations. The magnitude of errors in DVH' due to noise (minimal PVE) were compared to the errors from PVE (low noise). DVHs' were calculated from the 300-min sphere images (low noise) for both 37- and 17-mm using VOI with matching sizes to appreciate the PVE.

DVH' accuracy in clinically relevant imaging condition was evaluated in the presence of both PVE and image noise. The 300-min list-mode PET data (11-consecutive day acquisition) were down-sampled to 10 × 30 and 10 × 10 min for each day, spanning known sphere dose of 11–230 Gy. The tumors were emulated using the 37- and 17-mm spheres. Sphere DVH' were calculated as an average of 10 noise realizations and were calculated using matching-size VOI. DVH' accuracy were characterized as a function of known dose at D_{mean}, D_{80}, and D_{20} for both sphere sizes and acquisition durations.

4.2.3.2. Impact of low signal on volumetric ^{90}Y dose quantification random error

We evaluated the data from Chapter 4.2.3.1. The random error of the DVH' was calculated as the coefficient of variance (COV = standard deviation/average) of D_x for all volume coverage, x, in10 noise realizations. We calculated the COV of D_x in 37- and 17-mm sphere images acquired for 30 and 10 min. The maximum COV of D_x (for $20 \leq x \leq 80$) was characterized as a function of known dose.

4.3. Results

4.3.1. Dose-dependent systematic error in volumetric ^{90}Y-dose quantification

We observed a non-linear relationship between known dose and measured volumetric dose quantification in both spheres and background VOI. Fig 15A shows measured $D_{mean,no\ pve}$ in 37-mm spheres and background region as a function of known $D_{true.}$ $D_{mean,\ no\ pve}$ in both spheres and background VOI showed quadratic relationship ($0.0005x^2 + 0.72x - 1.42$) with the D_{true}; where x is decay corrected D_{true}. Consequently, the errors in measured $D_{mean,\ no\ pve}$, calculated as $D_{mean,\ no\ pve}/D_{ref}$ -1, showed dose-dependent systematic error that was consistent with quadratic relationship, i.e., ($0.0005x + 0.72 - 1.42/x$), shown in Fig 15B. In contrast, the errors in $D_{mean,\ no\ pve}$ calculated from sphere images with reduced duration did not exhibit noise-dependent errors (Fig 15C). The standard errors of the errors in $D_{mean,\ no\ pve}$ for 60 to 5-min images were < 0.5%, shown but not visible in Fig 15C. The slope of the errors vs. fractional count (duration) was consistent with zero with p value $>> 0.05$, while the slope of the errors vs. fractional count (activity) was clinically significant with p value $<< 0.05$.

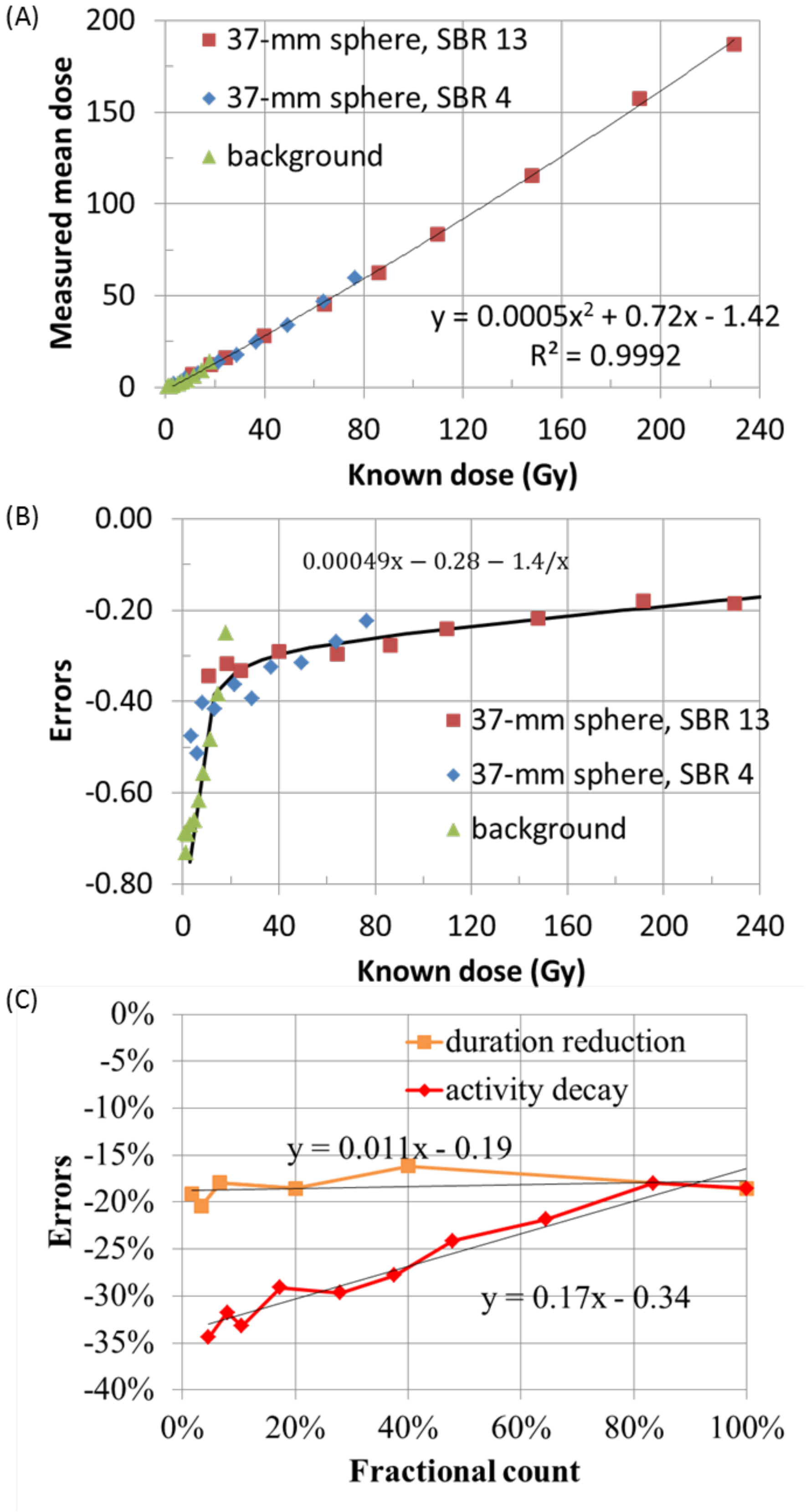
(A)
37-mm sphere, SBR 13
37-mm sphere, SBR 4
background
Measured mean dose
Known dose (Gy)
y = 0.0005x² + 0.72x - 1.42
R² = 0.9992
0
50
100
150
200
0
40
80
120
160
200
240
(B)
0.00049x − 0.28 − 1.4/x
Errors
Known dose (Gy)
37-mm sphere, SBR 13
37-mm sphere, SBR 4
background
0.00
-0.20
-0.40
-0.60
-0.80
0
40
80
120
160
200
240
(C)
duration reduction
activity decay
y = 0.011x - 0.19
y = 0.17x - 0.34
Errors
Fractional count
0%
-5%
-10%
-15%
-20%
-25%
-30%
-35%
-40%
0%
20%
40%
60%
80%
100%

Fig 15(A) Measured mean absorbed dose $D_{\text{mean, no pve}}$ (with minimal partial volume effect) in sphere and background regions as a function of known dose (from assay) showing a quadratic relationship. (B) The errors in $D_{\text{mean, no pve}}$ as a function of known dose showing an dose-dependent errors in $D_{\text{mean, no pve}}$. (C) Comparison of error trends in $D_{\text{mean, no pve}}$ of 37-mm sphere (SBR 13) vs. fractional count. The fractional count is varied by reducing the acquisition duration (orange line) and by letting the activity decay (red line).

The alteration in volumetric ^{90}Y-dose quantification due to this dose-dependent systematic error was found to be scalar, i.e., the relative dose distribution was not varied by this dose-dependent systematic error, as evident in the agreement in normalized DVH' of sphere images at different dose level (different errors) with equivalent noise. Fig 16A shows that the normalized DVH of 37-mm sphere with dose of 230, 100, and 11 Gy agree within 4%, which was consistent with their measurement random error (Chapter 4.3.3.2.). The dose-dependent errors in $D_{\text{mean, no pve}}$ were -20%, -24%, and -34% for sphere dose of 230, 100, and 11 Gy, respectively.

Fig 16B shows the DVH' (minimum partial volume) of 37-mm sphere (known dose of 110 Gy) for acquisition duration of 30 min with and without correction for dose-dependent systematic error. After the correction for the dose-dependent systematic error, the error in $D_{\text{mean, no pve}}$ was reduced from -22% to +2%; while the error in D_{80} was reduced from -36% to -15%. The overestimation in D_x for volume coverage x >50% was consistent with the systematic error introduced by the image noise (Chapter 4.3.3.1).

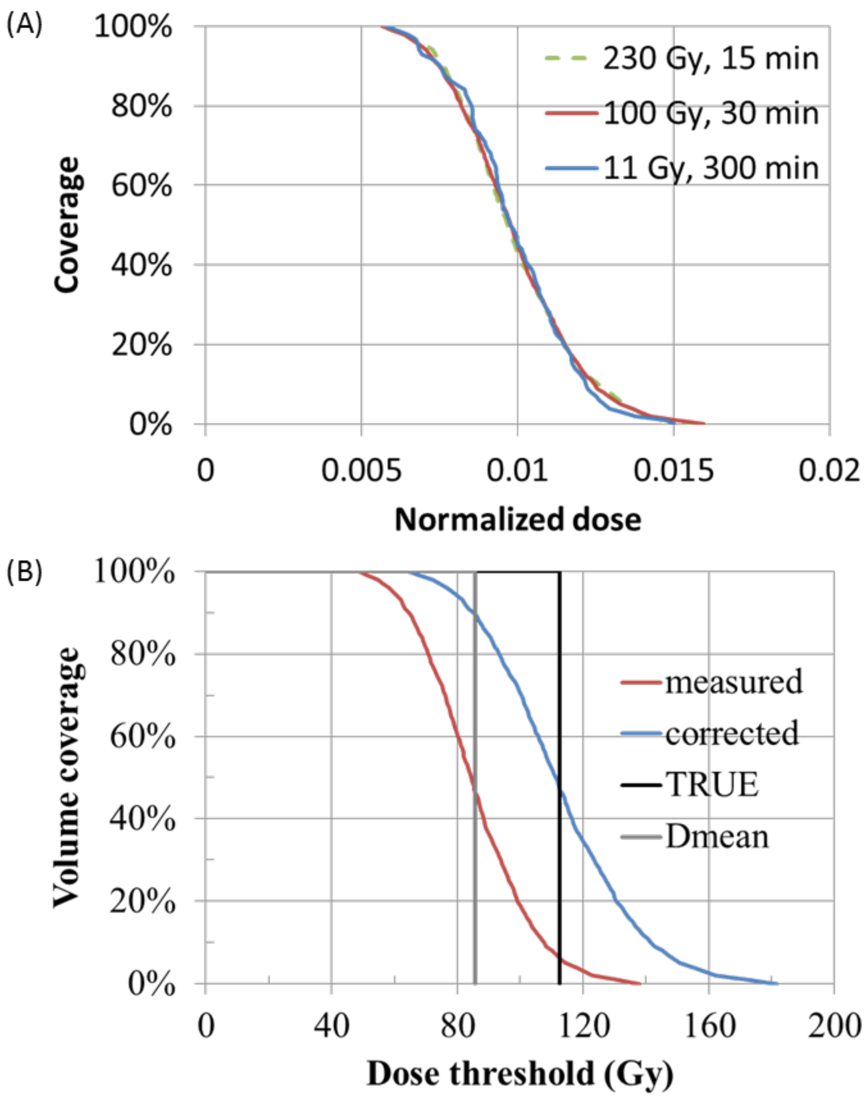

Fig 16. (A) Agreement between normalized dose volume histograms estimate (DVH') calculated from 37-mm spheres images (17-mm volume of interest) with comparable image noise, i.e., equivalent number of true coincidence (dose rate × acquisition duration). (B) DVH' before and after correction for dose-dependent systematic error.

4.3.2. Comparison between ^{90}Y and equivalent ^{18}F studies

Dose-dependent, which were seen in ^{90}Y study, were not observed in ^{18}F study with equivalent positron emission rates. Fig 17A shows errors in $D_{\text{mean, no pve}}$ as a function of positron emission rate (or equivalent ^{90}Y activity) for both ^{18}F and ^{90}Y studies. The errors in ^{18}F had higher uncertainty due to their single 30-min acquisition duration compared to 10 repeat scans of 30-min acquisition for each ^{90}Y data point. The correlation of the errors and positron emission rate in ^{18}F study was not clinically and statistically significant with slope of 0.0006 and *p-value* of 0.5. In contrast the errors in $D_{\text{mean, no pve}}$ and positron emission rate had strong correlation with slope of 0.07 and *p-value* of 0.007.

At clinical ^{90}Y equivalent positron emission rate, the random fraction (random events/total prompt) in both ^{90}Y and ^{18}F data were very high. Fig 17B shows that the random events dominated the total prompts in both ^{90}Y and ^{18}F studies. The number of random events in ^{90}Y data, however, was higher than it was in ^{18}F data with equivalent number of true coincidence.

Because of the very low PET signal (low positron emission rate), the random events associated annihilation photons are low as well. Fig 17B shows that the number of random events in ^{18}F data was dominated by LYSO background; as the positron emission rate (activity) increased from 2 to 75 kcps, the number of random events only increased from 1.50 to 1.53 Mcount. On the other hand, the major contributors to the number of random events in ^{90}Y data were LYSO background and bremsstrahlung photons. The number of random events increased from 2.34 to 4.95 Mcounts as the positron emission rate increased from 4 to 75 kcps (0.13 to 2.36 GBq ^{90}Y). The number of random events due to LYSO background was calculated to be 1.55 Mcount in 30-min blank scan, which was consistent with zero extrapolation from random events in ^{18}F study. In contrast, there seemed to be an overestimation in the LYSO background contribution in ^{90}Y data; zero extrapolation from random events in ^{90}Y was 2.13 Mcount.

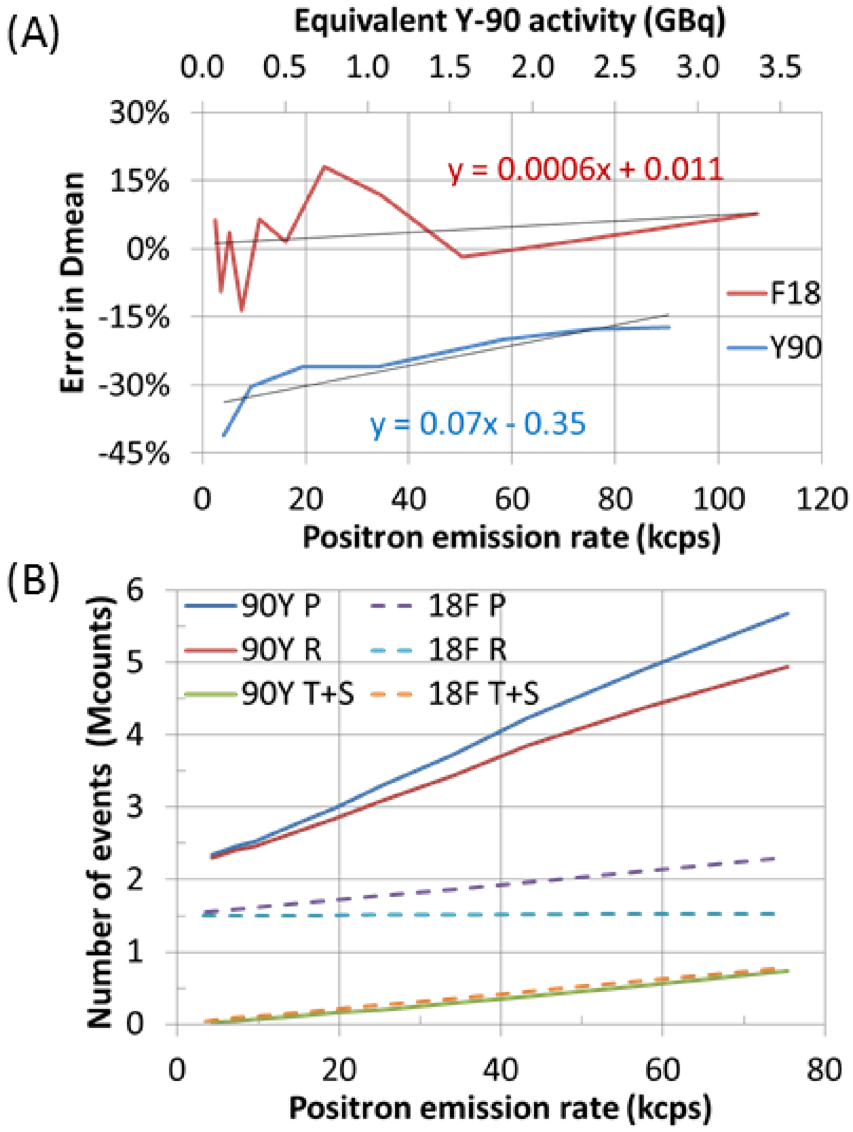

Fig 17 (A) Errors in mean dose of 37-mm sphere image (calculated using 17-mm volume of interest) as a function of positron emission rate (or equivalent ^{90}Y activity) for both ^{18}F and

^{90}Y in similar phantom studies. (B) Number of coincidence events in the scanner FOV as a function of positron emission rate from ^{18}F and ^{90}Y phantom studies in (A). Note: P: total prompt, R: random coincidence, T+S: true + scatter coincidence

4.3.3. Impact of low signal on volumetric ^{90}Y dose quantification

4.3.3.1. Impact of image noise on volumetric ^{90}Y dose quantification accuracy

We observed that the low count acquired in PET data increased the non-uniformity (image noise) in the dose distribution. Due to the non-negativity constraint of the voxel values in the image-reconstruction algorithm, the observed dose distribution was positively skewed, i.e. the dose distribution had a long tail toward high dose while the mass of the distribution was concentrated on the lower dose, as shown by the differential dose histogram in Fig 18A for 37-mm sphere (minimal PVE, reference dose of 60 Gy) under multiple acquisition durations. The degree of skewness, calculated as Pearsons' 2nd skewness coefficient, increased as the image noise increased (with shorter acquisition duration and/or lower dose). The D_{median} had increased negative deviation from D_{mean} as the acquisition duration was reduced, Fig 18B. Image noise introduced errors in the sphere DVH estimate as shown in Fig 18B for 37-mm sphere with known dose of 230 Gy. Away from the average dose (D_{mean}) the DVH metrics (D_x) toward the minimum dose (D_{100}) were underestimated and toward the maximum dose (D_0), D_x were overestimated.

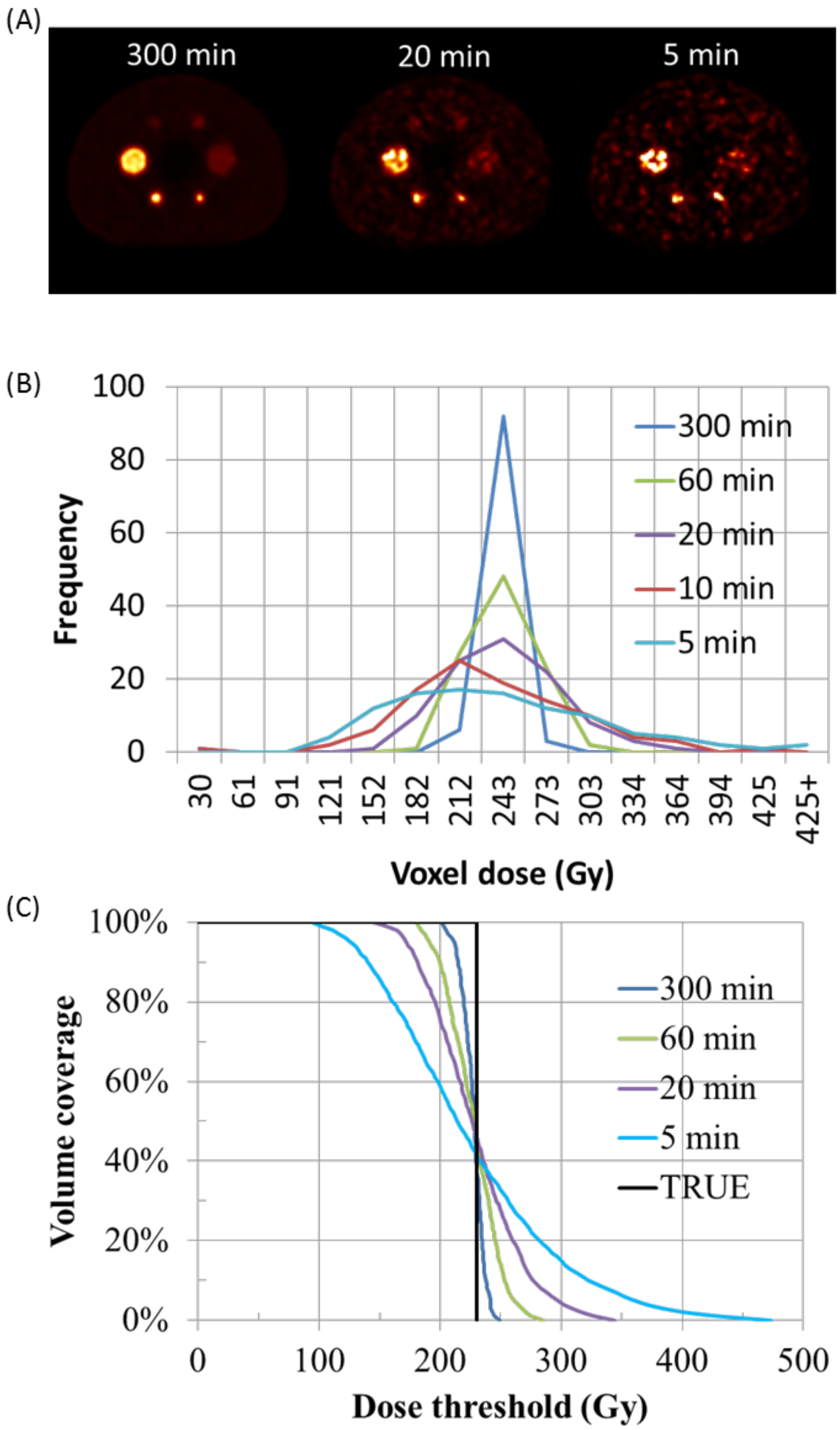
(A)
300 min
20 min
5 min
(B)
Frequency
100
80
60
40
20
0
30
61
91
121
152
182
212
243
273
303
334
364
394
425
425+
Voxel dose (Gy)
300 min
60 min
20 min
10 min
5 min
(C)
Volume coverage
100%
80%
60%
40%
20%
0%
0
100
200
300
400
500
Dose threshold (Gy)
300 min
60 min
20 min
5 min
TRUE

Fig 18. (A) Images of modified IEC phantom acquired for 300, 20, and 5 min. The sphere doses are 230 and 77 Gy with SBR of 13 and 4, respectively. (B) Differential and (C) cumulative volume histogram in 37-mm sphere image acquired for multiple acquisition duration. The histograms were calculated using 17-mm volume of interest to minimize partial volume effect.

Fig 19 shows the DVH' of the 17-mm sphere with PVE, and DVH' of the 37-mm sphere with and without PVE. The sphere dose was 230 Gy and the images were acquired for 300 min (solid lines) and 10 min (dash lines). With minimal PVE, the magntidue of errors in D_{80} increased from -3.4% to -22.7% when the acquisition duration was reduced from 300 to 10 min. The errors in $D_{\mathrm{mean,\ no\ PVE}}$ were relatively insensitive to noise, the errors increased from -0.2% to -2.5% as the duration was reduced.

PVE caused underestimation in DVH' at all volume coverage (Fig 19). The errors in D_x were higher toward minimum dose, i.e., when the volume coverage (x) was high. The errors in 37-mm sphere DVH' calculated from 300-min sphere images were -29.7%, -12.5% at D_{80}, and D_{mean}, respectively; whereas the errors in 17-mm sphere (300 min) DVH' were --55.4%, -32.4% at D_{80}, and D_{mean}, respectively. The confounding errors from image noise were minimal in the DVHs calculated from 300-min images: < 5% between D_5 and D_{95}, and < 10% outside D_5–D_{95}. In the presence of PVE, the additional errors due to acquisition reduction from 300 to 10 min were ∼10% and <5% for both 37- and 17-mm sphere. These additional errors were slightly lower (1%–2%) in 17-mm sphere, which suffered more PVE, than they were in 37-mm sphere DVH.

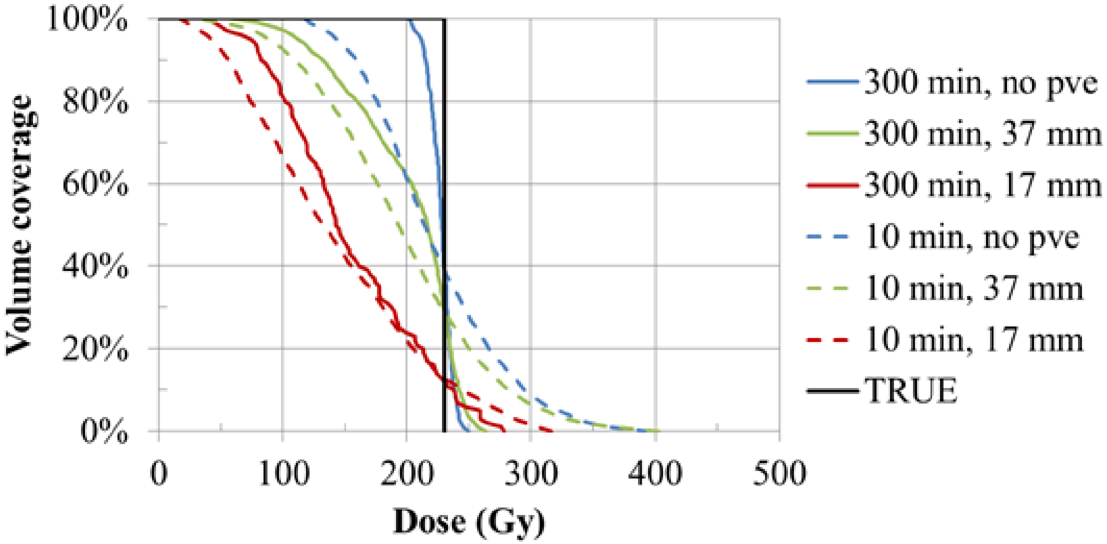

Fig 19. Dose volume histogram (DVH) of spheres with 3 degrees of partial volume effect (minimum, 17- and 37-mm sphere) and 2 acquisition durations (300 and 10 min).

Fig 20 shows the errors in 17-mm sphere DVH' (D_{20}, D_{mean}, and D_{80}) as a function of known sphere dose for both 30-min (solid lines) and 10-min (dash lines) acquisition duration. For acquisition duration of 30 and 10 min, the errors in DVH estimates (D_{20}—D_{80}) between known dose of 60—240 Gy were not sensitive (< 10% change) to changes in dose. At known sphere dose of < 60 Gy, the magnitude of errors started to increase.

The average errors in DVH' for 17-mm sphere with known dose of 60—240 Gy were -8%, -33%, and -57% at D_{20}, D_{mean}, and D_{80}, respectively, for 30-min scan; while, the errors in DVH' calculated from 37-mm sphere images (30-min scan) were +12%, -10%, and -34%, respectively. At shorter acquisition duration of 10 min, the additional errors in the DVH estimates for 17-mm sphere images were -10% and -1% at D_{80} and D_{20}, respectively.

For DVH estimates of 37-mm sphere images, the additional errors were +5% and +11% at D_{80} and D_{20}, respectively.

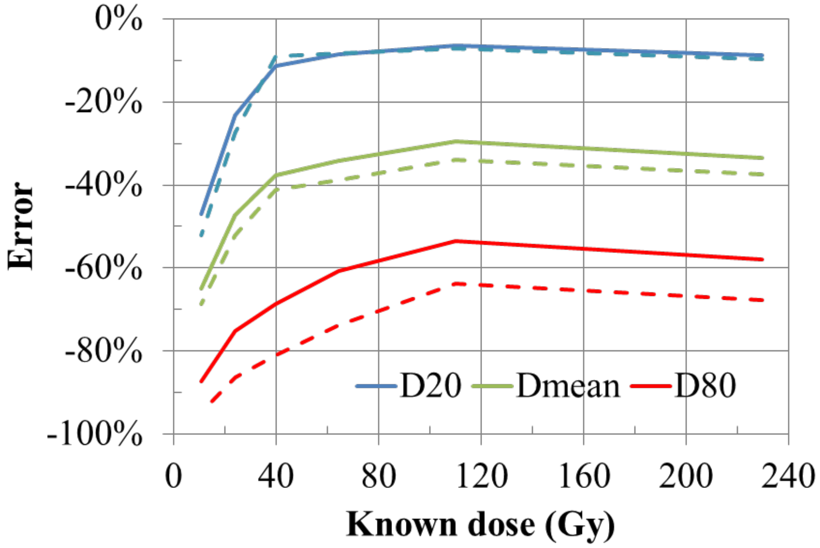

Fig 20. Errors in D_{80}, D_{20}, and D_{mean} as a function of known dose for 17-mm sphere. The solid and dash lines indicate errors in 30- and 10-min acquisition, respectively.

4.3.3.2. Impact of low count on volumetric ^{90}Y dose quantification random error

The COV of DVH estimates was lower in 37-mm sphere and 30-min duration. Fig 21A shows COV of DVH estimates as function of volume coverage for sphere sizes of 37- (solid lines) and 17-mm (dash-dot lines) spheres, and acquisition duration of 30 and 10 min. We found that the COV was the highest around the minimum dose (D_{80} to D_{100}) followed by the maximum dose (D_0 to D_{20}); whereas between D_{20} to D_{80} the COV was the lowest and stable (< 10% change).

In clinically relevant tumor dose of 60—230 Gy, the COV (between D_{20} to D_{80}) of 37-mm sphere DVH estimates was < 5% and < 10% for acquisition duration of 30 and 10 min. For 17-mm sphere DVH estimates, the COV (between D_{20} to D_{80}) was < 15% for acquisition duration of 30 min. DVH estimates of the 17-mm sphere that were calculated from 10-min sphere images suffered from higher random error. At a known sphere dose of 110 Gy, the COV (between D_{20} to D_{80}) of DVH estimates was already 20%. Fig 21B shows the maximum COV (between D_{20} to D_{80}) as a function of known dose.

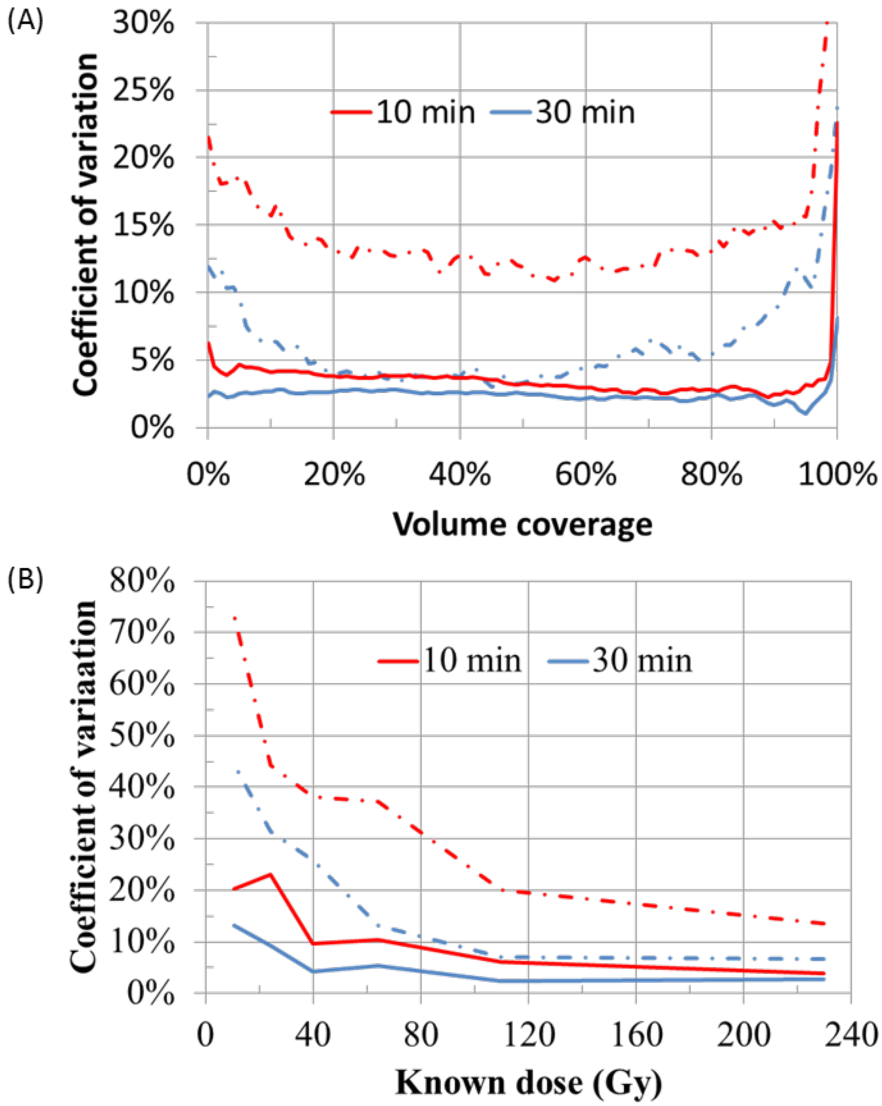

Fig 21. (A) Coefficient of variation (COV) in 37- and 17-mm sphere DVH estimates (with known dose of 230 Gy) calculated from 30- and 10-min images with 10 noise realizations. (B) Maximum COV (between D_{20} and D_{80}) in 37- and 17-mm sphere DVH estimates as a function of known dose. Note: the solid and dash-dot lines represent 37- and 17-mm spheres, respectively.

4.4. Discussion

4.4.1. Dose-dependent errors in volumetric ^{90}Y dose quantification

We characterized the errors in $D_{mean,\ no\ pve}$ as a function of known dose and compared them to the errors in $D_{mean,\ no\ pve}$ as a function of duration (Section C.2.1). The correlation between errors in $D_{mean,\ no\ pve}$ and acquisition duration (fractional count) was found to be practically (< 1% change in errors going from 300- to 5-min duration) and statistically (p value of the slope >> 0.05) insignificant; hence suggesting that the errors trend observed from images with decayed dose level was related to the dose (activity) only and not related to image noise.

True, scatter, and random contribute to the total prompt acquired. Among these components, random is the only quadratic component. In this work, the random correction was done using estimation from singles, i.e., $R \cong S_1 S_2 \Delta T$, where R is the random rate, S_1 and S_2 are the single rates, and ΔT is the timing resolution. The quadratic relationship (Fig 15A and Fig 15B) between measured $D_{mean,\ no\ pve}$ suggests that the random was not properly corrected which resulted in an dose-dependent errors in $D_{mean,no\ pve}$. This hypothesis is also supported by comparison with ^{18}F study with comparable positron emission rate to ^{90}Y. In our ^{18}F phantom study, when positron emission rate is < 20 kcps, the random fraction (random event/total prompt) is >90% (Fig 17B), which is comparable to the random fraction observed in clinical ^{90}Y study. However, even with similar random fraction, no dose-dependent systematic errors were observed in ^{18}F study. Comparison to trace amount of ^{18}F study suggests that the dose-dependent systematic errors observed in ^{90}Y is caused predominantly by the imperfect correction of random events from bremsstrahlung photons—

which is absent in ^{18}F study—rather than from background radiation in the detector from LYSO crystal, as suggested by previous study (66).

The overall errors in sphere DVH’ that we showed in section C.3.1. were corrected for the activity-dependent errors. In clinical practice, it may not be possible to correct for these dose-dependent systematic errors (section C.2.1.) because of the confounding errors in measured mean dose. Without correction for dose-dependent systematic error, the additional systematic error in volumetric dosimetry for tumor with average dose of 40–230 Gy is -20% to -30% (Fig 15B), whereas the systematic error in dose quantification in the normal tissue (< 30 Gy) is ~5–10 Gy.

4.4.2. Systematic and random errors in quantitative ^{90}Y -PET imaging in clinical practice

The unique challenge in ^{90}Y PET imaging is that it has a very low signal (32 ppm positron yield), which introduced systematic errors (Fig 18) and random error (Fig 21), both of which result in errors in DVH’ (Chapter 4.3.3). Systematic errors in DVH’ due to increased image noise can be reduced by “minimizing” equivalent iteration and “maximizing” filtration FWHM (section C.1.2.). Through image reconstruction optimization, the additional systematic error in DVH’ due to image noise can be kept < 10% (in addition to > 50% total systematic error) even at low tumor dose of 40 Gy and image acquisition duration of 10 min (Fig 19 and Fig 20).

The random error in DVH’ measurement can only be reduced by increasing the signal acquired. For a given PET imaging system, the only adjustable parameter is the acquisition duration (or table speed in continuous bed motion mode. For GE D690/D710, at acquisition duration of 30 min, the random error in measured DVH' can be kept < 10% even in 17-mm sphere with low dose (40 Gy); while at acquisition duration of 10 min, the random error in DVH' is > 20%. Therefore, to keep the additional errors (systematic and random) in DVH' < 20% for a typical tumor in hepatocellular carcinoma (HCC)—equivalent sphere diameter of > 17 mm and mean tumor dose > 60 Gy—ideally ^{90}Y PET data need to be acquired for 30 min. In clinical practice, the prescribed scan length for ^{90}Y-microsphere liver scan is 2 bed positions for majority of the patients; hence scan duration needed would be 2 × 30 min, which will likely be the maximum duration in clinical practice.

At lower count study, e.g. shorter duration and/or lower activity concentration, the COV is higher toward minimum dose D_{100}. The COV differences of D_{20} and D_{80} of up to 10% were observed. For decent statistic (duration of 300 min, dose of 230 Gy), Dmean approximately equals to D_{50}, however, Dmean is closer to D30 at low statistic (duration of 10 min, dose of 230 Gy). Consequently, the COV in Dmean at low statistic can be up to 10% lower than D_{80}. The errors in DVH also increase with increase in image noise, a manifestation of low count data. The magnitudes of errors in DVH are the smallest at D_{mean}, whose location in the DVH varies between D_{20}–D_{50} depending on the image noise, and the highest toward D_0 and D_{100}. In addition, because of the magnitude of the errors in D_{80} are higher, the random errors are also higher. Therefore for summary metrics such as D_{80} or D_{70} will have higher systematic errors and random errors than D_{mean}.

Without activity-dependent correction, the measured D_{mean} in tumor (> 27 mL) PET images acquired (using GE TOF scanners (D690 and 710, without prompt gamma correction) will have errors of -20%, -25%, and -30% at measured mean dose of 200, 100, and 50 Gy.

For tumor with smaller size (e.g. 2.6 mL), the errors are about 10% higher due to partial volume effect. The uncertainty is < 5% for tumor D_{mean} of dose > 50 Gy (both 30- and 10-min durations).

The underestimation in D_{mean} is increasing from -30% to -35% when Dmean decreases from 50 to 10 Gy (dose level relevant to normal tissue). The uncertainty in Dmean of normal tissue is low (<5%) as well for both acquisition durations of 10 and 30 min because the volume of interest for normal tissue is usually large (>> 27 mL).

Another consideration for determining the acquisition duration is whether or not to perform (gating-based) motion correction for liver, which is subject to breathing motion. With quiescent-period-gating method, the systematic errors in DVH' in motion-degraded images can potentially be reduced to < 10% —which is consistent with our finding here where the additional systematic error in DVH' due to reduced duration is <10%—at the expense of increase random error because the images were reconstructed using 33% of the total counts (effectively reducing the duration by 1/3).

Caution needs to be exercised when comparing dose data from published reports. Major challenges in comparing dose (Gy) are dosimetry models (standard vs partition vs image based), input images (PET vs ^{90}Y microsphere bremsstrahlung SPECT vs ^{99m}Tc-MAA SPECT). In our study using GE TOF scanners, we learned that even with the same PET-based dosimetry, the discrepancies in quantification of PET image from different scanner models (and image reconstruction) makes it difficult to make direct dose comparison. The errors in Dmean that we reported in GE TOF scanners are different from the errors observed in Siemens or Philips scanners.

Going forward, dose reporting needs to include the estimated errors (both systematic and random) in order to be able to make “Gray” a meaningful unit again. Unless these errors are reported, we cannot compare the dose value reported in other publications.

The QUEST study by Willowson et al (66) characterized the average systematic errors in various make and model of PET scanners. This study can be used to translate PET-based dose value.

4.4.3. Partial volume effect

Partial volume effect (PVE) blur the sphere images, as a result the image (activity concentration [Bq/mL] distribution) of a uniform sphere is not uniform with the measured activity concentration higher at the center than at the edge of the sphere image. The PVE is more severe in sphere with smaller diameter. Due to PVE, the sphere DVH deviates from the ideal rectangular DVH.

Dose map of a sphere with uniform 90Y activity distribution is not uniform because the electrons deposit their energy as they stagger in the sphere with average range of 4 mm and max range of 11 mm. The point at the center of the sphere will have highest dose because it receives the energy from all the high activity concentration distributed in the radius of 11 mm. A point at the edge of the sphere will have lower dose because it receive energy partially from high activity distribution in the sphere and also from low activity distribution in the background. As a result the dose map is a blurred version of the ideal uniform sphere image.

Using local deposition method (LDM), the sphere PET image (Bq/cc) is proportional to the dose map (Gy), i.e., the relative distributions are the same. Both sphere

PET images and sphere true dose map are a blurred version of the ideal uniform sphere image; hence the effect of image PVE on dose map calculated using LDM is reduced. The errors of PET-based dose map (LDM) with respect to the true dose map will be higher if the PET resolution is much different to the FWHM of the dose-kernel, e.g. resolution in the order of centimeter or sub-millimeter.

4.4.4. Study limitation

This study was limited to phantom studies using a modified NEMA IEC phantom. Spheres with uniform dose were not true representations of heterogeneous ^{90}Y-microsphere distribution in the tumor. Future studies using a physical phantom (83) with inhomogeneous ^{90}Y distribution are needed to further evaluate the errors in volumetric ^{90}Y dosimetry calculated from ^{90}Y PET images.

PVE is the dominant source of systematic errors in DVH' even in count-limited ^{90}Y PET images (Chapter 4.3.3). In this work, we did not perform partial volume correction beyond using PSF correction option in the image reconstruction. Even though application of post-reconstruction filtration increases PVE, we have shown in section C.1.2 that application of moderate filtration (5.2-mm FWHM, in this case) results in less systematic errors in DVH'. Voxel size and z-axis filtration were not evaluated in this work. Both parameters can potentially be optimized to trade-off the systematic error and random error in DVH'.

Partial volume effects are often compensated (74, 86) using a correction factor , which is derived from either simulation or phantom studies, to correct for average voxel value in a VOI for a given geometry. This empirical partial volume compensation method can be expanded to correct for underestimation in DVH' instead of the mean dose alone.

More advance partial volume correction methods use prior anatomical information based on co-registered high resolution CT images. Application of this class of partial volume correction to ^{90}Y quantitative PET imaging is very challenging because there is no biological uptake of microsphere distribution; microspheres are distributed mechanistically based on the blood flow in the vasculature, which may not be resolvable in CT images.

We hypothesized that the dose-dependent systematic error originated from imperfection in random correction of bremsstrahlung photons. Recently, ^{90}Y-PET image reconstruction algorithms that model the prompt gamma have become clinically available. Similar phantom studies are needed to determine whether prompt-gamma modelling can reduce the dose-dependent systematic error in ^{90}Y PET images.

4.5. Conclusion

Low signal in ^{90}Y PET imaging introduces both systematic and random errors in volumetric ^{90}Y dose quantification. Using errors in DVH' as the objective function, the image reconstruction protocol can be optimized such the additional systematic error in DVH' due to low signal < 10%. To keep the random error low, ^{90}Y PET data need to be acquired for as long as reasonably achievable (anti ALARA) duration, especially if motion correction is to be implemented.

Chapter 5: Effects of image noise, respiratory motion, and motion compensation on 3D activity quantification in count-limited PET images

5.1. Introduction

^{90}Y microspheres are used for treating non-resectable primary and metastatic liver cancers (48, 49). Post-treatment ^{90}Y imaging is useful in assessing planned microsphere delivery and treatment efficacy (21, 81, 83, 87, 88). Unlike most radionuclides used in nuclear medicine imaging, ^{90}Y is effectively a pure beta emitter, i.e., it lacks discrete-energy photon emissions, such as gamma and/or characteristic fluorescence X-rays. As a result, imaging ^{90}Y directly is challenging. The distribution of ^{90}Y activity is traditionally assessed by imaging the bremsstrahlung photons—produced from interactions of energetic beta particles with soft tissue—using a gamma camera or single-photon emission computed tomography (SPECT)/computed tomography (CT). The ^{90}Y decay process has a very small branching to the excited state of stable ^{90}Zr, which is followed by an internal pair production ($\sim 3.2 \times 10^{-5}$ per β-decay) (50). The positrons generate a pair of 511-keV annihilation photons that can be imaged using PET/CT. Several recent studies have suggested that ^{90}Y positron emission tomography (PET)/CT imaging is superior in image resolution, image contrast, and quantitative accuracy compared to ^{90}Y bremsstrahlung SPECT/CT (24–26).

Because liver is subject to respiratory motion, in vivo imaging of the liver is degraded by motion blur artifact. Typically acquisition duration of 15–30 min/bed is used to compensate the extremely low ^{90}Y-PET signal. During the long PET acquisition, respiratory motion causes motion blur attributable to the time-averaging of multiple breathing cycles (a normal breathing cycle is typically 4 seconds). Extensive studies of the impact of respiratory motion in fludeoxyglucose (^{18}F) (^{18}FDG) PET have demonstrated that motion artifacts cause blurring of the target volume margins and underestimation of PET standardized uptake values (SUV) (41–44).

Respiratory-gated PET/CT acquisitions group the acquired data into smaller phase or amplitude-matched bins to reduce motion blur, but at the cost of increasing noise, owing to the lower counts in each bin (46). To simultaneously avoid this increase in noise and the potential for data misregistration (between the PET and CT images) that results from spatiotemporal mismatch (43, 89, 90), PET emission data can be acquired in a quiescent respiratory phase, such as end expiration, in which the motion is relatively low. Quiescent-period gating (QPG) was developed to allow free breathing acquisition while reducing the motion artifact (45). In high-count studies like ^{18}FDG PET/CT imaging, it is clinically feasible to increase the acquisition duration (by a factor of 3 to 5 or, equivalently, by 10–15 min) to compensate for the noise penalty from gating. However, in a ^{90}Y-PET/CT acquisition, in which the number of positron emissions is 0.033% of that of an equivalent ^{18}FDG scan, increasing the acquisition duration (for example, to 60–100 min/bed) to compensate for the noise penalty caused by respiratory binning is not practical.

Previous work on PET motion compensation in ^{18}FDG scans has compensated for underestimation in SUV_{max} or SUV_{mean}; however, in these studies, the main imaging task was tumor detection, not measurement of the 3-dimensional (3D) activity or dose distribution. Post-^{90}Y-microsphere therapy quantitative PET/CT imaging has been extensively researched over the past several years, but studies still focus on the mean activity concentration (AC), which is more relevant to diagnostic imaging than to post-therapy imaging (24, 66, 67, 91). Post-^{90}Y-microsphere therapy PET/CT imaging provides the unique opportunity to make voxel-level absorbed dose calculations that can subsequently be used to predict tumor control probability and toxicity to normal tissue, which will enable the development of more personalized and more effective treatment strategies.

Drawing from radiation oncology, 3D voxel-level dosimetry calculation is often characterized by the cumulative dose volume histogram (DVH) (76, 77, 92, 93). It has been suggested that the dose distribution in ^{90}Y-microsphere therapy can readily be calculated from the ^{90}Y activity distribution images by assuming local energy deposition of the electrons (35, 51). Voxel-based dosimetry methods for ^{90}Y-microsphere therapy have been developed recently (20, 34, 51, 94). Those methods calculate the dose distributions from the 3D AC distribution either from surrogate ^{99m}Tc-MAA SPECT/CT images or from 3D ^{90}Y images (bremsstrahlung SPECT/CT or PET/CT) as the input functions. One limitation of voxel-based dosimetry is the accuracy of the inputs, which are subject to image-degrading factors such as image noise and motion blur (40).

The local deposition method assumes proportionality between absorbed dose to the voxel (in Gy) and activity concentration (in Bq/mL), which is the unit of voxels in PET images; therefore we propose to present DVHs as activity concentration volume histograms (ACVHs). The ACHV plots the threshold AC (abscissa) against the fraction of the volume of interest (VOI) with AC greater than or equal to the threshold (ordinate). ACVH also provides information about the conventional summary metrics, such as minimum, maximum, and median AC. The ordinate of ACVH spans 0% to 100% and the width of the ACVH curve around the median (50%) serves as an indicator of the non-uniformity of the 3D AC in the VOI; greater spread indicates a higher degree of non-uniformity. We characterized the effects of image noise and motion blur on ACVH estimates in count-limited phantom studies mimicking ^{90}Y PET/CT images. We also investigated whether the motion errors in the ACVH under very low-count conditions can be effectively compensated for using QPG.

5.2. Methods

5.2.1. Data acquisition

All PET/CT images were acquired using a GE Discovery 690 (General Electric Medical Systems, Milwaukee, WI). We assessed image quality and quantification using the National Electrical Manufacturers Association (NEMA) International Electrotechnical Commission (IEC) body phantom (Data Spectrum Corp., Chapel Hill, NC). A small amount of 18F was injected into the IEC phantom as a surrogate radionuclide to simulate the inherent low count typical of 90Y PET/CT studies. We matched the total number of positrons emitted in a 18F scan for 47 s/bed acquisition to those in a 90Y scan for 30 min/bed by equalizing the activity × positron yield × acquisition duration. The typical 90Y scan emulated was for a mean liver dose of 30 Gy with tumor uptake ratio of 10 (22, 24). The IEC phantom was prepared with 18F AC in the background of 0.8 kBq/mL (equivalent to 600 kBq/mL for 90Y) and a sphere-to-background ratio (SBR) of 9.6.

The PET data were acquired using a 1-bed position, centered at the spheres. We only acquired CT images of a static phantom to calculate the attenuation correction. We did not expect any significant motion errors in the attenuation map because both the spheres and background contain water, and the thin acrylic walls of the spheres have attenuation similar to that of water, at 511 keV.

All images were reconstructed using 3D Ordered Subset Expectation Maximization (OSEM) iterative reconstruction with time-of-flight correction and point spread function modeling (GE Vue Point FX-S) using the following parameters: 2 iterations and 24 subsets, 50-cm field of view, 5.2-mm post-reconstruction axial filter, and standard z-axis filter.

5.2.1.1. Effects of total count on 3D activity quantification

To establish a high-count reference dataset, we acquired PET data of the 18F IEC phantom for 300 s (equivalent to a 3 hour/bed 90Y scan). These data were down-sampled to shorter durations per bed position: 47 s (equivalent to clinical 90Y total counts, i.e., 100%), 40 s (85%), 32 s (68%), 24 s (51%), 16 s (33%), and 8 s (17%). Data down-sampling for each duration was done on 5 independent time windows to determine statistical variations in the activity distribution quantification.

5.2.1.2. Effects of motion on 3D activity quantification

To evaluate the effects of motion on activity quantification, we acquired 4 PET datasets with the IEC phantom: a single static reference acquisition and 3 motion-degraded PET data with periodic motions of 1-, 2-, and 4-cm amplitudes. The phantom motion was tracked using a real-time position management device (RPM, Varian Medical System, Inc., Palo Alto, CA) (95). We used an in-house motion platform (96) that uses a linear stage (Velmex, Inc., Bloomfield, NY) to simulate regular 1D respiratory patterns, with a typical period of 4 s and amplitudes of 1, 2, and 4 cm (Fig 22). To reduce the compounding effect of image noise (section B.1.1), all PET data sets with motion were acquired for 300 s. These 300-s data sets had lower noise (background standard deviation [SD] of 15%) than do clinical ^{90}Y PET images (background SD of 40%).

5.2.1.3. Effectiveness of QPG as compensation for 3D AC distribution in a count-limited study

We evaluated the ability of the QPG to effectively trade off motion blur and image noise in a count-limited PET study by improving the image contrast-to-noise ratio (CNR) and AC quantification. The 4 datasets acquired in section B.1.2 were down-sampled to 47 s to yield the total number of counts expected in a clinical 90Y PET scan. The 3 motion-degraded datasets were retrospectively binned into 3, 4, and 5 respiratory-phase gates over the 4-s motion period; the PET images were then reconstructed for each gate to create 4D PET images.

The motion artifacts in the images were compensated using 2 QPG, with count (time) fractions of 25% and 33%, i.e., a single respiratory gate was used for image reconstruction from 4D PET that was gated with 4 and 3 respiratory bins, respectively. We also co-registered adjacent gated images (post-reconstruction) during the quiescent period to create QPG images with count fractions of 40% and 50%, i.e., to co-register 2 gated images in 4D PET with 5 and 4 bins (Fig 22), respectively.

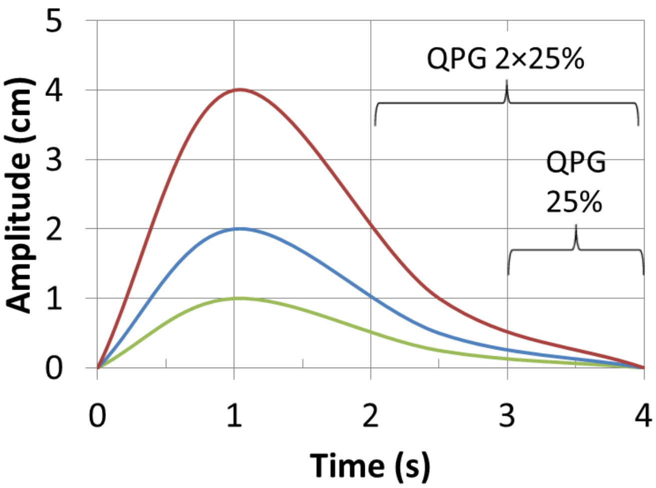

Fig 22. The ilustration of the gating timing of quiescent period gating (QPG) motion compensation on 1-D motion input function with period of 4 s and amplitude of 1, 2, and 4 cm. QPG images with a count fraction of 25% were created by selecting 1 gated image in the quiescent period from a 4D PET image with 4 gates. QPG images with a count fraction of 2 × 25% were created by co-registering 2 adjacent gated images in the quiescent period from 4D PET with 4 gates.

5.2.2. Data analysis

The hot spheres, which represented tumors, were segmented out using sphere VOIs contoured from the corresponding CT images (Fig 23). The diameters of the VOIs were matched to the sphere diameters (from the NEMA IEC phantom manual) and were verified from the CT images of the sphere inserts. For static PET images, all VOI locations were registered to the CT images of the spheres. For PET images with motion blur, the VOI locations in the bed axis (along the motion direction) were manually adjusted by registering the VOIs and the sphere location in the PET images; the centers of all VOIs were still co-planar.

The normal liver tissue surrounding the tumor was represented by a 126-mL cylinder containing a 1.7-cm sphere (Fig 23). The spherical VOI (diameter of 1.7 cm) was segmented out from the cylindrical VOI to simulate uniform ^{90}Y activity in normal tissue around the tumor.

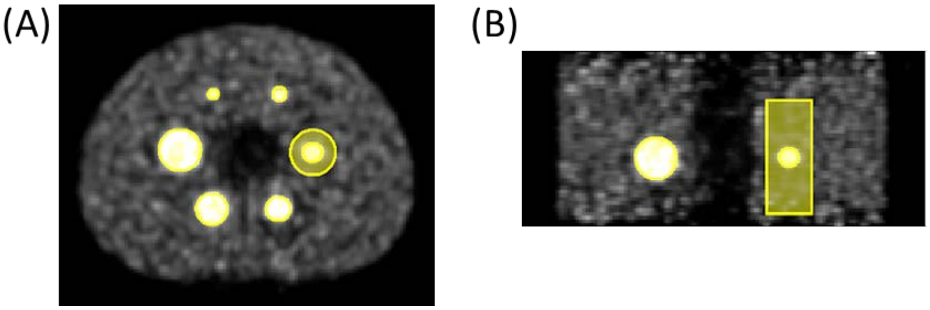

Fig 23**.** Size and placement of the volumes of interest (VOIs) from which activity concentration distributions were quantified. The spherical and cylindrical VOIs represent, respectively, tumors and normal tissue surrounding the 17-mm “tumor” in transaxial (A) and coronal (B) views.

To quantify the AC distribution, we calculated the cumulative ACVH for all VOIs (6 spheres and 1 background) for the 4 PET image acquisitions. In addition, we calculated the ACVHs for each down-sampling and gating method.

5.2.2.1. Effects of total count on 3D activity quantification

The ACVHs of both the sphere and the background were calculated for all static PET images with durations of 300 s (reference images), 47 s, 40 s, 32 s, 24 s, 16 s, and 8 s.

The ACVHs for 47, 40, and 32 s images were calculated as the average ACVH from 5 down-sampled scans; whereas the ACVH for 24, 16, and 8 s were calculated as the average of 10 down-sample scans. The variability of the ACVH was measured as the standard deviation of multiple down-sampled scans of the same total duration. The ACVH for each down-sampled image was compared graphically against those for the reference images. The ACVHs were compared quantitatively by computing the deviation of the AC of the PET images from that of the reference image as a function of cumulative volume.

For the spheres, we also reported the difference in mean AC (AC_{mean}) and differences in AC_X (defined as the minimum AC that covers X% of the VOI) that are typically used in tumor dosimetry; for example, AC_{90}, AC_{80}, and AC_{50} as a function of total count (or duration). The relationship between the ACVH parameters AC_{90}, AC_{80}, AC_{50}, and AC_{mean} and the count densities was evaluated using linear regression analysis; the slopes and the corresponding *p* value were reported.

5.2.2.2. Effects of motion on 3D activity quantification

We visually analyzed the effects of motion in the sphere images by comparing the motion-degraded images with the static reference images. We also compared line profiles of the sphere images along the motion direction as a semi-quantitative analysis of the motion blur.

The ACVHs of both the sphere and background were calculated for all high-count static (reference) images and high-count motion-degraded PET images. The ACVH for the motion-degraded images was compared graphically against the ACVH for the static reference images. The ACVH values were also compared quantitatively by computing the errors in AC of the motion-degraded images with respect to the reference static image as a function of cumulative volume.

In addition, for sphere images, we used linear regression analysis to evaluate the relationship between the errors in AC_{mean} and the relative motion (motion amplitude/sphere diameter) for 5 sphere diameters (37, 28, 22, 17, and 13 mm).[1] The Pearson correlation coefficient and the *p* value were reported.

5.2.2.3. Effectiveness of QPG to compensate for motion errors in 3D AC distribution in count-limited PET images

We evaluated the effectiveness of motion compensation using QPG with count fractions of 25% and 33% by quantifying the relative change (with respect to the static reference images) in image CNR and AC with and without QPG.

The effectiveness of motion compensation in the sphere images was visually analyzed by comparing the in-motion images with and without motion compensation to the static reference images. The CNR of the spheres was also calculated, as (sphere AC_{mean} – background AC_{mean}) / (background SD of mean), to evaluate the improvement in the image contrast.

The ACVHs of both the sphere and the background were calculated for static reference images and in-motion PET images with and without motion compensation. The ACVH of the in-motion images was compared graphically against the ACVH of the static

---

[1] The 10-mm sphere in IEC phantom was not detectable due to the very high noise, so the 13-mm sphere was the detection limit.

reference images. We also quantitatively compared the ACVHs by computing the errors in AC of the in-motion images before and after motion compensation. All errors were reported as differences from the static reference images.

For the reconstructed sphere images, we used linear regression analysis to evaluate the relationship between AC_{mean} and relative motion before and after motion compensation for 5 sphere diameters at 3 different motion amplitudes. The significance of the differences in the slopes of the linear regression curves before and after motion compensation were evaluated using a 1-sided *t*-test.

5.3. Results

5.3.1 Effects of total count on 3D activity quantification

Reducing the acquisition duration resulted in an increase in the image noise, as shown in Fig 24A. The range of observed AC increased with lower acquisition duration, i.e., the measured minimum AC decreased while the maximum AC increased (Fig 24B and Fig 24C). The increase in the non-uniformity of the AC distribution was more pronounced in the smaller spheres, i.e., the change in the ACVH spread was greater for the 17-mm sphere than for the 37-mm sphere. Because of the lower AC in the background (SBR of 9.6), the increase in AC distribution inhomogeneity was higher in the background region, as shown in the images in Fig 24A and the ACVHs in Fig 24C. The observed profiles were substantially different that the ideal ACVH, in part, due to the partial volume effect; the differences from ideal were less pronounced in the background compared to the tumor VOI (Figures 3B and 3C).

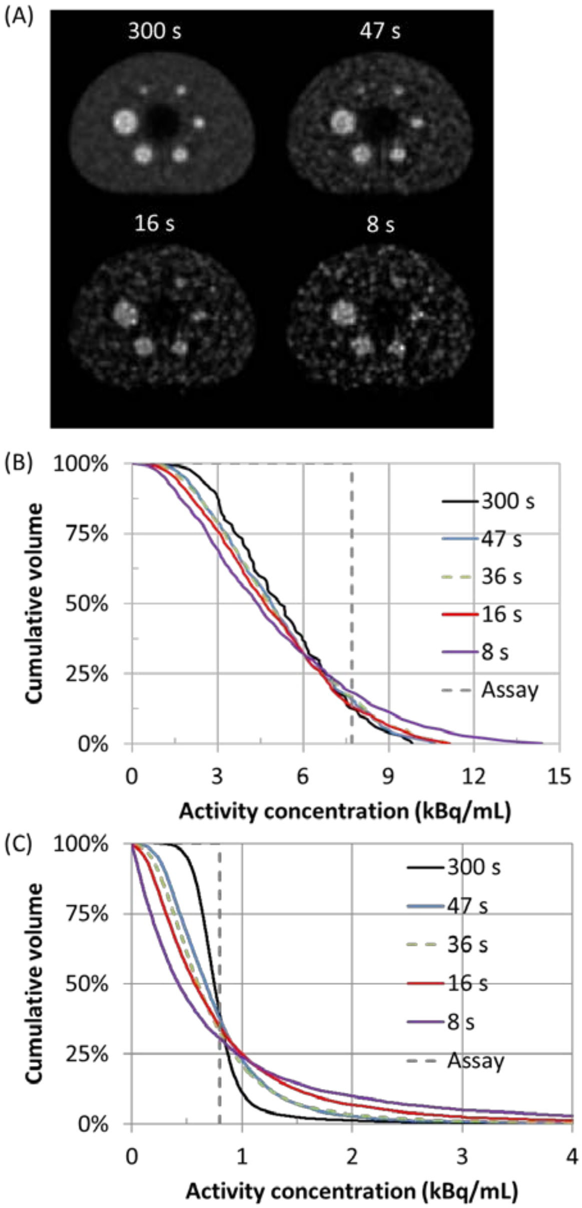

Fig 24**.** (A) Transaxial PET images of an IEC phantom acquired for the indicated durations. The window width and level of these images were adjusted manually to show the texture of the sphere images. (B, C) Activity concentration volume histograms (ACVH) for (B) the 17-mm sphere and (C) the surrounding background region as the acquisition duration varied. Note: the gray dashed ACVHs show ideal ACVH calculated from known activity assays. The ACVHs in (B) and (C) were average ACVH from multiple down-sampled scans.

AC$_{20}$ to AC$_{40}$ was observed to be less sensitive to duration reduction (< 10% deviation from the low-noise reference), as shown in Fig 25A. At an acquisition duration of 32 s (68%), the ACVH errors were comparable to the errors (< 5% difference) at the 47-s acquisition (100%), except beyond AC$_{90}$. At acquisition duration of 8 s (17%), the errors were > 10% outside the AC$_{20}$ to AC$_{40}$. Fig 25B shows the ACVH errors as a function of acquisition durations for several AC$_{X}$ that are typically used in tumor dosimetry. The errors and variability of AC$_{mean}$ were independent of a reduction in acquisition duration down to 17%. The slope of AC$_{mean}$ versus the acquisition duration was statistically consistent with zero; while the slopes for other AC$_{X}$ were non-zero and statistically significant ($p < 0.05$). The magnitude of both AC$_{X}$ errors and AC$_{X}$ variability monotonically increased away from AC$_{mean}$ (at around AC$_{30}$) toward both extremes, i.e., AC$_{0}$ (AC$_{max}$) and AC$_{100}$ (AC$_{min}$). The variability of AC$_{X}$ was also affected by the object and VOI sizes; the SD for the 37-mm sphere was smaller than it was for the 17-mm sphere. Similar trends were observed for ACVH parameters in the background VOIs.

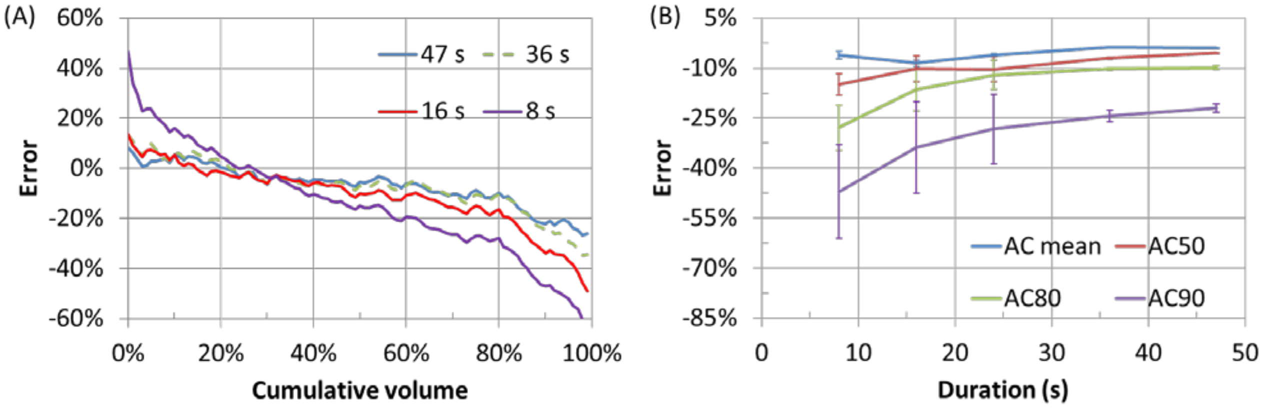

Fig 25**.** (A) Errors in the 17-mm sphere activity concentration volume histogram (ACVH) with respect to the ACVH calculated from reference images for multiple acquisition durations. (B) Errors of activity concentration (AC) parameters that are typically used in tumor dosimetry as a function of acquisition duration for the 17-mm sphere. The error bars represent ± 1 standard deviation.

5.3.2. Effects of respiratory motion on 3D activity quantification

Motion blurred the activity distribution of the spheres across a volume larger than the actual sphere diameter, causing underestimation of the actual sphere AC and an increase in the surrounding background AC, as shown in the sphere images and their line profiles in Fig 26. The magnitude of the underestimation depended on the relative motion amplitude with respect to the sphere diameter.

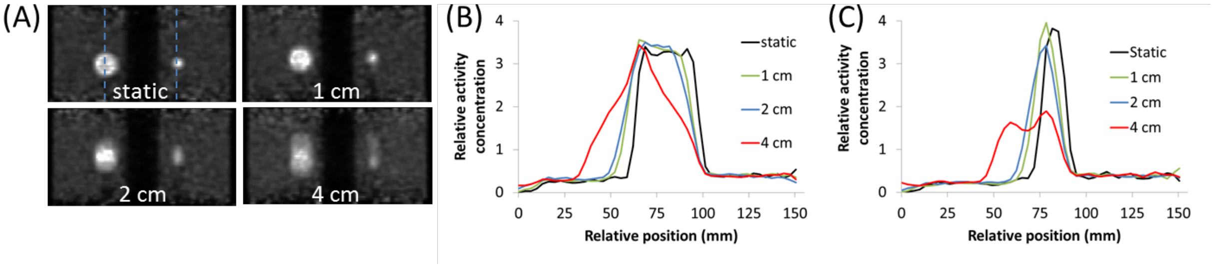

Fig 26**.** (A) Coronal PET images showing the motion blurring artifact from the breathing pattern (shown in Figure 1) on 37- and 17-mm spheres. Z line profiles of 37-mm (B) and 17-mm (C) spheres extracted from the PET images (location shown by the dashed blue lines in [A]).

The ACVHs for the spheres and the background regions under 1-, 2-, and 4-cm motion patterns are shown in Fig 27A and Fig 27B, respectively. The average errors (relative to the static case) in sphere AC_{mean} were −4%, −16%, and −52% for the 37-mm sphere under 1, 2, and 4-cm motion amplitudes, respectively; these errors increased to −6%, −27%, and −64% for the 17-mm sphere. The maximum AC (AC_0), however, was not underestimated if the relative motion was < 1, as shown in Fig 27. The errors in the other AC_X values, AC_{90}, AC_{80}, and AC_{50}, followed a similar pattern as that of AC_{mean}; the variation in errors for these parameters was about 10% from the AC_{mean}.

The ACVH was relatively unchanged by 1-cm motion for the 37-mm sphere but showed more substantial underestimation for the 1.7-cm sphere with the same 1-cm motion (Fig 27A). The error magnitude of AC_{mean} depended on the relative motion; the Pearson correlation coefficient of the error in AC_{mean} against the relative motion was 0.90 ($p << 0.001$). At small relative motion values (≤ 0.5 cm), the errors in AC_{mean} due to motion blur were small (≤ 5%).

Fig 27B illustrates the increase of AC (about AC_{30} to AC_{10}) in the region surrounding the 17-mm sphere. The increase was higher for wider motion amplitudes. Nevertheless, the ACVH errors in the background region that were attributable to motion were minimal. For 4-cm motion blur, the ACVH errors were < 10% at AC_{10} to AC_{80} because the motion blur covered only a small fraction (< 5%) of the background region VOI.

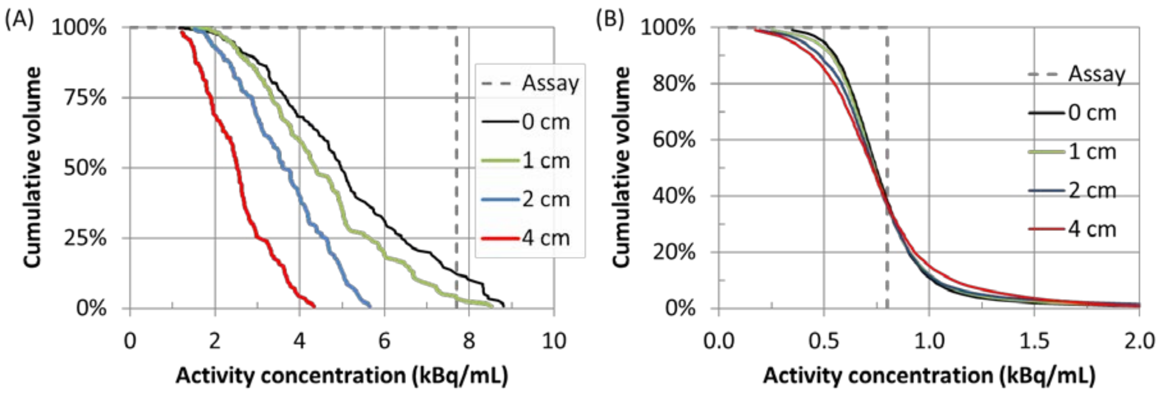

Fig 27**.** Cumulative volume histograms from volumes of interest in (A) the 17-mm sphere and (B) background regions under the static reference condition and motion with 1-, 2-, and 4-cm amplitudes.

5.3.3. Effectiveness of QPG to compensate for motion errors in 3D AC distribution in count-limited PET images

QPG (with various count fractions) reduced the severity of motion blur. As shown in Fig 28A, the narrower the QPG gate width, the greater the reduction in motion blur. The 17-mm sphere images (with 4-cm motion amplitude) that were compensated using QPG with a count fraction of 25% had less motion blur than those compensated using QPG with a count fraction of 33%. Narrower gate widths, however, had smaller total counts, which led to an increase in image noise and consequently an increase in image non-uniformity, as is evident from the stretch in the ACVH of the motion-compensated images (Fig 28B, C for the 17-mm sphere and Fig 28D, E for the surrounding background region). The increase in non-uniformity from QPG was consistent with the increase in non-uniformity from reduced acquisition duration (Fig 28). This trade-off between motion blur reduction and increase in image noise is apparent from the CNRs of the 17-mm sphere images under various conditions (Fig 28A).

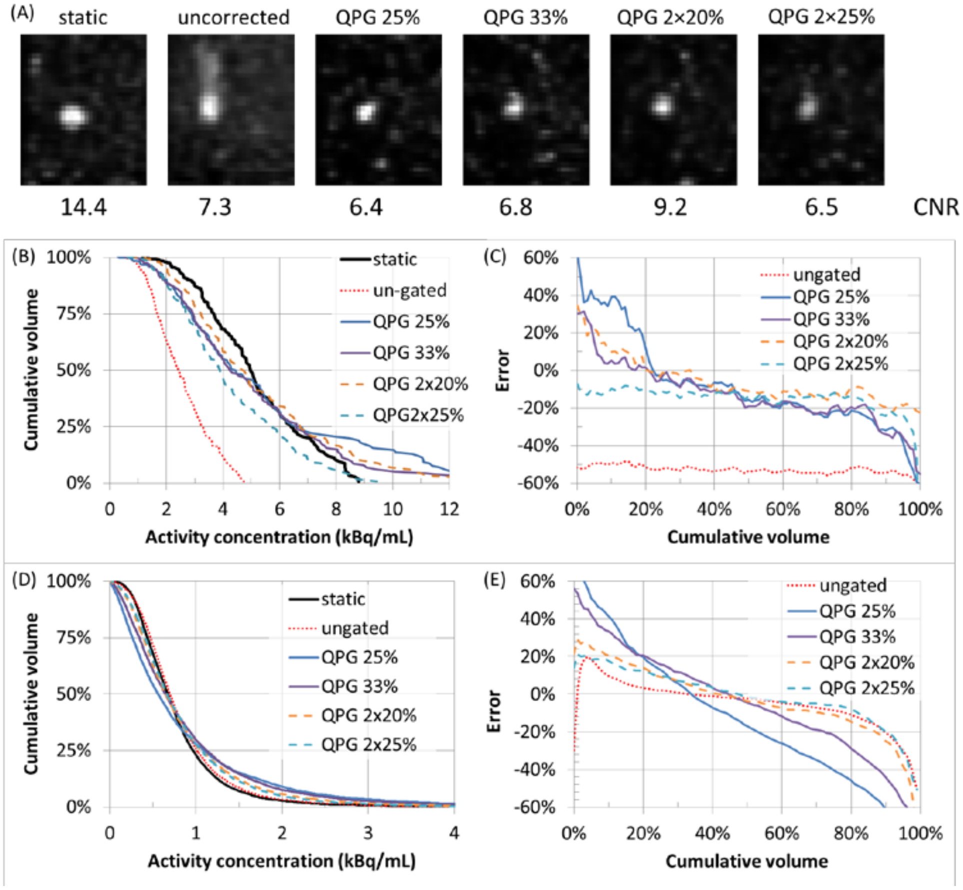

Fig 28. (A) Images of the 17-mm sphere under the static condition and with the 4-cm motion amplitude without and with quiescent period gating (QPG) with various count fractions. The contrast-to-noise ratio (CNR) of the 17-mm sphere is shown. (B, D) Activity concentration volume histogram of (B) the 17-mm sphere and (D) the surrounding background region. (C, E) Error in activity concentration coverage with respect to the static condition as a function of cumulative volume for the 17-mm sphere (C) and the background region (E).

The average errors in AC_{10} to AC_{80} were reduced from −25% and −55% to −10% and −15% for sphere images degraded by motion with amplitudes of 2 cm and 4 cm, respectively. Similarly, the underestimation of the AC_{mean} of the 1.7-cm sphere was reduced from ~30% and ~50%, respectively, to ~10% for both 2-cm and 4-cm motion. Fig 29 shows the errors in AC_{mean} before and after QPG (2 × 20%) as a function of relative motion for all sphere images (37–13 mm) under the 3 motion patterns evaluated (amplitudes of 1, 2, and 4 cm). The *t*-test indicated that the difference in the slopes before and after QPG was significant ($p = 0.029$). With QPG, the errors in AC_{mean} (with respect to the low-noise image) were reduced to about 10%, regardless of the relative motion. The QPG reduced the motion blur errors at all AC levels. AC_{40} to AC_{60}, however, suffered from errors attributable to increased noise.

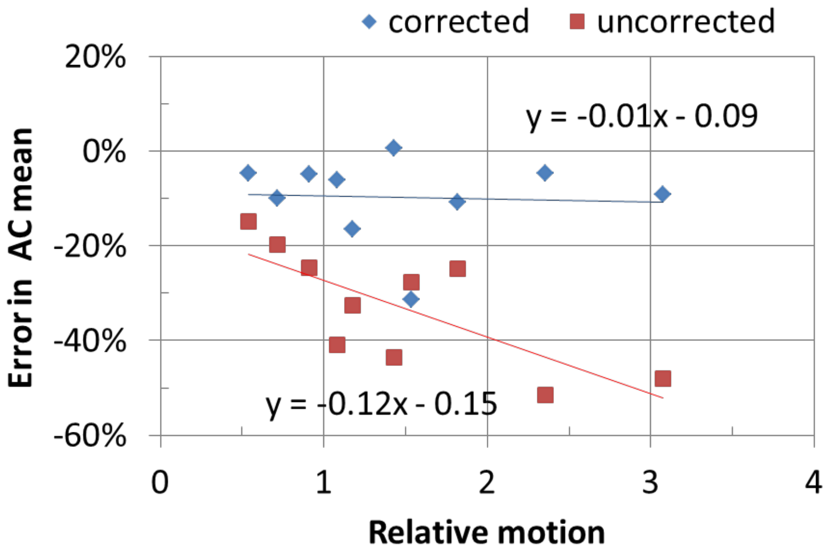

Fig 29. Errors in mean activity concentration (AC_{mean}) as a function of relative motion (motion amplitude/sphere diameter) for sphere images (37–13 mm) under 3 motion patterns (amplitude of 1, 2, and 4 cm) with and without motion compensation.

ACVH for the background region has reduced counts fractions following QPG, the errors in the ACVH after QPG were dominated by the reduction in counts. The motion errors in all cases were < 10% for AC_{10} to AC_{80}.

5.4. Discussion

5.4.1. Bias and variability in AC quantification

At the typical level of total count realized in clinical settings for ^{90}Y PET with 30 min/bed, the overall errors from both bias and variability in the static case (with no respiratory motion) for AC_{90} and AC_{80} were within 10% (Fig 25). In realistic scenarios with respiratory motion, when QPG motion compensation was used, the total count decreased to about 30%, and the expected overall error in AC_{90} and AC_{80} was > 50%. In this case, AC_{50} and AC_{mean} were less sensitive to the total count reduction. Dose-response studies of both brachytherapy (70) and other radiopharmaceutical therapies, such as ^{131}I (29) and ^{177}Lu (97), have suggested a strong correlation between AC_{90} (or AC_{80}) and tumor response metrics. Furthermore, these studies also demonstrated that AC_{mean} (or AC_{50}) was not significantly correlated with tumor response. AC_{60}–AC_{80}, which may be more relevant to tumor dosimetry, had errors of about −15% at an acquisition duration of 16 s (33%) or 10 min/bed for ^{90}Y PET.

It is noteworthy that in this study, the 100% sphere total count represents a tumor with an AC of 6 MBq/mL acquired for 30 min/bed. (24)(2013) found that tumor AC ranged from 2000 to 13000 kBq/mL. Assuming a local deposition method (35, 51) to convert the AC map to the dose map, an AC of 6 MBq/mL would result in a tumor dose of 290 Gy, which is in agreement with the finding from (22) (2013). Depending on the actual tumor AC and the acquisition duration, the overall errors may vary.

5.4.2. Effectiveness of QPG to compensate for motion errors in 3D AC distribution in count-limited PET images

QPG shows potential for reducing errors in ACVH in quantitative ^{90}Y PET/CT studies that suffer from motion blur. Qualitatively, a single-gate QPG, e.g., QPG 25% or QPG 33%, did not show improvement in sphere detectability (measured using CNR). Although the sphere image showed a reduction in motion blur, it also displayed increased noise (Fig 30A). Quantitatively, sphere images with QPG motion compensation improved ACVH over uncorrected ACVH, i.e., the compensated ACVH was closer to the static ACVH.

As shown in Fig 30 the total counts limit the effectiveness of QPG. After QPG with a count fraction of 33%, the compensated ACVH of the 17-mm sphere under both 2-cm and 4-cm motion agreed with that of the ACVH of static images with a 33% total count. A noise-related error of 15% in AC_{60}–AC_{80} for the 17-mm sphere image acquired for 16 s was also achievable after QPG with similar image noise (Fig 30B). For tumors with relative motion ≥ 0.5, QPG with various count fractions can be applied to reduce the errors in ACVH.

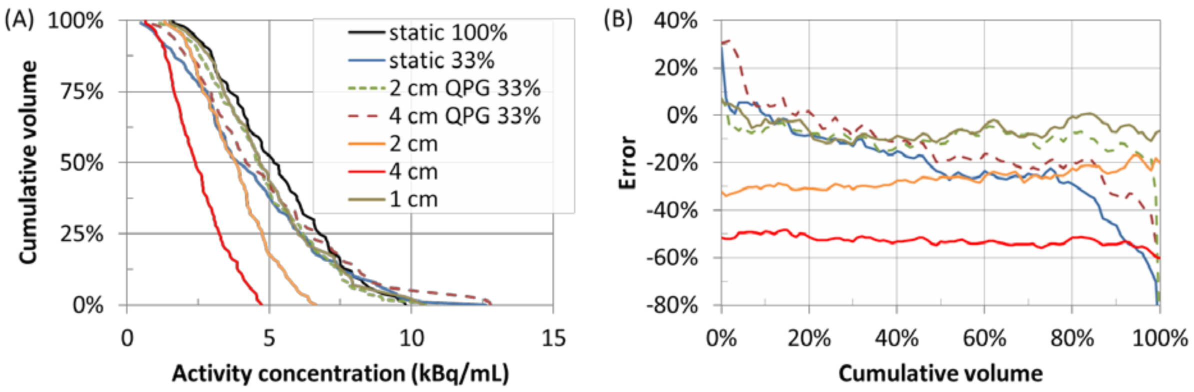

Fig 30. (A) Activity concentration volume histogram (ACVH) of the 17-mm sphere under static condition, with motion without correction, and with quiescent period gating (QPG) motion compensation (33% count fraction). (B) Differences in the ACVH curves in (A) with respect to static ACVH (100% total count) as a function of cumulative volume. Note: figure legend in (A) and (B) are the same.

Registration of 2 adjacent gated images during the quiescent period increases the total count and reduces noise. However, gated images acquired during the quiescent period may not be completely motionless, depending on the breathing motion pattern. The images may also have different residual motion, as shown in Fig 28. For instance, QPG 25% will have less motion blur than QPG 2 × 25%. Consequently, the sphere CNR of QPG 2 × 25% is comparable to that of QPG 25%, as illustrated in Fig 28A.

Optimizing the trade-off between the motion blur reduction and the increased noise is beyond the scope of this study, as such optimizations strongly depend on the specific imaging conditions and imaging tasks; therefore, optimization needs to be performed on a case-by-case basis. As an example, for the 17-mm sphere, QPG 25% reduced the errors in ACVH better than QPG 2 × 25% did for 2-cm motion. However, for 4-cm motion, QPG 2 ×

25% yielded lower ACVH errors than did QPG 25%, although the sphere CNR was comparable (Fig 28A). Another practical consideration is that in clinical settings, deformable image registration may be required, and misregistration errors will produce errors in AC quantification (45, 89, 98). In addition, the errors in the ACVH of the background region are dominated by the errors from noise; the errors due to motion were < 10%. Our results suggest, therefore, that the QPG method is not effective for motion compensation in the background region (Fig 28D and Fig 28E).

Our data show that QPG need not be applied to tumors with relative motion < 0.5, i.e., with motion amplitude half of the tumor size. Applying QPG in such cases results in an error in AC_{mean} of about 10% (Fig 29). In these cases, the errors in activity quantification introduced by motion are of the same order as, if not smaller than, the errors introduced by the reduced total count. In a real clinical case, respiratory motion is the largest in the superior-inferior direction, with a typical amplitude of about 2 cm. By comparison, hepatocellular carcinoma tumors are typically > 2 cm, while metastatic liver tumors from colorectal cancer are typically < 1 cm.

5.4.3. Study limitations

Although the specific count-limited study of interest is ^{90}Y PET images, we used low amount of ^{18}F after careful matching of the total positron emissions to evaluate the noise trade-off of using QPG to compensate for respiratory motion. Furthermore, we do not expect substantial differences in intrinsic image resolution because the maximum positron energies of ^{18}F and ^{90}Y are very close (0.635 MeV vs. 0.63 MeV, respectively) (25, 99). The overall image quality, however, may be somewhat different because random coincidence event from bremsstrahlung photon and prompt gamma detection may not be modeled properly in ^{90}Y-PET image reconstruction, which is optimized for ^{18}F imaging (27, 100).

Second, we used an IEC phantom, which has uniform activity distribution in both spheres and background, to represent tumor tissue and normal liver tissue. In reality, the geometry and activity distributions in tumors and normal liver background are not necessarily homogeneous. Further studies using anthropomorphic phantoms and/or clinical ^{90}Y PET/CT studies are needed to evaluate the effectiveness of QPG for motion compensation and to determine the optimal count fraction for use in clinical studies. Our study also used a single SBR of 10, which is typical for the ^{90}Y-microsphere tumor-to-background ratio reported by some PET/CT clinical studies (24). We expect that changes in SBR will change the magnitude of the observed phenomena, but will not change the general trend.

Third, we only considered 1D periodic motions with a period of 4 s and fixed amplitudes of 1, 2, and 4 cm because of tracking device hardware limitations. Irregular motions may introduce additional uncertainty in AC quantification (42, 43, 90). We expect that different periods, however, will only change the relative motion range in the gated images.

Fourth, we did not correct for partial volume effects beyond using the built-in point spread function correction in GE VuePoint. However, we excluded partial volume effects as a potential source of error by using the reference static images.

Finally, we only considered the QPG single-gate and double-gate summation regimes. Motion correction techniques that avoid increasing acquisition duration are under development, including pre-reconstruction corrections that use data-driven approaches and motion corrections for use during image reconstruction (101). These methods, however, are not yet commercially available for clinical use. It would be valuable to evaluate whether these data-driven correction methods will benefit count-starved ^{90}Y PET studies as much as they do high-count ^{18}F studies.

5.5. Conclusion

Caution needs to be exercised when using ACVH parameters such as AC_{90} and AC_{80} to calculate absorbed dose because the ACVH is susceptible to image degradation from both image noise and respiratory motion. When using gating-based motion compensation, e.g., the QPG method studied here, with 33% total count in the gated image, the overall error (bias and variability) in AC_{90} and AC_{80} can be over 60%. The AC_{mean} seems to be less sensitive to image noise, but its correlation with clinical response to radiation therapy has not yet been established.

The average error in sphere ACVH (from AC_{10} to AC_{80}) with relative motion (motion amplitude/sphere diameter) less than about 0.5 was found to be < 10%. QPG can be used to reduce motion blur artifacts and reduce the errors in sphere ACVH down to 10–15% (limited by the total count acquired), but at the expense of increased image noise. QPG was found to be ineffective for the quantification of background AC distribution.

Chapter 6: Discussion

6.1. Summary

The hypothesis of this dissertation work was that optimization of Y90 emission data reconstruction can maintain the overall errors (systematic and random) in volumetric dose quantification to < 20% in clinically relevant imaging conditions

Hence the main objectives were 1) to optimize the emission data reconstruction, and 2) to characterize both systematic and random errors in volumetric dose quantification from the optimized emission images.

We tested the hypothesis on both SPECT in specific aim 1 (Chapter 2) and on PET in specific aim 2–4 (Chapter 3–5) images.

We developed a practical protocol for improving image quality and quantification of bremsstrahlung SPECT/CT (bSPECT) imaging in specific aim 1. We found severe partial volume effect (PVE), where the systematic bias in mean dose of 37-mm sphere > 50%, due to electron staggering in bremsstrahlung photon production and sub-optimal collimator design to image bremsstrahlung photons. Because of high systematic errors due to PVE, volumetric dosimetry using bSPECT is very challenging; Monte-Carlo simulation based image reconstruction and/or a bSPECT-optimized hardware design are needed to improve the image resolution. Nevertheless, we have shown that with proposed CT attenuation correction and background compensation, we can accurately quantify the total ^{90}Y activity delivered to the patient with errors < 5%.

In specific aim 2, we optimized PET image reconstruction parameters (equivalent iterations and filtration full width at half maximum) for volumetric ^{90}Y dosimetry by minimizing the root mean square errors in the image-based dose volume histogram estimates (DVH'). In the process, we also minimized the systematic error in the quantitative image/dose map due to noise realization in image noise. For ordered subset expectation maximization with time of flight and point spread function correction algorithm in General Electric PET/CT system, the optimal reconstruction parameters were 36 equivalent iterations with 5.2-mm post-reconstruction filtration. Using these parameters, spheres under various clinically relevant imaging condition (diameter > 17 mm, sphere-to-background ratio > 4, sphere dose > 40 Gy, acquisition duration > 10 min) were found to have minimum errors in DVH'.

The systematic and random errors in DVH' were characterized in specific aim 3 and 4. In specific aim 3, we showed that the (additional) systematic errors due to image noise (manifestation of low signal) were < 10% for clinically relevant imaging condition tested. The systematic errors in DVH' were still dominated by the PVE (> 30%), even at count-limited study ^{90}Y PET. The random errors (measurement repeatability), however, were governed solely by the low signal. Random errors of < 10% can be expected in DVH' of sphere images under relevant clinically imaging condition, provided that the acquisition duration of 30 min. Under shorter acquisition duration (e.g. 10 min) or if gating-based motion compensation method (e.g. quiescent period gating) is applied, then sphere with diameter ~17 mm will have random errors of > 15%; even though larger sphere (e.g. 37-mm sphere) will still have random errors < 10% at sphere dose> 80 Gy. To keep random errors <

10–15%, longer acquisition duration is required; in clinical practice, the maximum practical limitation will likely be 30 min/bed for 2 bed positions (60 min total duration).

In specific aim 4, we characterized a specific source of systematic errors, namely motion blur. We found that without any motion compensation, spheres with relative motion range (motion amplitude/sphere diameter) > 0.5, errors in DVH’ > 20%. Using gating-based motion compensation (QPE method), we traded off the systematic errors due to motion with a combination of systematic and random errors due to low signal (from gated data). Although we have shown that the systematic errors due to motion blur can be reduced to <10%—which is consistent with systematic errors due to increased image noise found in specific aim 3—the random errors increase due to data gating with magnitude depending on the sphere diameter and acquisition duration such that spheres with motion range < 0.5 will not benefit from QPG and spheres with motion range > 1 will likely benefit from QPG. The total errors reduction using QPG will vary on case-by-case basis; hence it would be recommended that motion tracking is performed on all ^{90}Y PET scan such that the QPG method can be applied when deemed necessary.

Our finding from development of practical bSPECT did not support our central hypothesis since bSPECT images suffer from very high PVE even at 37-mm sphere. Volumetric dosimetry using bSPECT will suffer errors >> 50%. Data from specific aim 2–4, on using optimized PET images to estimate DVH’, support the central hypothesis under certain imaging condition: effective tumor diameter > 37 mm, average tumor dose > 60 Gy, acquisition duration > 10 min. Under this imaging condition, the errors in dose that covers 80% of the volume of interest are < 30%. The errors in D_{mean} and D_{70} are < 20%.

6.2. Listed contributions of this dissertation

6.2.1. Physics contributions

1) Characterization of the impact of low count (a unique challenge in ^{90}Y PET) on systematic and random errors in volumetric dosimetry.

2) Characterization of the impact of motion blur and the effectiveness of QPG in trading-off motion blur and reduced count in an already count-limited ^{90}Y PET study.

3) Establishing the expected errors (systematic and random) in image-based dose volume histogram.

6.2.2. Clinical contributions

1) Development of practical bSPECT image reconstruction for improved image quality and limited quantification.

2) Development of practical PET/CT image reconstruction for volumetric ^{90}Y dosimetry.

3) Establishing the robustness of the dosimetry metric (DVH' summary metrics) which is important in developing dose-response model.

6.3. Future directions

6.3.1. Continuation to minimize errors in volumetric ^{90}Y dose quantification

6.3.1.1. Robustness of volumetric ^{90}Y dosimetry in heterogeneous distribution

One of the major limitations in our present work is that we represent liver tumor using spheres with uniformly distributed ^{90}Y dose. In reality, the ^{90}Y dose distribution in the tumor is heterogeneous, which increases the complexity of correcting DVH' for PVE, dose-dependent error, etc. In the future, we plan to characterize the errors in DVH' for (pseudo) heterogeneous distribution, for example by using a cluster of smaller spheres.

6.3.1.2. Partial volume correction

We have shown that despite having very limited counts, the errors in volumetric ^{90}Y dosimetry calculated from both bSPECT and PET images are still dominated by PVE; therefore effort to improve volumetric ^{90}Y dosimetry should first focus on partial volume correction.

In our present work, we used the point-spread-function (PSF) correction available on GE OSEM algorithm (Vue Point). While the errors in mean dose (D_{mean}) are reasonable (< 10% for 37-mm sphere), the errors toward minimum dose (e.g. D_{80}) are > 30% for 37-mm sphere with minimal systematic errors due to image noise. Traditionally for quantitative diagnostic imaging, where Dmean is the quantity of interest, partial volume correction can be carried empirically using look-up correction factors for different object sizes based on phantom studies. In post-therapy ^{90}Y imaging, however, the summary DVH' metric of interest has not yet been determine and hence we remain interested in a wide range of DVH' metrics (e.g. D_{20}–D_{80}). We hypothesize that the empirical partial volume correction method to correct for D_{mean}, can be extended to correct for DVH' by using correction functions, which is subject to our future study.

More complicated partial-volume-correction methods that involve the use of prior image information (e.g. CT or MRI images) can be very challenging to be applied for ^{90}Y microsphere studies; the mechanistic nature of microsphere distribution means that the distribution of microsphere is not confined to the tumors only. The microsphere distribution needs to be match with the vasculature which may not be resolveable in the CT or MR images, or otherwise may not be feasible to co-register the anatomical images with the PET or SPECT images.

6.3.1.3. Breathing motion correction

^{90}Y PET data needs to be acquired for a long duration, 30 min/bed at least because the signal in ^{90}Y PET comes from a very low positron yield of 32 ppm. The number of counts in ^{90}Y PET data is a scarce commodity. In QPG method, however, we used only 33% of the counts collected, which leads to increase in both systematic and random errors in volumetric ^{90}Y dosimetry.

Ideally in ^{90}Y-PET/CT study, we want to reconstruct the PET images using all the acquired data by combining the gated data during image reconstruction(89, 102) or by spatially registering all (post reconstruction) gated images(103, 104) together. The latter may not be feasible in ^{90}Y PET because gated PET images suffers from errors due to higher noise penalty(89), while gated CT are subject to temporal mismatch (43, 90) between several seconds CT data with up to 60 min PET data. Combining the gated data during image reconstruction using motion pattern from real-time position management device or data-driven method may allow more effective error reduction in DVH' compared to QPG method.

6.3.1.3. Development of dose-response model to predict treatment outcome

The long term goal of this project is to be able to predict the efficacy of ^{90}Y microsphere therapy based on the post-therapy images. To achieve this goal, we need to develop a dose-response model. In this dissertation work, we characterized the robustness of potential dose metrics (e.g. D_{70} or D_{mean} that have been used by other studies) that may have (strong) correlation with tumor response. Evaluation of which dose metrics have strong correlation with tumor response cannot be done with our phantom study, since development of dose-response model, obviously, need the tumor response data, i.e., clinical data, which are absent in this dissertation work. In the future, we would like to develop the dose-response model by correlating dose metrics with patient outcome.

Appendix

A1. Evaluation of Step-and-Shoot and Continuous-Bed-Motion modes of acquisition for limited-view organ scans

A.1.1. Introduction

The continuous-bed-motion (CBM) mode was originally developed to improve axial image uniformity in whole body imaging in 2D step-and shoot (SS) acquisition mode(105), where there were sensitivity variations in the axial direction due to gaps between detector blocks(106). The axial uniformity, however, is no longer a problem in modern PET/CT scanners utilizing 3D SS acquisition mode, where the axial uniformity in 3D acquisition can be improved by overlapping the end slices of adjacent bed positions and adding the overlapped data(107). Theoretically, CBM mode may also allow oversampling in the z-axis direction and produce super-resolution images(108); however, this super-resolution effect is not realized in clinical practice due to high level of noise(106).

The true clinical benefit of CBM is the ability to tailor fit the PET/CT scan length and local scan duration based on the imaging task. In traditionally SS mode, the PET scan length increases in steps of the PET z-axis field of view (aFOV) depending on the amount of detector overlap between bed positions. Hence, the ability to tailor fit the PET/CT scan length allows modest CT dose saving and facilitates trading off the scan length with the total scan duration. In multi-bed SS acquisitions, the PET acquisition duration per bed is also fixed; whereas in CBM mode, the local acquisition duration can be modulated along the z-axis adjusted by varying the bed speed; hence allowing acquisition of higher counts in regions of greater interest. In addition, clinical practice has also suggested that patients find CBM more comfortable compared to SS acquisition(109).

Recently, the CBM acquisition mode has been made commercially available in Siemens Biograph mCT Flow (Siemens Medical Solutions USA, Knoxville, TN). The CBM acquisition mode is intended for whole body PET/CT imaging with long scan length (multiple aFOVs). The benefits of CBM mode in clinical whole body imaging have been studied(106, 110). The benefits of CBM acquisition mode in short scan length studies, however, have not been investigated. The objective of this work is to evaluate the potential differences in the counting efficiency profiles along the z-axis between CBM and SS modes of acquisition for limited-view organ studies, such as ^{90}Y PET/CT liver scan, where the scan length is short (≤ 2 aFOV) and the scan duration is long(28, 111) ($\leq 30\ min/bed$). We also discuss the implication of these differences on the image quality and quantification of ^{90}Y-PET/CT liver scan.

A.1.2. Methods

A.1.2.1. Analytical comparison of counting efficiency in CBM and SS modes

A.1.2.1.1.Counting efficiency profiles in 3D SS acquisition mode

The sensitivity (count rate per unit activity) profile of PET acquisition is proportional to the volume of response (VOR) accepted for a given geometry(112). In 3D SS acquisition mode, the VOR at any given axial position along the PET bed is proportional to its distance from the edge of the aFOV, i.e., the VOR is the largest at the center and the smallest at the edges of the aFOV (Fig 31A). The 3D SS acquisition therefore has a triangular sensitivity profile for scan length of 1 aFOV (Fig 31B). For multi-aFOV SS acquisition, the overall sensitivity profiles can be calculated by adding the count profiles of each individual aFOV acquisitions accounting for the amount of bed overlap (Fig 31C). In reality, the axial sensitivity profile is not exactly triangular but has a saw-tooth shape with a plateau depending on the axial compression that is used on the scanner , the maximum acceptance angle, and the number of detectors used. An ideal simplification of sensitivity profile is used to conceptually illustrate sensitivity/bed overlap in 3D SS modes.

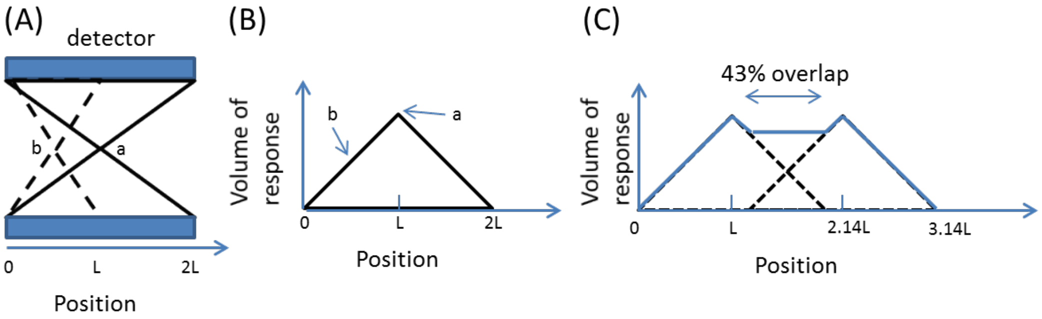

Fig 31. (A) Volume of response (VOR) in 3D step-and-shoot (SS) acquisition at two locations: a and b. The VOR varies linearly as a function of distance along the axial (z-axis) field of view (aFOV). (B) For a single aFOV, the VOR and the sensitivity as a function of position has a triangular profile. (C) For two-aFOV SS acquisition, the VOR profile as a function of position is simply a summation of the individual aFOV profiles at each bed position taking into account the amount of bed-overlap; 43% aFOV overlap in Siemens mCT is illustrated.

The number of counts in an image slice is proportional to the integral of its VOR over time. For a uniformly distributed activity along the bed motion direction (z axis), the z-axis count profile $C(z)$ can be calculated as

$$C(z) \propto \int_{0}^{t_{dur}} VOR(z)dt = VOR(z) \times t_{dur} \ , \tag{1}$$

where $VOR(z)$ is the volume of response at slice z and t_{dur} is the acquisition duration. In SS mode, the VOR varies only as a function of location inside the aFOV; hence the count profile is proportional to the VOR.

A.1.2.1.2.Counting efficiency profiles in CBM mode

In CBM mode, the object is moving along the z-axis; hence during the acquisition, the VOR for slice location z changes over time. The variation of the VOR at location z as a function of time, $C_z(t)$, is illustrated in Fig 32. For Siemens mCT scanner, the CBM mode is acquired with 50% overscan, i.e., the scan prescription begins and ends at the center of the detector aFOV(106). In this configuration, the count profile for a uniform cylindrical source consists of 1/2-aFOV-long ramp up and down regions at the beginning and end with a flat constant profile in between (Fig 32C). Following equation (1), the count profile for CBM can be expressed as:

$$C(z) \propto -\frac{z^2}{2Lv} + \frac{z}{v} + \frac{L}{2v} \qquad , for\ 0 \le z \le L,$$

$$C(z) \propto \frac{L}{v} \qquad , for\ L \le z \le L + d, \tag{2}$$

$$C(z) \propto -\frac{z'^2}{2Lv} + \frac{z'}{v} + \frac{L}{2v} \qquad , for\ L + d \le z \le 2L + d,$$

where z is the image slice position along z-axis, L is half of the FOV length, d is the length of the uniform region, v is the bed speed, and $z' = -(z - 2L - d)$. Note that d is equal to the total scan length minus $2L$. In reality, the actual efficiency profile depends on a large number of hardware and software parameters that include the detector segments used and the scan extend outside the aFOV. We have once again simplified the theoretical derivation of the axial efficiency to conceptually illustrate the sensitivity profile in CBM mode.

The PET and the CT acquisition have a matching scan length prescription, which does not account for the 50% overscan in PET acquisition. Due to the missing CT-based attenuation correction factors outside the PET/CT scan prescription, the coincidence counts acquired in the VOR outside the scan prescription cannot be used in the quantitative PET image reconstruction(106). As illustrated in Fig 32, the volume of response and, therefore, the count profile at the axial extends of prescribed scan regions are limited by the attenuation correction unavailability rather than limited by the acquisition geometry. Similar to the ideal CBM case, following equation (1), the count profile for observed CBM mode can be expressed as:

$$
\begin{aligned}
&C(z) \propto \frac{3z}{2v} - \frac{z^2}{2Lv} && , for\ 0 \le z \le L, \\
&C(z) \propto \frac{L}{v} && , for\ L \le z \le L + d, \\
&C(z) \propto \frac{3z'}{2v} - \frac{z'^2}{2Lv} && , for\ L + d \le z \le 2L + d,
\end{aligned}
\tag{3}
$$

Note that contrary to the ideal CBM case, in practice $C(0) = 0$.

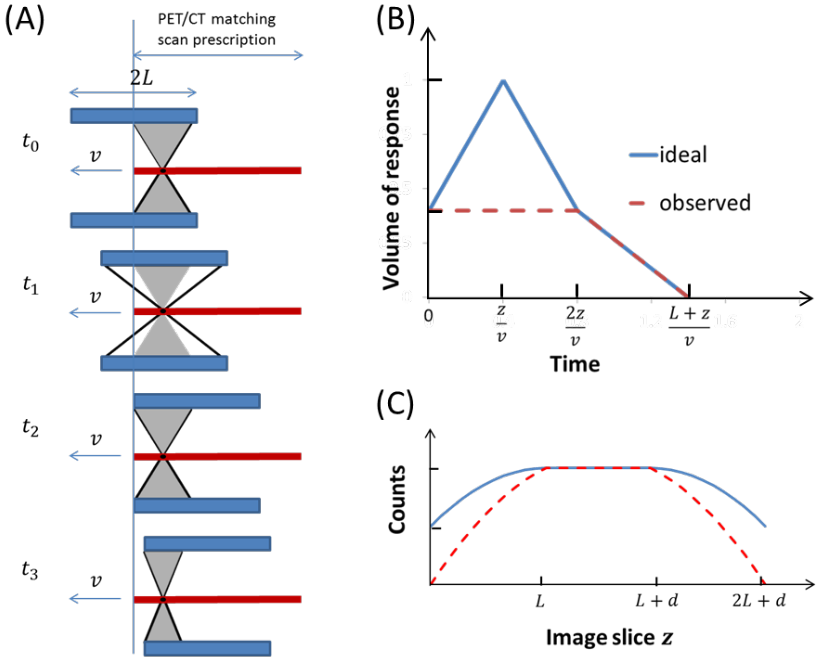

Fig 32. (A) The variation of the volume of response (VOR) at location $\boldsymbol{z = 0.4L}$ (black dot) at time *t* is illustrated by the empty and shaded triangles for ideal and practical cases, respectively. Note that the continuous-bed-motion (CBM) acquisition starts with the edge of the prescribed scan region located at the center of the axial field of view. (B) Graph of the VOR and (C) net counts at location $\boldsymbol{z}$ as function of time in the ideal CBM (solid blue) and

practical CBM (red dash) modes. The variation in VOR at time points illustrated (A) are indicated in (B). As expected the counts are lower in the practical CBM at the ramping up and down regions. The profiles are derived for a CBM acquisition with 50% overscan.

A.1.2.1.3.Analytic comparison of counting efficiencies in SS and CBM modes

We compared the count efficiencies of three different modes of PET data acquisition: 3D SS acquisition for 1 aFOV, 2 aFOVs, and CBM acquisition for the same acquisition duration. For 2-aFOV scan, the acquisition duration for each bed position was half of the acquisition duration in 1-aFOV scan to maintain the same total duration. The scan lengths for 1-aFOV, 2-aFOV, and CBM were 22, 35, and 24 cm, respectively. The scan length of 24 cm was chosen for CBM to provide a scan length similar to 1-aFOV while maintaining scan duration of 40 min at the slowest bed speed of 0.1 mm/s.

A.1.2.2. Experimental verification of counting efficiencies in SS and CBM modes

All PET/CT images were acquired using Siemens Biograph mCT Flow featuring the CBM acquisition mode (Flow Motion). The scanner has a bore diameter of $78\ cm$ and an axial field of view (aFOV) of 22-cm (4-ring detector configuration). The system is also time-of-flight (TOF) capable with nominal timing resolution of $0.555\ ns$.

A 2-mCi ^{68}Ge daily QC phantom with length of 27 cm and diameter of 20 cm was scanned using 3 PET acquisition modes described previously: 1 and 2-aFOV SS, and CBM modes to derive the count density profiles of each mode. The acquisition parameters were the same as those used for analytical comparison (Material and Method section 1c). All

PET/CT images were reconstructed using TOF information with CT attenuation correction, PSF modeling, scatter correction, and OSEM iterative reconstruction (TrueX, Siemens Medical Solutions) with subset and iteration of 2×21.

For all transaxial slices, the means and standard deviations of the reconstructed activity concentration were extracted from a 40-cm^2 ROI placed at the center of the phantom images. Based on our observation, the PET image noise follows a Poisson-like distribution, i.e., $image\ noise\ \propto counts^{-0.51}$; therefore the relative count density profiles were computed from the relative noise measurements of the ROIs as:

$$C \propto \frac{1}{\sigma_{rel}^2} = \left(\frac{mean}{stdev}\right)^2. \tag{4}$$

The relative count profiles along z axis were calculated for all 3 PET acquisition modes. These relative count profiles were then compared to the analytically derived count profiles (Material and Method section 1b) for validation.

A.1.3. Results

A.1.3.1. Comparison of the sensitivity profiles in CBM and SS modes

The theoretically derived count density profiles are shown together with the experimentally computed count profiles for 1- and 2-aFOV SS, and CBM modes in Fig 33. The measured profiles for 1-aFOV and CBM with axial scan lengths of 22 cm and 24 cm, respectively, are in good agreement with the theoretically derived profiles. However, the measured profile for 2-aFOV with axial scan length of 35 cm is not fully characterized in the axial direction because the phantom used for the measurements is shorter in length (only ~27 cm). Nonetheless, agreement between measured and theoretical profiles for SS 2-aFOV scans can be fully appreciated in the positive positions where the phantom extends fully. The measured profiles are noisy while the analytically profiles were derived under idealized assumptions, yet there is reasonably good agreement between them.

The measured profile from CBM acquisition has been demonstrated to be less efficient compared to the ideal CBM case, as explained in Materials and Methods section 1b, due to unusable data due to missing attenuation correction factor in the overscan region. For fixed scan durations, the overall counting efficiency of CBM mode is lower compared to those of 1- and 2-aFOV SS acquisition modes in terms of total PET signal (area under the curves). CBM mode only acquired $\sim 60\%$ of the total counts acquired in the SS acquisition modes for the same acquisition duration. In addition, for the same acquisition duration, the ratio of the maximum counts in the CBM to 1-aFOV SS modes is proportional to $aFOV/(2 \times scan\ length_{CBM})$, i.e., the maximum-count images in the CBM is $\leq 50\%$ of those for 1-aFOV SS mode, and $\leq 100\%$ of those for 2-aFOV SS mode.

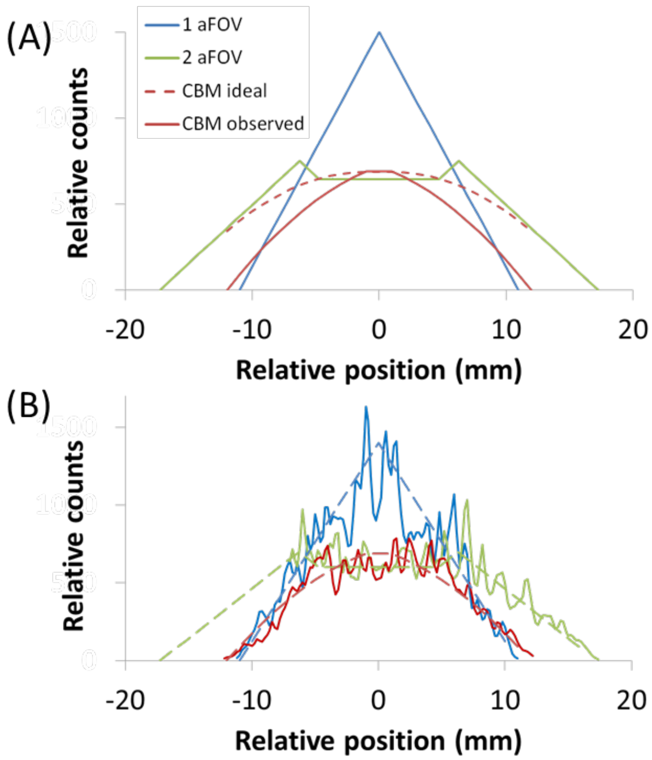

Fig 33. (A) Comparison of the analytically derived counting efficiencies for a uniform line cylindrical source acquired using step-and shoot (SS) acquisition mode (scan lengths of 1 and 2 aFOVs) and continuous bed motion (CBM) mode. All profiles are aligned at the central slices to compare the trade-off between counts and scan length. The ideal CBM profile (red dash) shows the counting efficiency for a geometry-limited CBM mode, while observed CBM profile (solid red line) shows the counting efficiency realized in the CBM mode with missing attenuation correction in the overscan region. (B) The profiles from analytical derivation (dash line) showing good agreement with the experimentally derived count profiles (solid line) for 1- and 2-aFOV SS, and CBM acquisition modes. The counting efficiency of CBM mode is less efficient compared to the SS mode. The measured profiles for 1-aFOV and CBM with axial scan lengths of 22 cm and 24 cm, respectively, are in good agreement with the theoretically derived profiles. However, the measured profile for 2-aFOV

with axial scan length of 35 cm is not fully characterized in the axial direction because the phantom used for the measurements is shorter in length (only ~27 cm).

For a short scan length of 1 aFOV, i.e., $\sim 22\ cm$, a plateau of lower relative noise (based on the relative count density profiles) with 1-aFOV SS mode was realized for a region of $\sim 14\ cm$ around the center of the axial FOV. The extent of the lower noise plateau region decreased to $\sim 10\ cm$ for 2-aFOV SS and CBM modes. The 2-aFOV SS mode, however, does provide 11 cm additional axial scan coverage than CBM mode, i.e., 35 cm compared to 24 cm, for the same acquisition time.

A.1.4. Discussion

A.1.4.1. Effects of acquisition modes on image quality and quantitation

Both SS and CBM PET acquisition modes allow for trade-off between the counts per unit (axial) distance and scan length for fixed acquisition duration. With SS mode the increments in scan length are in terms on a fixed fraction of PET aFOV depending on the prescribed bed-overlap; with CBM, however, the scan length can be increased in increments of prescribed table speed allowed. For the same acquisition duration, the maximum count efficiency (at the central images) for CBM mode is less than or equal to half of that for 1-aFOV SS acquisition mode and less than or equal to the maximum count efficiency for 2-aFOV SS acquisition mode. For the same scan length and scan duration, CBM mode only collected $\sim 60\%$ coincidence counts that are collected in the 1-aFOV SS mode. For the same acquisition duration, the maximum count efficiency of a 2-aFOV SS acquisition relative to a 1-aFOV SS mode depends on the amount of bed overlap; it is half for 50% bed-overlap.

A.1.4.2. CBM versus SS modes for organ scan

The primary advantages of the CBM mode compared to the SS mode are that the CBM mode offers uniform axial sensitivity profile and it facilitates effective trading between scan length and scan duration. These advantages, however, are not realized in scans of limited axial coverage such as scans of liver or other organs. For organ studies with scan lengths less than $\sim 30\ cm$, tailor fitting the scan length becomes less practical. As discussed in detail in the material and method section 1, the CBM count density is not uniform for the first and the last halves of the aFOV. For a scan length ≤ 2 aFOV, these non-uniform regions comprise $\geq 50\%$ of the total scan length.

The usefulness of CBM mode is even more restricted in studies with short scan length and long scan duration such as ^{90}Y liver PET/CT ($10 - 30\ min/bed$). The slowest speed setting in CBM is $0.1\ mm/s$ and the speed has the finest increment of $0.1\ mm/s$. For a typical liver length of $24\ cm$, the scan duration can be set to a maximum of $40\ min$. Since the next available speed setting is $0.2\ mm/s$, the next available duration to cover the 24-cm liver scan is $20\ min$. Due to its finite bed speed increments, CBM mode losses its ability to effectively trade scan lengths and durations for exams requiring long scan durations such as ^{90}Y PET/CT. For a short scan with long duration, SS mode gives greater flexibility in scanning duration with net higher counts detected for 1-aFOV scan length, and net longer scan length coverage with at least comparable net counts for 2-aFOV scan length.

For a count-starved study like ^{90}Y PET/CT, the counting efficiency is of importance because the image quality and quantification are strongly dependent on the number of coincidence count detected during the acquisition. Since SS acquisition has higher counting efficiency compared to CBM mode, SS acquisition is more suitable for organ scan with limited scan length and long scan duration like ^{90}Y liver PET/CT.

A.1.4.3. Limitations

In this work, we presented simplistic models to characterize the counting efficiencies across the aFOV both in the SS and CBM modes. Even though these idealized models do not incorporate details(106) about data acquisition, splitting, correction and image reconstruction, they were still effective to demonstrate the difference in the counting efficiencies between the SS and CBM modes.

It is important to note that the lack of attenuation information outside the CBM aFOV may be overcome by more advanced reconstruction algorithms (e.g., data driven) or altering the CBM scan protocol (e.g., operating CBM at high bed speeds at the two end of FOV). Use of attenuation corrected PET signal from outside the CBM scan prescription will help push CBM sensitivity profile similar to that of 2-aFOV SS in central region (as shown in Figure 3A).

The primary objective of this study was to optimize the acquisition protocol for post-therapy microsphere ^{90}Y-PET/CT studies; we, however, used ^{68}Ge phantom as a surrogate radionuclide. ^{68}Ge and ^{90}Y may have differences in the absolute sensitivity, scatter properties, singles, random coincidence, and resolution; nevertheless, the relative counting efficiency in different acquisition modes should be similar. Using ^{68}Ge instead of ^{90}Y allowed us to acquire higher counts in shorter duration with lower radioactivity.

A.1.4.4. Conclusion

The benefits of CBM mode is severely challenged in studies with short scan length ($\leq 30\ cm$), due to non-uniform count density in the first and the last halves of the aFOV, and long scan duration ($20\ min/aFOV$), due to limitation in the bed speed increment of $0.1\ mm/s$. The SS acquisition mode is preferable to CBM mode for count-starved ^{90}Y-PET/CT livers scans due to having higher counting efficiency, which will lead to better image quality and quantification precision.

Bibliography

1. Ferlay, J., I. Soerjomataram, R. Dikshit, S. Eser, C. Mathers, M. Rebelo, D. M. Parkin, D. Forman, and F. Bray. 2015. Cancer incidence and mortality worldwide: Sources, methods and major patterns in GLOBOCAN 2012. *Int. J. Cancer* 136: E359–E386.

2. Cancer Facts & Figures 2016 | American Cancer Society. .

3. Shah, S. A., J. K. Smith, Y. Li, S. C. Ng, J. E. Carroll, and J. F. Tseng. 2011. Underutilization of therapy for hepatocellular carcinoma in the medicare population. *Cancer* 117: 1019–1026.

4. Sonnenday, C. J., J. B. Dimick, R. D. Schulick, and M. A. Choti. 2007. Racial and geographic disparities in the utilization of surgical therapy for hepatocellular carcinoma. *J. Gastrointest. Surg. Off. J. Soc. Surg. Aliment. Tract* 11: 1636–1646; discussion 1646.

5. Popescu, I., S. T. Alexandrescu, I. Popescu, and S. T. Alexandrescu. 2012. Surgical Options for Initially Unresectable Colorectal Liver Metastases, Surgical Options for Initially Unresectable Colorectal Liver Metastases. *HPB Surg. HPB Surg.* 2012, 2012: e454026.

6. Adam, R., V. Delvart, G. Pascal, A. Valeanu, D. Castaing, D. Azoulay, S. Giacchetti, B. Paule, F. Kunstlinger, O. Ghémard, F. Levi, and H. Bismuth. 2004. Rescue Surgery for Unresectable Colorectal Liver Metastases Downstaged by Chemotherapy. *Ann. Surg.* 240: 644–658.

7. Kennedy, A. S., C. Nutting, D. Coldwell, J. Gaiser, and C. Drachenberg. 2004. Pathologic response and microdosimetry of 90Y microspheres in man: Review of four explanted whole livers. *Int. J. Radiat. Oncol.* 60: 1552–1563.

8. Breedis, C., and G. Young. 1954. The Blood Supply of Neoplasms in the Liver. *Am. J. Pathol.* 30: 969–985.

9. Garin, E., Y. Rolland, and E. Boucher. 2013. Pre-therapeutic dosimetry evaluation and selective internal radiation therapy of hepatocellular carcinoma using yttrium-90-loaded microspheres. *J. Hepatol.* 58: 1055–1056.

10. Sangro, B., M. Iñarrairaegui, and J. I. Bilbao. 2013. Reply to: "Pre-therapeutic dosimetry evaluation and selective internal radiation therapy of hepatocellular carcinoma using yttrium-90-loaded microspheres." *J. Hepatol.* 58: 1056–1057.

11. Sangro, B., M. Iñarrairaegui, and J. I. Bilbao. 2012. Radioembolization for hepatocellular carcinoma. *J. Hepatol.* 56: 464–473.

12. Wondergem, M., M. L. J. Smits, M. Elschot, H. W. A. M. de Jong, H. M. Verkooijen, M. A. A. J. van den Bosch, J. F. W. Nijsen, and M. G. E. H. Lam. 2013. 99mTc-macroaggregated albumin poorly predicts the intrahepatic distribution of 90Y resin microspheres in hepatic radioembolization. *J. Nucl. Med. Off. Publ. Soc. Nucl. Med.* 54: 1294–1301.

13. Kao, Y. H., E. H. Tan, T. K. B. Teo, C. E. Ng, and S. W. Goh. 2011. Imaging discordance between hepatic angiography versus Tc-99m-MAA SPECT/CT: a case series, technical discussion and clinical implications. *Ann. Nucl. Med.* 25: 669–676.

14. Strigari, L., R. Sciuto, S. Rea, L. Carpanese, G. Pizzi, A. Soriani, G. Iaccarino, M. Benassi, G. M. Ettorre, and C. L. Maini. 2010. Efficacy and Toxicity Related to Treatment of Hepatocellular Carcinoma with 90Y-SIR Spheres: Radiobiologic Considerations. *J. Nucl. Med.* 51: 1377–1385.

15. Okuda, K., T. Ohtsuki, H. Obata, M. Tomimatsu, N. Okazaki, H. Hasegawa, Y. Nakajima, and K. Ohnishi. 1985. Natural history of hepatocellular carcinoma and prognosis in relation to treatment. Study of 850 patients. *Cancer* 56: 918–928.

16. Giannini, E. G., F. Farinati, F. Ciccarese, A. Pecorelli, G. L. Rapaccini, M. Di Marco, L. Benvegnù, E. Caturelli, M. Zoli, F. Borzio, M. Chiaramonte, F. Trevisani, and Italian Liver Cancer (ITA.LI.CA) group. 2015. Prognosis of untreated hepatocellular carcinoma. *Hepatol. Baltim. Md* 61: 184–190.

17. Görög, D., A. Tóth, and J. Weltner. 1997. Prognosis of untreated liver metastasis from rectal cancer. *Acta Chir. Hung.* 36: 106–107.

18. Adam, R. 2000. The importance of visceral metastasectomy in colorectal cancer. *Ann. Oncol. Off. J. Eur. Soc. Med. Oncol. ESMO* 11 Suppl 3: 29–36.

19. Campbell, J. M., C. O. Wong, O. Muzik, B. Marples, M. Joiner, and J. Burmeister. 2009. Early Dose Response to Yttrium-90 Microsphere Treatment of Metastatic Liver Cancer by a Patient-Specific Method Using Single Photon Emission Computed Tomography and Positron Emission Tomography. *Int. J. Radiat. Oncol.* 74: 313–320.

20. Sarfaraz, M., A. S. Kennedy, M. A. Lodge, X. A. Li, X. Wu, and C. X. Yu. 2004. Radiation absorbed dose distribution in a patient treated with yttrium-90 microspheres for hepatocellular carcinoma. *Med. Phys.* 31: 2449–2453.

21. D’Arienzo, M., P. Chiaramida, L. Chiacchiararelli, A. Coniglio, R. Cianni, R. Salvatori, A. Ruzza, F. Scopinaro, and O. Bagni. 2012. 90Y PET-based dosimetry after selective internal radiotherapy treatments. *Nucl. Med. Commun.* 33: 633–640.

22. Kao, Y.-H., J. D. Steinberg, Y.-S. Tay, G. K. Lim, J. Yan, D. W. Townsend, C. A. Budgeon, J. A. Boucek, R. J. Francis, T. S. Cheo, M. C. Burgmans, F. G. Irani, R. H. Lo, K.-H. Tay, B.-S. Tan, P. K. Chow, S. Satchithanantham, A. E. Tan, D. C. Ng, and A. S. Goh. 2013. Post-radioembolization yttrium-90 PET/CT - part 2: dose-response and tumor predictive dosimetry for resin microspheres. *EJNMMI Res.* 3: 1–12.

23. Fowler, K. J., N. M. Maughan, R. Laforest, N. E. Saad, A. Sharma, J. Olsen, C. K. Speirs, and P. J. Parikh. 2016. PET/MRI of Hepatic 90Y Microsphere Deposition Determines Individual Tumor Response. *Cardiovasc. Intervent. Radiol.* 39: 855–864.

24. Carlier, T., T. Eugène, C. Bodet-Milin, E. Garin, C. Ansquer, C. Rousseau, L. Ferrer, J. Barbet, F. Schoenahl, and F. Kraeber-Bodéré. 2013. Assessment of acquisition protocols for routine imaging of Y-90 using PET/CT. *EJNMMI Res.* 3: 11.

25. Elschot, M., B. J. Vermolen, M. G. E. H. Lam, B. de Keizer, M. A. A. J. van den Bosch, and H. W. A. M. de Jong. 2013. Quantitative Comparison of PET and Bremsstrahlung SPECT for Imaging the In Vivo Yttrium-90 Microsphere Distribution after Liver Radioembolization. *PLoS ONE* 8.

26. Kao, Y.-H., J. D. Steinberg, Y.-S. Tay, G. K. Lim, J. Yan, D. W. Townsend, A. Takano, M. C. Burgmans, F. G. Irani, T. K. Teo, T.-N. Yeow, A. Gogna, R. H. Lo, K.-H. Tay, B.-S. Tan, P. K. Chow, S. Satchithanantham, A. E. Tan, D. C. Ng, and A. S. Goh. 2013. Post-radioembolization yttrium-90 PET/CT - part 1: diagnostic reporting. *EJNMMI Res.* 3: 56.

27. Rong, X., Y. Du, M. Ljungberg, E. Rault, S. Vandenberghe, and E. C. Frey. 2012. Development and evaluation of an improved quantitative 90Y bremsstrahlung SPECT method. *Med. Phys.* 39: 2346–2358.

28. Elschot, M., M. G. E. H. Lam, M. A. A. J. van den Bosch, M. A. Viergever, and H. W. A. M. de Jong. 2013. Quantitative Monte Carlo–Based 90Y SPECT Reconstruction. *J. Nucl. Med.* 54: 1557–1563.

29. Dewaraja, Y. K., M. J. Schipper, P. L. Roberson, S. J. Wilderman, H. Amro, D. D. Regan, K. F. Koral, M. S. Kaminski, and A. M. Avram. 2010. 131I-Tositumomab

Radioimmunotherapy: Initial Tumor Dose–Response Results Using 3-Dimensional Dosimetry Including Radiobiologic Modeling. *J. Nucl. Med.* 51: 1155–1162.

30. Pasciak, A. S., A. C. Bourgeois, J. M. McKinney, T. T. Chang, D. R. Osborne, S. N. Acuff, and Y. C. Bradley. 2014. Radioembolization and the Dynamic Role of 90Y PET/CT. *Front. Oncol.* 4.

31. Chiesa, C., M. Mira, M. Maccauro, C. Spreafico, R. Romito, C. Morosi, T. Camerini, M. Carrara, S. Pellizzari, A. Negri, G. Aliberti, C. Sposito, S. Bhoori, A. Facciorusso, E. Civelli, R. Lanocita, B. Padovano, M. Migliorisi, M. C. D. Nile, E. Seregni, A. Marchianò, F. Crippa, and V. Mazzaferro. 2015. Radioembolization of hepatocarcinoma with 90Y glass microspheres: development of an individualized treatment planning strategy based on dosimetry and radiobiology. *Eur. J. Nucl. Med. Mol. Imaging* 42: 1718–1738.

32. O' Doherty, J. 2015. A review of 3D image-based dosimetry, technical considerations and emerging perspectives in 90Y microsphere therapy. *J. Diagn. Imaging Ther.* 2: 1–34.

33. Kennedy, A., W. Dezarn, and A. Weiss. 2011. Patient Specific 3D Image-Based Radiation Dose Estimates for 90Y Microsphere Hepatic Radioembolization in Metastatic Tumors. *J. Nucl. Med. Radiat. Ther.* 1.

34. Dieudonné, A., E. Garin, S. Laffont, Y. Rolland, R. Lebtahi, D. Leguludec, and I. Gardin. 2011. Clinical Feasibility of Fast 3-Dimensional Dosimetry of the Liver for Treatment Planning of Hepatocellular Carcinoma with 90Y-Microspheres. *J. Nucl. Med.* 52: 1930–1937.

35. Pasciak, A. S., A. C. Bourgeois, and Y. C. Bradley. 2014. A Comparison of Techniques for 90Y PET/CT Image-Based Dosimetry Following Radioembolization with Resin Microspheres. *Front. Oncol.* 4.

36. Willowson, K., N. Forwood, B. W. Jakoby, A. M. Smith, and D. L. Bailey. 2012. Quantitative 90Y image reconstruction in PET. *Med. Phys.* 39: 7153–7159.

37. Goedicke, A., Y. Berker, F. A. Verburg, F. F. Behrendt, O. Winz, and F. M. Mottaghy. 2013. Study-Parameter Impact in Quantitative 90-Yttrium PET Imaging for Radioembolization Treatment Monitoring and Dosimetry. *IEEE Trans. Med. Imaging* 32: 485–492.

38. Martí-Climent, J. M., E. Prieto, C. Elosúa, M. Rodríguez-Fraile, I. Domínguez-Prado, C. Vigil, M. J. García-Velloso, J. Arbizu, I. Peñuelas, and J. A. Richter. 2014. PET optimization for improved assessment and accurate quantification of 90Y-microsphere biodistribution after radioembolization. *Med. Phys.* 41: 92503.

39. Tapp, K. N., W. B. Lea, M. S. Johnson, M. Tann, J. W. Fletcher, and G. D. Hutchins. 2014. The Impact of Image Reconstruction Bias on PET/CT 90Y Dosimetry After Radioembolization. *J. Nucl. Med.* 55: 1452–1458.

40. Sgouros, G., and R. F. Hobbs. 2014. Dosimetry for Radiopharmaceutical Therapy. *Semin. Nucl. Med.* 44: 172–178.

41. Nehmeh, S. A. 2013. Respiratory Motion Correction Strategies in Thoracic PET-CT Imaging. *PET Clin.* 8: 29–36.

42. Li, G., C. R. Schmidtlein, I. A. Burger, C. A. Ridge, S. B. Solomon, and J. L. Humm. 2014. Assessing and accounting for the impact of respiratory motion on FDG uptake and viable volume for liver lesions in free-breathing PET using respiration-suspended PET images as reference. *Med. Phys.* 41: 91905.

43. Teo, B.-K., B. Saboury, R. Munbodh, J. Scheuermann, D. A. Torigian, H. Zaidi, and A. Alavi. 2012. The effect of breathing irregularities on quantitative accuracy of respiratory gated PET/CT. *Med. Phys.* 39: 7390–7397.

44. Bettinardi, V., E. Rapisarda, and M. C. Gilardi. 2009. Number of partitions (gates) needed to obtain motion-free images in a respiratory gated 4D-PET/CT study as a function of the lesion size and motion displacement. *Med. Phys.* 36: 5547–5558.

45. Liu, C., A. Alessio, L. Pierce, K. Thielemans, S. Wollenweber, A. Ganin, and P. Kinahan. 2010. Quiescent period respiratory gating for PET⁄CT. *Med. Phys.* 37: 5037–5043.

46. Lu, W., P. J. Parikh, J. P. Hubenschmidt, J. D. Bradley, and D. A. Low. 2006. A comparison between amplitude sorting and phase-angle sorting using external respiratory measurement for 4D CT. *Med. Phys.* 33: 2964–2974.

47. Bourgeois, A. C., T. T. Chang, Y. C. Bradley, S. N. Acuff, and A. S. Pasciak. 2014. Intraprocedural yttrium-90 positron emission tomography/CT for treatment optimization of yttrium-90 radioembolization. *J. Vasc. Interv. Radiol. JVIR* 25: 271–275.

48. Salem, R., K. G. Thurston, B. I. Carr, J. E. Goin, and J.-F. H. Geschwind. 2002. Yttrium-90 microspheres: radiation therapy for unresectable liver cancer. *J. Vasc. Interv. Radiol. JVIR* 13: S223-229.

49. Salem, R., and K. G. Thurston. 2006. Radioembolization with 90Yttrium microspheres: a state-of-the-art brachytherapy treatment for primary and secondary liver malignancies. Part 1: Technical and methodologic considerations. *J. Vasc. Interv. Radiol. JVIR* 17: 1251–1278.

50. Selwyn, R. G., R. J. Nickles, B. R. Thomadsen, L. A. DeWerd, and J. A. Micka. 2007. A new internal pair production branching ratio of 90Y: the development of a non-destructive

assay for 90Y and 90Sr. *Appl. Radiat. Isot. Data Instrum. Methods Use Agric. Ind. Med.* 65: 318–327.

51. Mikell, J. K., A. Mahvash, W. Siman, F. Mourtada, and S. C. Kappadath. 2015. Comparing voxel-based absorbed dosimetry methods in tumors, liver, lung, and at the liver-lung interface for 90 Y microsphere selective internal radiation therapy. *EJNMMI Phys.* 2: 16.

52. Heard, S., G. D. Flux, M. J. Guy, and R. J. Ott. 2004. Monte Carlo simulation of 90Y Bremsstrahlung imaging. In *2004 IEEE Nuclear Science Symposium Conference Record* vol. 6. 3579–3583 Vol. 6.

53. Walrand, S. 2014. Bremsstrahlung SPECT/CT. In *Clinical Applications of SPECT-CT* H. Ahmadzadehfar, and H.-J. Biersack, eds. Springer Berlin Heidelberg. 271–280.

54. Rong, X., M. Ghaly, and E. C. Frey. 2013. Optimization of energy window for 90Y bremsstrahlung SPECT imaging for detection tasks using the ideal observer with model-mismatch. *Med. Phys.* 40: 62502.

55. Hulme, K. W., and S. C. Kappadath. 2014. Implications of CT noise and artifacts for quantitative 99mTc SPECT/CT imaging. *Med. Phys.* 41: 42502.

56. Jaszczak, R. J., J. Floyd, C.E., and R. E. Coleman. 1985. Scatter Compensation Techniques for SPECT. *IEEE Trans. Nucl. Sci.* 32: 786–793.

57. Ogawa, K., Y. Harata, T. Ichihara, A. Kubo, and S. Hashimoto. 1991. A practical method for position-dependent Compton-scatter correction in single photon emission CT. *IEEE Trans. Med. Imaging* 10: 408–412.

58. Koral, K. F., K. R. Zasadny, R. J. Ackermann, and E. P. Ficaro. 1998. Deadtime correction for two multihead Anger cameras in [sup 131]I dual-energy-window-acquisition mode. *Med. Phys.* 25: 85.

59. Koral, K. F., J. N. Kritzmaan, V. E. Rogers, R. J. Ackermann, and J. A Fessler. 2007. Optimizing the number of equivalent iterations of 3D OSEM in SPECT reconstruction of I-131 focal activities. *Nucl. Instrum. Methods Phys. Res. Sect. Accel. Spectrometers Detect. Assoc. Equip.* 579: 326–329.

60. Rong, X., M. Ghaly, and E. Frey. 2012. Optimization of energy windows for Y-90 bremsstrahlung SPECT for detection tasks in microsphere brachytherapy. *Soc. Nucl. Med. Annu. Meet. Abstr.* 53: 431.

61. Rong, X., and E. C. Frey. 2013. A collimator optimization method for quantitative imaging: application to Y-90 bremsstrahlung SPECT. *Med. Phys.* 40: 82504.

62. Walrand, S., M. Hesse, R. Wojcik, R. Lhommel, and F. Jamar. 2014. Optimal design of Anger camera for bremsstrahlung imaging: Monte Carlo evaluation. *Cancer Imaging Diagn.* 4: 149.

63. Moore, S. C., M.-A. Park, M. Cervo, and S. P. Muller. 2012. A fast Monte Carlo-based forward projector with complete physics modeling of Y-90 bremsstrahlung. In *2012 IEEE Nuclear Science Symposium and Medical Imaging Conference (NSS/MIC)* 2699–2701.

64. Zeintl, J., A. H. Vija, A. Yahil, J. Hornegger, and T. Kuwert. 2010. Quantitative Accuracy of Clinical 99mTc SPECT/CT Using Ordered-Subset Expectation Maximization with 3-Dimensional Resolution Recovery, Attenuation, and Scatter Correction. *J. Nucl. Med.* 51: 921–928.

65. Jentzen, W. 2010. Experimental investigation of factors affecting the absolute recovery coefficients in iodine-124 PET lesion imaging. *Phys. Med. Biol.* 55: 2365.

66. Willowson, K. P., M. Tapner, D. L. Bailey, and T. Q. I. Team. 2015. A multicentre comparison of quantitative 90Y PET/CT for dosimetric purposes after radioembolization with resin microspheres. *Eur. J. Nucl. Med. Mol. Imaging* 1–21.

67. Willowson, K., N. Forwood, B. W. Jakoby, A. M. Smith, and D. L. Bailey. 2012. Quantitative 90Y image reconstruction in PET. *Med. Phys.* 39: 7153–7159.

68. Siman, W., M. Silosky, and S. C. Kappadath. 2015. A revised monitor source method for practical deadtime count loss compensation in clinical planar and SPECT studies. *Phys. Med. Biol.* 60: 1199.

69. Silosky, M., V. Johnson, C. Beasley, and S. C. Kappadath. 2013. Characterization of the count rate performance of modern gamma cameras. *Med. Phys.* 40: 32502.

70. Nath, R., W. S. Bice, W. M. Butler, Z. Chen, A. S. Meigooni, V. Narayana, M. J. Rivard, Y. Yu, and American Association of Physicists in Medicine. 2009. AAPM recommendations on dose prescription and reporting methods for permanent interstitial brachytherapy for prostate cancer: report of Task Group 137. *Med. Phys.* 36: 5310–5322.

71. Gulec, S. A., M. L. Sztejnberg, J. A. Siegel, T. Jevremovic, and M. Stabin. 2010. Hepatic Structural Dosimetry in 90Y Microsphere Treatment: A Monte Carlo Modeling Approach Based on Lobular Microanatomy. *J. Nucl. Med.* 51: 301–310.

72. Ho, S., W. Y. Lau, T. W. T. Leung, M. Chan, Y. K. Ngar, P. J. Johnson, and A. K. C. Li. 1996. Partition model for estimating radiation doses from yttrium-90 microspheres in treating hepatic tumours. *Eur. J. Nucl. Med.* 23: 947–952.

73. Strigari, L., R. Sciuto, S. Rea, L. Carpanese, G. Pizzi, A. Soriani, G. Iaccarino, M. Benassi, G. M. Ettorre, and C. L. Maini. 2010. Efficacy and Toxicity Related to Treatment of Hepatocellular Carcinoma with 90Y-SIR Spheres: Radiobiologic Considerations. *J. Nucl. Med.* 51: 1377–1385.

74. Dewaraja, Y. K., E. C. Frey, G. Sgouros, A. B. Brill, P. Roberson, P. B. Zanzonico, and M. Ljungberg. 2012. MIRD Pamphlet No. 23: Quantitative SPECT for Patient-Specific 3-Dimensional Dosimetry in Internal Radionuclide Therapy. *J. Nucl. Med. Off. Publ. Soc. Nucl. Med.* 53: 1310–1325.

75. Lhommel, R., L. van Elmbt, P. Goffette, M. Van den Eynde, F. Jamar, S. Pauwels, and S. Walrand. 2010. Feasibility of 90Y TOF PET-based dosimetry in liver metastasis therapy using SIR-Spheres. *Eur. J. Nucl. Med. Mol. Imaging* 37: 1654–1662.

76. Drzymala, R. E., R. Mohan, L. Brewster, J. Chu, M. Goitein, W. Harms, and M. Urie. 1991. Dose-volume histograms. *Int. J. Radiat. Oncol. Biol. Phys.* 21: 71–78.

77. Cheng, L., R. F. Hobbs, P. W. Segars, G. Sgouros, and E. C. Frey. 2013. Improved dose–volume histogram estimates for radiopharmaceutical therapy by optimizing quantitative SPECT reconstruction parameters. *Phys. Med. Biol.* 58: 3631.

78. Niemierko, A., and M. Goitein. 1993. Implementation of a model for estimating tumor control probability for an inhomogeneously irradiated tumor. *Radiother. Oncol.* 29: 140–147.

79. Warkentin, B., P. Stavrev, N. Stavreva, C. Field, and B. G. Fallone. 2004. A TCP-NTCP estimation module using DVHs and known radiobiological models and parameter sets. *J. Appl. Clin. Med. Phys. Am. Coll. Med. Phys.* 5: 50–63.

80. Fourkal, E., I. Veltchev, M. Lin, S. Koren, J. Meyer, M. Doss, and J. Q. Yu. 2013. 3D inpatient dose reconstruction from the PET-CT imaging of 90Y microspheres for metastatic cancer to the liver: Feasibility study. *Med. Phys.* 40: 81702.

81. Cremonesi, M., C. Chiesa, L. Strigari, M. Ferrari, F. Botta, F. Guerriero, C. De Cicco, G. Bonomo, F. Orsi, L. Bodei, A. Di Dia, C. M. Grana, and R. Orecchia. 2014. Radioembolization of Hepatic Lesions from a Radiobiology and Dosimetric Perspective. *Front. Oncol.* 4.

82. Pasciak, A. S., A. C. Bourgeois, and Y. C. Bradley. 2016. A Microdosimetric Analysis of Absorbed Dose to Tumor as a Function of Number of Microspheres per Unit Volume in 90Y Radioembolization. *J. Nucl. Med.* 57: 1020–1026.

83. Kao, Y. H., O. S. Luddington, S. R. Culleton, R. J. Francis, and J. A. Boucek. 2014. A gelatin liver phantom of suspended 90Y resin microspheres to simulate the physiologic microsphere biodistribution of a postradioembolization liver. *J. Nucl. Med. Technol.* 42: 265–268.

84. Carlier, T., K. P. Willowson, E. Fourkal, D. L. Bailey, M. Doss, and M. Conti. 2015. 90Y -PET imaging: Exploring limitations and accuracy under conditions of low counts and high random fraction. *Med. Phys.* 42: 4295–4309.

85. Garin, E., L. Lenoir, J. Edeline, S. Laffont, H. Mesbah, P. Porée, L. Sulpice, K. Boudjema, M. Mesbah, A. Guillygomarc'h, E. Quehen, M. Pracht, J. L. Raoul, B. Clement, Y. Rolland, and E. Boucher. 2013. Boosted selective internal radiation therapy with 90Y-loaded glass microspheres (B-SIRT) for hepatocellular carcinoma patients: a new personalized promising concept. *Eur. J. Nucl. Med. Mol. Imaging* 40: 1057–1068.

86. Rousset, O., A. Rahmim, A. Alavi, and H. Zaidi. 2007. Partial Volume Correction Strategies in PET. *PET Clin.* 2: 235–249.

87. Campbell, J. M., C. O. Wong, O. Muzik, B. Marples, M. Joiner, and J. Burmeister. 2009. Early Dose Response to Yttrium-90 Microsphere Treatment of Metastatic Liver Cancer by a Patient-Specific Method Using Single Photon Emission Computed Tomography and Positron Emission Tomography. *Int. J. Radiat. Oncol.* 74: 313–320.

88. Lhommel, R., P. Goffette, M. V. den Eynde, F. Jamar, S. Pauwels, J. I. Bilbao, and S. Walrand. 2009. Yttrium-90 TOF PET scan demonstrates high-resolution biodistribution after liver SIRT. *Eur. J. Nucl. Med. Mol. Imaging* 36: 1696–1696.

89. Qiao, F., T. Pan, J. W. C. Jr, and O. R. Mawlawi. 2006. A motion-incorporated reconstruction method for gated PET studies. *Phys. Med. Biol.* 51: 3769.

90. Nehmeh, S. A., Y. E. Erdi, T. Pan, E. Yorke, G. S. Mageras, K. E. Rosenzweig, H. Schoder, H. Mostafavi, O. Squire, A. Pevsner, S. M. Larson, and J. L. Humm. 2004. Quantitation of respiratory motion during 4D-PET/CT acquisition. *Med. Phys.* 31: 1333–1338.

91. Attarwala, A. A., F. Molina-Duran, K.-A. Büsing, S. O. Schönberg, D. L. Bailey, K. Willowson, and G. Glatting. 2014. Quantitative and Qualitative Assessment of Yttrium-90 PET/CT Imaging. *PLoS ONE* 9.

92. Sgouros, G. 2005. Dosimetry of internal emitters. *J. Nucl. Med. Off. Publ. Soc. Nucl. Med.* 46 Suppl 1: 18S–27S.

93. Cheng, L., R. F. Hobbs, G. Sgouros, and E. C. Frey. 2014. Development and evaluation of convergent and accelerated penalized SPECT image reconstruction methods for improved dose–volume histogram estimation in radiopharmaceutical therapy. *Med. Phys.* 41: 112507.

94. Petitguillaume, A., M. Bernardini, L. Hadid, C. de Labriolle-Vaylet, D. Franck, and A. Desbrée. 2014. Three-Dimensional Personalized Monte Carlo Dosimetry in 90Y Resin Microspheres Therapy of Hepatic Metastases: Nontumoral Liver and Lungs Radiation Protection Considerations and Treatment Planning Optimization. *J. Nucl. Med.* 55: 405–413.

95. Nehmeh, S. A., Y. E. Erdi, C. C. Ling, K. E. Rosenzweig, H. Schoder, S. M. Larson, H. A. Macapinlac, O. D. Squire, and J. L. Humm. 2002. Effect of Respiratory Gating on Quantifying PET Images of Lung Cancer. *J. Nucl. Med.* 43: 876–881.

96. Fitzpatrick, M. J., G. Starkschall, P. Balter, J. A. Antolak, T. Guerrero, C. Nelson, P. Keall, and R. Mohan. 2005. A novel platform simulating irregular motion to enhance assessment of respiration-correlated radiation therapy procedures. *J. Appl. Clin. Med. Phys. Am. Coll. Med. Phys.* 6: 13–21.

97. Grimes, J., and A. Celler. 2014. Comparison of internal dose estimates obtained using organ-level, voxel S value, and Monte Carlo techniques. *Med. Phys.* 41: 92501.

98. Nehmeh, S. A., and Y. E. Erdi. 2008. Respiratory Motion in Positron Emission Tomography/Computed Tomography: A Review. *Semin. Nucl. Med.* 38: 167–176.

99. Prekeges, J. 2012. *Nuclear Medicine Instrumentation,*. Jones & Bartlett Publishers.

100. Martin, C. C., B. T. Christian, M. R. Satter, L. D. H. Nickerson, and R. J. Nickles. 1995. Quantitative PET with positron emitters that emit prompt gamma rays. *IEEE Trans. Med. Imaging* 14: 681–687.

101. Pépin, A., J. Daouk, P. Bailly, S. Hapdey, and M.-E. Meyer. 2014. Management of respiratory motion in PET/computed tomography: the state of the art. *Nucl. Med. Commun.* 35: 113–122.

102. Li, T., B. Thorndyke, E. Schreibmann, Y. Yang, and L. Xing. 2006. Model-based image reconstruction for four-dimensional PET. *Med. Phys.* 33: 1288–1298.

103. Dawood, M., N. Lang, X. Jiang, and K. P. Schafers. 2006. Lung motion correction on respiratory gated 3-D PET/CT images. *IEEE Trans. Med. Imaging* 25: 476–485.

104. Klein, G. J., R. W. Reutter, and R. H. Huesman. 2001. Four-dimensional affine registration models for respiratory-gated PET. *IEEE Trans. Nucl. Sci.* 48: 756–760.

105. Dahlbom, M., D.-C. Yu, S. R. Cherry, A. Chatziioannou, and E. J. Hoffman. 1992. Methods for improving image quality in whole body PET scanning. *IEEE Trans. Nucl. Sci.* 39: 1079–1083.

106. Panin, V. Y., A. M. Smith, J. Hu, F. Kehren, and M. E. Casey. 2014. Continuous bed motion on clinical scanner: design, data correction, and reconstruction. *Phys. Med. Biol.* 59: 6153–6174.

107. Schubert, S. F., S. Pajevic, and R. E. Carson. 1996. Whole body PET using overlapped 3D acquisition and weighted image summation. In *, 1996 IEEE Nuclear Science Symposium, 1996. Conference Record* vol. 2. 1285–1289 vol.2.

108. Dahlbom, M., J. Reed, and J. Young. 2000. Implementation of true continuous 2D/3D whole body PET scanning. In *2000 IEEE Nuclear Science Symposium Conference Record* vol. 3. 17/13-17/17 vol.3.

109. Everding, M., D. Emery, O. Mawlawi, R. Millican-Campbell, T. Palendat, T. Pan, L. Peirsol, B. Simon, N. Swanston, and E. Rohren. 2014. Impact of continuous bed motion (CBM) PET/CT scanners on clinical operation. *Soc. Nucl. Med. Annu. Meet. Abstr.* 55: 2511.

110. Osborne, D. R., S. Acuff, S. Cruise, M. Syed, M. Neveu, A. Stuckey, and Y. Bradley. 2014. Quantitative and qualitative comparison of continuous bed motion and traditional step and shoot PET/CT. *Am. J. Nucl. Med. Mol. Imaging* 5: 56–64.

111. Carlier, T., T. Eugène, C. Bodet-Milin, E. Garin, C. Ansquer, C. Rousseau, L. Ferrer, J. Barbet, F. Schoenahl, and F. Kraeber-Bodéré. 2013. Assessment of acquisition protocols for routine imaging of Y-90 using PET/CT. *EJNMMI Res.* 3: 11.

112. Daube-Witherspoon, M. E., and G. Muehllehner. 1987. Treatment of Axial Data in Three-Dimensional PET. *J. Nucl. Med.* 28: 1717–1724.

VITA

Wendy Siman was born in Jakarta, Indonesia on April 23, 1986, the son of Turino Lusfaidi and Turino Sualina. He first came to the United States to Urbana, IL, where he earned a Bachelor of Science degree in Engineering Physics with very high honors from the University of Illinois at Urbana-Champaign in May of 2008. He later went on to complete Master of Science in Medical Physics from Columbia University in the city of New York (December of 2009) before matriculating to The University of Texas Health Science Center at Houston Graduate School of Biomedical Science in August 2012.

Permanent address:

TBD